

UNIVERSITY OF CALIFORNIA
SANTA BARBARA

Characterizing the Edge of Chaos for Shear Flows

by

Lina Kim

A Dissertation submitted in partial satisfaction of the
requirements for the degree of
Doctor of Philosophy

in

Mechanical Engineering

Committee in charge:
Professor Jeffrey Moehlis, Chair
Professor Igor Mezić
Professor George Homsy
Professor Bruno Eckhardt

September 2009

The dissertation of Lina Kim is approved:

Professor Igor Mezić

Professor George Homsy

Professor Bruno Eckhardt

Professor Jeffrey Moehlis, Chair

September 2009

Characterizing the Edge of Chaos for Shear Flows

Copyright © 2009

by

Lina Kim

To my father

Acknowledgments

First and foremost, I would like to express my gratitude to my graduate advisor Jeff Moehlis for being an excellent mentor and teacher. Without a doubt, his enthusiasm for science has helped me become a better researcher. He has been a true inspiration and this work would not have been possible without his encouragement and support.

I would like to thank George Homsy, Igor Mezić, and Bruno Eckhardt for their advice, valuable comments on this work, and for kindly serving in my committee. I especially want to thank Bruno Eckhardt for the numerous fruitful discussions and constant encouragement. To all my teachers present and past, thank you for instilling in me a great appreciation for science. I would like to thank Tobias Schneider for his helpful comments on this work. This work would not have been completed without the support from John Gibson. His channelflow library has opened up so many research doors, none of us could have done this without him.

I am indebted to the QSR Linux Cluster of the California NanoSystems Institute high computing facility with Hewlett–Packard at UC Santa Barbara, the MARC Linux Cluster of the Hochschulrechenzentrum in Marburg, Germany, Alex Olshansky, and Paul Weakliem for the computational support.

I would like to thank the NSF for giving me the opportunity to be part of the LEAPS team for two years. I have learned so much about teaching from working

with eight-grade students, I truly believe that I am a better teacher and researcher from this experience. I also need to thank Fiona Goodchild, Beth Gwinn, and Wendy Ibsen for being great role models and for the constant support. I would like to give thanks to Santa Barbara Junior High School and the fellows for an amazing two years.

The graduate school experience would not have been the same without my colleagues, I thank you for keeping it light when it was tough. It has been a privilege to work with the Moehlis research group; we might have worked on different areas but we all had each other in common and I could not have asked for a better research group. I would also like to thank my office mates and all other former and current members of the Dynamics, Controls and Robotics Lab.

I would like to thank my friends, from every part of my life for helping me become the person I am today, I am honored and lucky to have met such wonderful people. This dissertation would not have been possible without the understanding and continuous support of my family. To my family in Argentina, gracias por creer en mí y por todo el amor que me han dado. Romina, you are an amazing person and sister, I am very proud of you. Finally and most importantly, my parents who have not only encouraged me to become the best person I could be but have also taught me to never give up and have sacrificed so much to give me and my sister the best education.

Vita of Lina Kim

September 2009

Education

Ph.D. in Mechanical Engineering September 2009
University of California, Santa Barbara

M.S. in Mechanical Engineering August 2005
University of California, Santa Barbara

B.S. in Mechanical Engineering (cum laude) June 2003
University of California, Riverside

Professional Employment

Graduate Student Researcher, Supervisor: Jeff Moehlis 2004–2007
Department of Mechanical Engineering, University of California, Santa Barbara

Teaching Assistant and Course Reader 2003–2009
Department of Mechanical Engineering, University of California, Santa Barbara

Scientist, Santa Barbara Junior High School 2007–2009

Publications

L. Kim and J. Moehlis, Characterizing the Edge of Chaos for a Shear Flow Model, *Phys. Rev. E*, **78** : 036315, 2008

L. Kim and J. Moehlis, Transient Growth for Streak-Streamwise Vortex Interactions, *Phys. Lett. A*, **358**, 431 – 37, 2006

L. Kim and J. Moehlis, Streak-Streamwise Vortex Interactions: Transient Growth and Optimal Perturbations, *unpublished*

L. Kim, Transient Growth for a Sinusoidal Shear Flow Model, M.S. Thesis, 2005

Awards and Honors

NSF Let's Explore Applied Physical Sciences (LEAPS) Fellowship, 2007-2009

Abstract

Characterizing the Edge of Chaos for Shear Flows

by

Lina Kim

The transition to turbulence in linearly stable shear flows is one of the most intriguing and outstanding problems in classical physics. It is of fundamental interest from a mathematical and physical perspective, since understanding the mechanisms that trigger turbulence would give great insight into the nature of turbulence and would provide a foundation for control of these flows. Turbulent dynamics are readily observed at flow speeds where the laminar state remains stable under infinitesimal perturbations. Moreover, for a smaller class of shear flows, such as plane Couette flow and pipe flow, linear stability theory predicts that the laminar state remains stable for all Reynolds numbers. However, numerical simulations and experiments provide evidence that these flows exhibit turbulence for sufficiently high Reynolds numbers and perturbations.

The accepted representation of the behaviors in state space postulated that the stable laminar solution coexisted with the turbulent regime. Only recently, the notion of a third, dynamically invariant region that might lie between the laminar

and turbulent regions in state space has been suggested. In it, the dynamics would differ from those observed in the laminar and turbulent regimes. This boundary, called the *edge of chaos*, contains invariant solutions, the *edge states* which are too weak to become turbulent and too strong to decay to the laminar state. The edge of chaos separates trajectories that directly decay to the laminar state from those that grow and become turbulent.

These edge states, which can be either dynamically simple or complex structures, are identified using an iterated edge tracking algorithm based on a bisection method. This dissertation focuses on a dynamical systems analysis of the transition to turbulence in sinusoidal shear flow and plane Couette flow. For sinusoidal shear flow, the edge of chaos is characterized for a low-dimensional model derived via a Galerkin projection onto physically meaningful modes. The edge coincides with the codimension-1 stable manifold of an unstable periodic orbit. For the related system of plane Couette flow, direct numerical simulations of the Navier-Stokes equations are performed to identify edge states for different flow domains. For a particular range of flow geometries, multiple, non-symmetry related edge states, which coexist in state space, were found. The characterization of the edge of chaos will provide a greater understanding of the transition to turbulence in turbulent shear flows.

Contents

List of Figures	x
List of Tables	xii
1 Shear Flow Turbulence	1
1.1 Motivation	2
1.2 The Transition to Turbulence	2
1.3 The Governing Equations for Fluid Flow	5
1.4 Dynamical Systems Theory	6
1.4.1 Equilibria	6
1.4.2 Periodic Orbits	7
1.4.3 Invariant Manifolds	7
1.5 Scope of the Dissertation	8
2 The Edge of Chaos	9
2.1 The Laminar–Turbulent Boundary	9
2.2 Geometry of the Boundary	10
2.3 Dynamics on the Edge of Chaos	11
2.4 Previous Studies of the Edge of Chaos	12
2.4.1 Parallel Shear Flow	13
2.4.2 Pipe Flow	14
2.4.3 Plane Couette Flow	15
3 The Edge of Chaos for a Low–Dimensional Model	16
3.1 A Low–Dimensional Model for Sinusoidal Shear Flow	16
3.1.1 Prominent Modes	17
3.1.2 Amplitude Equations	19
3.1.3 Dynamics of the Model	20
3.2 Finding the Edge of Chaos	21

3.3	The Edge of Chaos for Sinusoidal Shear Flow	22
3.3.1	The Chaotic Transient State	23
3.3.2	Characteristics of the Unstable Periodic Orbit Associated with the Edge of Chaos	23
3.4	Probabilistic Analysis of the Edge of Chaos	25
3.5	Basin Boundary of the Nontrivial Attractor	28
3.6	Discussion	31
4	The Laminar–Turbulent Boundary in Plane Couette Flow	34
4.1	Plane Couette Flow	34
4.1.1	Symmetries of Plane Couette Flow	35
4.2	Numerical Analysis	36
4.2.1	Numerical Discretization and Resolution	36
4.2.2	The Edge Tracking Algorithm	37
4.2.3	Finding Eigenvalues	41
4.2.4	Searching for Invariant Structures	41
4.3	The $L_x = 4\pi$ and $L_z = 2\pi$ Domain	42
4.4	The $L_x = 4\pi$ and $L_z = 4\pi$ Domain	47
4.5	Multiple Edge States	47
4.5.1	Approximate Connections Between Edge States	49
4.6	Long Flow Domains	54
4.7	Discussion	55
5	Conclusions	59
5.1	Outlook	60
	Bibliography	61
A	Uniform Distribution of Initial Conditions for an n-Dimensional Sphere	65
B	Approximating Edge Trajectories Using an Edge Tracking Algo- rithm	67
C	A Summary of States found in Plane Couette Flow	69

List of Figures

1.1	Sketch of Reynolds's experiment	3
2.1	2-dimensional sketch of the laminar-turbulent boundary in state space	10
2.2	Trajectories on either side of the laminar-turbulent boundary . .	11
2.3	Turbulent lifetimes as a function of scaling amplitudes and Reynolds numbers	12
2.4	Lifetimes of perturbations for a low-dimensional model for sinusoidal shear flow	13
2.5	Dynamics associated with the edge of chaos	14
3.1	Geometry of sinusoidal shear flow	17
3.2	Turbulent statistics for sinusoidal shear and plane Couette flows .	21
3.3	Schematic diagram of the edge tracking algorithm for sinusoidal shear flow	22
3.4	Transient and decay dynamics for the nine-dimensional model for sinusoidal shear flow	23
3.5	Schematic diagram of the edge of chaos for the nine-dimensional model for sinusoidal shear flow	24
3.6	The unstable periodic orbit associated with the edge of chaos for sinusoidal shear flow	25
3.7	Time series for the amplitudes of the unstable periodic orbit associated with the edge for sinusoidal shear flow	26
3.8	Average values for energy, streaks, and streamwise vortices of the unstable periodic orbit	27
3.9	Probability of transient chaos as a function of Reynolds number and initial perturbation energy	29
3.10	Sustained, transient, and decay dynamics for the nine-dimensional model for sinusoidal shear flow	30

3.11	Nontrivial attractors in the nine-model model for sinusoidal shear flow	31
3.12	Bifurcation diagram for the nine-dimensional model for sinusoidal shear flow	32
3.13	Probability of reaching the nontrivial attractor as a function of Reynolds number and initial perturbation energy	32
3.14	Basin boundary of the nontrivial attractor	33
4.1	Geometry of plane Couette flow	35
4.2	A schematic representation of the iterated edge tracking algorithm for plane Couette flow	38
4.3	Typical iteration of the edge tracking algorithm for plane Couette flow	39
4.4	Trajectories near the edge of chaos	40
4.5	Edge trajectories for the $L_x = 4\pi$ and $L_z = 2\pi$ plane Couette flow domain calculated with the edge-tracking algorithm	43
4.6	The edge state in the $L_x = 4\pi$ and $L_z = 2\pi$ domain	44
4.7	Invariant state in the $L_x = 4\pi$ and $L_z = 2\pi$ domain	45
4.8	Sketch of invariant states in the edge of chaos	46
4.9	The edge state in the $L_x = 4\pi$ and $L_z = 4\pi$ domain	48
4.10	Eigenvalue analysis for variable channel widths	49
4.11	The 4-roll edge state in the $L_x = 4\pi$ and $L_z = 3.5\pi$ domain	50
4.12	The 6-roll edge state in the $L_x = 4\pi$ and $L_z = 3.5\pi$ domain	51
4.13	Edge states for variable Reynolds number in the $L_x = 4\pi$ and $L_z = 3.5\pi$ domain	52
4.14	Approximate edge trajectory which comes near both edge states	53
4.15	Approximate edge trajectory which comes near both edge states multiple times	54
4.16	Sketch of the dynamics in state space showing approximate connections between edge states	55
4.17	Energy traces of perturbations on the unstable manifold of edge states	56
4.18	The edge state in the $L_x = 8\pi$ and $L_z = 2\pi$ domain	57
4.19	The edge state in the $L_x = 16\pi$ and $L_z = 2\pi$ domain	58
B.1	Edge tracking algorithm flowchart	68

List of Tables

3.1	Classification of the nontrivial attractor as a function of Re	29
3.2	Reynolds number scalings for probability of transient chaos curves.	30
4.1	Sample scaling factor calculations	39
C.1	Classification of edge states in plane Couette flow	69

Chapter 1

Shear Flow Turbulence

“I am an old man now, and when I die and go to heaven there are two matters on which I hope for enlightenment. One is quantum electrodynamics, and the other is the turbulent motion of fluids. And about the former I am rather optimistic.”

–Horace Lamb, 1934

One of the greatest unsolved problems in classical physics is understanding the nature of turbulence. In addition to being of fundamental interest, advancements in this area of research could lead to the ability to control or produce turbulent flows, which could result in dramatic improvements in the design, efficiency, and performance of many technological systems. Certainly, much progress has been

made in describing and understanding the nature of turbulence, but there is much yet to learn.

Indeed, despite a century of vigorous efforts to develop a universal theory for turbulence, theorists have yet to thoroughly describe this phenomenon. However, notable progress was made in the first half of the 20th century, when both Richardson and Kolmogorov ventured to describe turbulence using statistical properties of the flow [4, 42]. In particular, Richardson's energy cascade theory for fully turbulent flow established that the instabilities in the flow created large eddies which then quickly evolved into smaller vortices due to inertial instabilities. Later, Kolmogorov developed the theory of self similarity in which very small eddies possess nearly universal statistical characteristics.

An important related finding for turbulent shear flows is the *law of the wall*, which characterizes the mean behavior of these flows as a function of the distance from the wall [42]. In particular, the velocity profile in the inner layer (also referred to as the constant stress region) varies linearly with the distance to the wall since viscosity dominates the flow. The outer layer on the other hand is dominated by Reynolds stresses, which results in an inviscid flow. The region between the inner and outer layers is commonly referred to as the buffer or log layer, where the viscous and Reynolds stresses are approximately equal in magnitude in this region. The most important result from this study is the relationship between the

turbulent scale and the Reynolds number.

The basis of such theoretical approaches to turbulence has been to implement statistical methods to characterize the flow. Although it is generally agreed that such methods have successfully described turbulent shear flows to some extent, it does not satisfactorily describe the dynamic behavior of the flow. Thus, the focus of this dissertation will be to further understand turbulence using a dynamical systems approach. Specifically, the laminar–turbulent boundary of two shear flows will be characterized in detail.

1.1 Motivation

Turbulence is a ubiquitous phenomenon that is observed in nature. It is generally characterized by irregular or unstable flow and can be regarded as a disarray of scales where small structures intermix with larger ones. Whether it is used as a method of enhancing certain properties of systems, such as mixing, or to control undesirable behavior, the manipulation of turbulence is a powerful tool that can be used to for many systems. It has often been used to enhance the mixing properties and/or the efficiency of systems which lack such dynamics. One of the earliest references to the notion of turbulent flows was provided by Leonardo da Vinci in the late 15th century when he made an attempt to study the flow of displaced water. Da Vinci observed the different patterns that water made when

it flowed around obstacles.

The transition from laminar to turbulent flow in a pipe was pointed by Reynolds in 1883. Pipe flow is a pressure-driven shear flow in a long and straight pipe of circular cross section. In his experiment, he observed that the transition in pipe flow between the two regimes (laminar and turbulent) was controlled by the dimensionless quantity $Re = ud/\nu$, where u is the mean velocity of the flow, d is the diameter of the pipe, and ν is the kinematic viscosity of the fluid. The remarkable outcome of his experiments was that the transition spontaneously occurred at a critical value of $Re \sim 2000$ [46]. This result was intriguing because (1) he observed that laminar flow was stable for Re up to approximately 13000; (2) no turbulence was detected below this critical value; and (3) this critical value is very sensitive to perturbations at the entrance of the pipe. Reynolds's stunning findings have remained a mystery ever since, and have motivated a community of scientists and engineers to pursue efforts to further understand the transition to turbulence.

Pipe flow is in a class of shear flows which includes plane Couette flow and sinusoidal shear flow. One outstanding characteristic of these flows is that they exhibit simple geometries, but the way in which they become turbulent is still unknown. The substantial interest in such flows derives from the fact that turbulence develops despite linear stability of the laminar profile. Indeed, hydrodynamic stability theory predicts that the laminar state for these shear flows remains stable

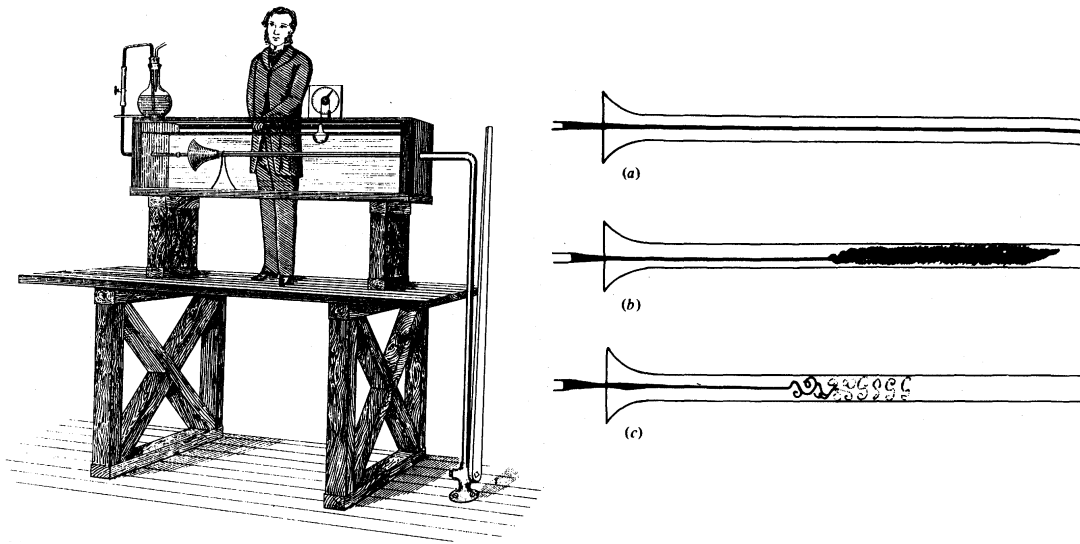


Figure 1.1: Sketch of Reynolds's experiment (left) and the typical types of flows he observed (right). (Figure obtained from [46])

for all Reynolds numbers [12]. This implies that for these flows, turbulence arises abruptly rather than through a sequence of transitions from the laminar state to more and more complicated behavior as some parameter value is increased. For other shear flows such as plane Poiseuille flow and parallel shear flow, the laminar state loses stability at a value of the Reynolds number higher than values for which turbulence is found.

1.2 The Transition to Turbulence

The transition to turbulence in shear flows has been studied for a very long time. This is mainly due to the fact that the transition from laminar to turbulent

flow is complicated and not easily understood. The issue is not when turbulence emerges in the flow, but rather why it appears and what mechanisms in the flow trigger this phenomenon. Moreover, the transition process distinctively depends on the geometry, parameters, and initial conditions of the flow, thus, there is little hope in finding a single mechanism that drives the transition process in these flows. Previous studies have hypothesized and suggested various routes by which turbulence can be triggered in these flows, which include methods such as studying various types of flow instabilities, analyzing coherent structures, and developing reduced-order models. The following section will highlight some of these important methods used to characterize the transition to turbulence.

The conventional method which is suggested to give a good understanding of the transition process involves instabilities in the flow [47]. The principal idea behind this is that predominant instabilities exponentially grow to excite subsequent instabilities that lead to the typical turbulent dynamics observed in many of these flows. In essence, these small disturbances can grow in the linear regime to a size where nonlinear effects become important in the flow and trigger secondary disturbances which amplify to excite subsequent instabilities and breakdown of the flow occurs. The general notion of the transition process can be described for a boundary layer as follows [47]. The flow is initially dominated by streaks of high and low speed fluid which are pulled away from the wall by disturbances via

a lift-up process where nonlinear streamwise vortices are generated. Flows with strong inflection points in the mean streamwise profile create additional instabilities which grow exponentially and generate the dynamics necessary for turbulent flow.

The transition to turbulence is a difficult problem and a comprehensive description of the process is yet to be described. For this reason, reduced-order models have been developed in an attempt to describe the transition process and unearth mechanisms that can trigger turbulence in these flows. For example, low-dimensional models have been derived from Galerkin projection onto Fourier modes for sinusoidal shear flow in [61, 62, 63, 13, 48, 33, 34], and models for plane Couette flow have been derived using proper orthogonal decomposition by [36, 53]. The reduced-order models are not limited to ordinary differential equations; for example, the Swift-Hohenberg system can be described by simpler partial differential equations as shown in [30, 29]. The goal is to use low-dimensional models, composed of a set of ordinary differential equations, which provide a simplified description of the dynamics of a complex system. Provided that a reduced-order model successfully captures the behavior of the full system, a plethora of information can be obtained about the dynamics of the system without significant computational costs by using tools that are advantageous for reduced-order systems.

One technique frequently used to derive such reduced-order models is proper orthogonal decomposition [52]. This method captures the dominant components of a complex system, such as the average energy in the system, from data obtained from experiments or numerical simulations. Models derived using proper orthogonal decomposition have also been studied for turbulent boundary layers [1], channel flow [43], and transitional shear-layer flows [41]; see also the references in [45]. Standard proper orthogonal decomposition analysis does not guarantee the best model in terms of capturing the dynamics of the system [52]. This is due to the fact that proper orthogonal decomposition produces sets of modes which contain the most energy in the system, a quantity which may be a poor indicator of the key structures participating in the dynamics of the flow. However, in the last few years, many advances have been made in developing proper orthogonal decomposition methods which look beyond the energy content of the system as a measure of importance to the dynamics [24].

One topic of much debate in the development of these low-dimensional models has been regarding on the mechanisms that play an important role in the transition to turbulence. In particular, Waleffe emphasized that the transition process is governed by the dynamics of nonlinear self-sustained solutions rather than by non-normal linear mechanisms [62]. He constructed a simple 4-dimensional nonlinear model which captured the dynamics of prominent components of the *self-*

sustaining process observed in the full Navier–Stokes system. The self-sustaining process, which was observed in direct numerical simulations of turbulent shear flows, is a nonlinear process analyzed by Waleffe where the streamwise vortices stimulate the formation of streaks that become unstable over time. The nonlinear self–interaction of these unstable streak modes, in turn, generate streamwise-dependent flow which allows for the streamwise vortices to regenerate and the process to repeat. It has been argued that this self–sustaining process is a universal characteristic of shear flow turbulence [23, 63, 44, 25, 26].

Another class of low–dimensional models considered for studying the transition process gives an emphasis on the non-normal growth of linear mechanisms in the flow. Most notably, Baggett, Driscoll, and Trefethen developed a 3–dimensional model which considers transient energy growth as a mechanism for triggering nonlinear effects that lead to turbulence [2]. In particular, the nonlinear terms are treated as a generic mixer where their purpose is to sustain the linear dynamics via a bootstrapping method. While this method of describing the mechanism of the transition process is different from Waleffe’s, it has been suggested that transient energy growth provides a good basis for understanding the transition of turbulence in flows where turbulence exists for parameter values where the laminar state is stable; see e.g. [6, 57]. For a review of models emphasizing transient energy growth arising from non-normality, see [3].

Although a great deal of research has been dedicated to study the transition to turbulence using low-dimensional techniques, it does not fully capture the physical quantities in the transition. In particular, these low-dimensional models have not been able to identify critical mechanisms or structures that trigger turbulence in shear flows. As a result, direct numerical simulations of the Navier–Stokes equations have been used in order to better understand the transition to turbulence. For turbulent shear flows, turbulence can be obtained by increasing the amplitude of a perturbation about the laminar state, provided some critical value of Reynolds number is exceeded. It has been suggested that the emergence of unstable steady states [37, 38, 39, 40, 8, 64, 65, 16, 67, 14, 26, 58, 59, 22] in various flows can provide knowledge about the critical parameter values for which turbulent behavior can be observed in a particular system. The governing equations for these flows possess numerous branches of these unstable steady states that arise from saddle–node bifurcations [37, 7, 48, 15], similar to the traveling wave solutions found in pipe flow [16, 67]. In plane Couette flow, the “upper branch” solution which arises in a saddle–node bifurcation and undergoes successive bifurcations has properties characteristic of turbulence while the “lower branch” solution, which seems to remain intact, seems to be associated with the transition to turbulence [66, 8, 65]. These unstable steady states are exact coherent structures which have stable and unstable manifolds that intertwine in state space. It

has been hypothesized that this convolution, in which trajectories enter and exit, allows for the turbulent dynamics observed in these shear flows. Despite the fact that these coherent states have been found and studied, the explicit relationship between these three-dimensional solutions and turbulence is still not known.

1.3 The Governing Equations for Fluid Flow

The equations governing fluid flow are known as the Navier-Stokes equations and describe the conservation of mass and momentum of a fluid. They can be derived by applying Newton's second law to a small mass of fluid, with volume δV , as it moves through a flow field, which gives:

$$(\rho\delta V)\frac{D\mathbf{u}_{tot}}{Dt} = -(\nabla p_{tot})\delta V + (\rho\delta V)\mathbf{f}_v + (\rho\delta V)\mathbf{f}_b, \quad (1.1)$$

where ρ is the fluid density, \mathbf{u}_{tot} is the total velocity field, and p_{tot} is the total pressure. The viscous forces (per unit mass) \mathbf{f}_v arise from viscous stresses, and \mathbf{f}_b is the net body force (per unit mass) in the flow. The total viscous force acting on a volume of fluid and exerted in the i^{th} direction is given by:

$$f_i = \sum_j \frac{\partial \tau_{ji}}{\partial x_j}, \quad \tau_{ij} = \nu \left\{ \frac{\partial u_i}{\partial x_j} + \frac{\partial u_j}{\partial x_i} \right\}, \quad (1.2)$$

where ν is the kinematic viscosity. Substituting (1.2) into (1.1), dividing by $(\rho\delta V)$, and simplifying gives:

$$\frac{D\mathbf{u}_{tot}}{Dt} = -\frac{1}{\rho}\nabla p_{tot} + \nu\nabla^2\mathbf{u}_{tot} + \mathbf{f}_b. \quad (1.3)$$

The rate of change of a property of the fluid mass as it moves around can be obtained using the chain rule. For simplicity, consider the change in the density of a fluid $\rho(\mathbf{x}, t)$ due to small spatial and temporal variations, $\delta\mathbf{x} = \mathbf{u}_{tot} \delta t$ and δt , respectively:

$$\delta\rho = \rho(\mathbf{x} + \mathbf{u}_{tot} \delta t; t + \delta t) - \rho(\mathbf{x}, t). \quad (1.4)$$

Expanding (1.4) to first order in δt gives:

$$\delta\rho = \delta t \frac{\partial\rho}{\partial t} + u_x \delta t \frac{\partial\rho}{\partial x} + u_y \delta t \frac{\partial\rho}{\partial y} + u_z \delta t \frac{\partial\rho}{\partial z}. \quad (1.5)$$

Therefore, the change in density following a fluid particle is:

$$\frac{D\rho}{Dt} = \frac{\delta\rho}{\delta t} = \frac{\partial\rho}{\partial t} + (\mathbf{u}_{tot} \cdot \nabla)\rho. \quad (1.6)$$

Similarly,

$$\frac{D\mathbf{u}_{tot}}{Dt} = \frac{\partial\mathbf{u}_{tot}}{\partial t} + (\mathbf{u}_{tot} \cdot \nabla)\mathbf{u}_{tot}, \quad (1.7)$$

so (1.3) can be rewritten as

$$\frac{\partial\mathbf{u}_{tot}}{\partial t} + (\mathbf{u}_{tot} \cdot \nabla)\mathbf{u}_{tot} = -\frac{1}{\rho}\nabla p_{tot} + \nu\nabla^2\mathbf{u}_{tot} + \mathbf{f}_b. \quad (1.8)$$

The continuity equation, which captures the conservation of mass for a fluid, is given by

$$\frac{\partial\rho}{\partial t} + \nabla \cdot (\rho\mathbf{u}_{tot}) = 0. \quad (1.9)$$

This study will exclusively consider incompressible fluids, that is, fluids for which

$D\rho/Dt = 0$. As a result of this constraint, (1.9) and (1.8) can be written as

$$\nabla \cdot \mathbf{u}_{tot} = 0, \quad (1.10)$$

$$\frac{\partial \mathbf{u}_{tot}}{\partial t} + (\mathbf{u}_{tot} \cdot \nabla) \mathbf{u}_{tot} = -\frac{1}{\rho} \nabla p_{tot} + \nu \nabla^2 \mathbf{u}_{tot} + \mathbf{f}_b, \quad (1.11)$$

which are the equations governing the evolution of fluid flow.

1.4 Dynamical Systems Theory

Understanding the long term behavior of systems is often of interest, especially when it pertains to studying turbulent shear flows. The behavior of such systems can be analyzed using dynamical systems techniques. The following section will provide a broad overview of some key elements of dynamical systems theory [21, 68] that will be used to analyze the Navier-Stokes equations.

Consider the following set of differential equations as a dynamical system

$$\frac{d\mathbf{x}}{dt} \equiv \dot{\mathbf{x}} = f(\mathbf{x}; \mu), \quad (1.12)$$

where $\mathbf{x} \in \mathbb{R}^n$ is a state of the system (1.12) at a given time $t \in \mathbb{R}$. The system depends on a set of parameters $\mu \in \mathbb{R}^p$ such as the Reynolds number. The dynamics are specified by the vector field $f : \mathbb{R}^n \times \mathbb{R}^p \rightarrow \mathbb{R}^n$. Systems in the form of (1.12) are commonly known as *autonomous* since the vector field does not have an explicit time dependence.

Solutions of differential equations depend on initial conditions and parameters. For shear flows, it is very useful to study the explicit dependence of solutions on parameters. In particular, it is of interest to determine any qualitative changes in the system, for example, how the variation of the Reynolds number can influence turbulence. The principal solutions that will be of interest in this study are equilibria and periodic orbits.

1.4.1 Equilibria

An *equilibrium* point, also called a fixed point, is a solution of a dynamical system that does not change in time. Such a solution for (1.12) is a point $\mathbf{x} \in \mathbb{R}^n$ such that $f(\mathbf{x}; \mu) = 0$. A stability analysis determines how neighboring solutions behave. In particular, if all neighboring solutions decay to a given solution, then that solution is said to be stable. In practice, there are two fundamental definitions of stability for equilibrium points. If $\mathbf{x}(t)$ is a solution of (1.12), then $\mathbf{x}(t)$ is said to be *Lyapunov stable* if for a given $\epsilon > 0$, there exists $\delta = \delta(\epsilon) > 0$ and some t_0 such that for any other solution of (1.12) $\mathbf{y}(t)$

$$|\mathbf{x}(t) - \mathbf{y}(t)| < \delta \implies |\mathbf{x}(t) - \mathbf{y}(t)| < \epsilon, \quad \forall t > t_0. \quad (1.13)$$

This implies that solutions starting near $\mathbf{x}(t)$ at a given time will remain close to $\mathbf{x}(t)$ for all future times.

A stronger definition of stability is *asymptotic stability* which holds when an

equilibrium point is both Lyapunov stable and attracting. In particular, $\mathbf{x}(t)$ is asymptotically stable if it is Lyapunov stable and for any other solution $\mathbf{y}(t)$ of (1.12), there exists a constant $\delta > 0$ such that

$$|\mathbf{x}(t_0) - \mathbf{y}(t_0)| < \delta \implies \lim_{t \rightarrow \infty} |\mathbf{x}(t) - \mathbf{y}(t)| = 0. \quad (1.14)$$

Hereafter, solutions that are asymptotically stable will simply be called stable.

The stability of the equilibrium \mathbf{x}_p can be calculated via a linearization of the dynamical system about the equilibrium in the following manner. Letting $x = \mathbf{x}_p + y$, substituting this into (1.12) and Taylor expanding about the equilibrium point gives:

$$\dot{y} = Df(\mathbf{x}_p; \mu)y + \mathcal{O}(|y|^2), \quad (1.15)$$

where Df is the Jacobian matrix. The equilibrium \mathbf{x}_p is asymptotically stable if and only if all the eigenvalues of the Jacobian have negative real parts; otherwise, if any of the eigenvalues have positive real parts, then the equilibrium point is unstable.

If the Jacobian $Df(\mathbf{x}_p; \mu)$ has n_s (respectively, n_u) eigenvalues with negative (respectively, positive) real part, then the equilibrium \mathbf{x}_p will have an n_s -dimensional stable (respectively, n_u -dimensional unstable) manifold. This is an invariant manifold which consists of all points in \mathbb{R}^n which give trajectories that asymptotically approach \mathbf{x}_p as $t \rightarrow \infty$ (respectively, $t \rightarrow -\infty$).

1.4.2 Periodic Orbits

Another important type of solution that will be studied in this dissertation is a *periodic orbit*, which is a solution that repeats itself. More specifically, periodic orbits are solutions for which

$$\mathbf{x}(t) = \mathbf{x}(t + T), \quad \forall t \in \mathbb{R}, \quad T > 0. \quad (1.16)$$

For planar systems, the existence of periodic orbits can be established by using methods such as index theory, Dulac's criterion, the Poincaré-Bendixon Theorem, etc. For higher dimensional systems, periodic orbits typically need to be found numerically. The stability of a periodic orbit is determined by considering a Poincaré map. Consider the vector field (1.12) and let the Poincaré section Σ be an $(n - 1)$ -dimensional surface transverse to the vector field. Then, the Poincaré map P is the map which takes a point x_0 to its first return to Σ . Now, suppose that x_0 lies on a periodic orbit with period T such that $P(x_0) = x_0$; such a fixed point of the map P corresponds to a periodic orbit of the vector field (1.12). Therefore, the stability of a periodic orbit is determined by the eigenvalues of $DP(x_0)$. In particular, if all the eigenvalues of the Jacobian are in the unit circle, then the periodic orbit is said to be stable; otherwise, it is unstable.

If $DP(x_0)$ has n_s (respectively, n_u) eigenvalues inside (respectively, outside) the unit circle, then the periodic orbit which passes through x_0 will have an $(n_s + 1)$ -dimensional stable (respectively, $(n_u + 1)$ -dimensional unstable) manifold. This is

an invariant manifold which consists of all points in \mathbb{R}^n which give trajectories that asymptotically approach the periodic orbit as $t \rightarrow \infty$ (respectively, $t \rightarrow -\infty$).

1.4.3 Invariant Manifolds

Invariant manifolds will play a critical role in the notion of a laminar–turbulent boundary in turbulent shear flows. In particular, the manifolds of the invariant structures embedded in the laminar–turbulent boundary will be important for the dynamics in this boundary. In order to divide state space into two regions, invariant solutions with a single unstable direction will be found such that its codimension–1¹ stable manifold can separate trajectories which decay to the laminar state without becoming turbulent from those which become turbulent. This manifold will be referred to as the *edge of chaos*.

1.5 Scope of the Dissertation

This dissertation will focus on characterizing the edge of chaos for two similar turbulent shear flows: sinusoidal shear flow and plane Couette flow. The linear stability of the laminar state for these flows indicates that infinitesimal perturbations will decay despite high Reynolds numbers. A dynamical systems approach will be used in order to further understand the transition to turbulence and iden-

¹Codimension is the number of directions normal to the manifold. A codimension–1 manifold can be thought of as a surface dividing the infinite dimensional space of a dynamical system.

tify the structures living in the border of the laminar and turbulent regimes.

Chapter 2 will introduce the notion of a laminar–turbulent boundary that separates two qualitatively distinct regions in phase space. Trajectories near this boundary visit near a subset in state space which is invariant under the flow and attracting for initial conditions on this boundary. A method of finding this boundary, which involves tracking the time evolutions of velocity fields, will be discussed in detail. A literature review of the previous studies of such a boundary will be given at the end of the chapter.

The laminar–turbulent boundary will be discussed in Chapter 3 for a nine-dimensional model for sinusoidal shear flow. The sinusoidal shear flow model has trajectories which either decay to the laminar state, become transiently chaotic before decaying to the laminar state, or become transiently chaotic before moving towards a nontrivial attractor. Due to the dimensionality of the system, a probabilistic numerical scheme will be used to characterize the boundary. Furthermore, the basins of attraction for the laminar and nontrivial attractor states will be studied in order to characterize how they coexist in phase space.

In Chapter 4, the edge of chaos for plane Couette flow will be explored for various ranges of Reynolds numbers and channel sizes. An iterated edge tracking algorithm, based on a bisection method, will be used to identify structures in the laminar–turbulent boundary. Properties of these structures, called edge states,

will be classified in detail. Furthermore, the coexistence of multiple edge states for a small range of channel sizes and Reynolds numbers will be discussed.

Finally, concluding remarks on the edge of chaos for turbulent shear flows will be given in Chapter 5.

Chapter 2

The Edge of Chaos

For turbulent shear flows, such as sinusoidal shear flow and plane Couette flow, the linear stability of the laminar state indicates that even at high Reynolds numbers, sufficiently small perturbations to the laminar state will decay. Nevertheless, turbulent dynamics are observed for these flows. Experimental and numerical analysis presents strong evidence that the turbulent state coexists in state space with the stable laminar state and has suggested that trajectories do not remain turbulent forever. With the present scenario, it is conceivable to imagine that there exists some border in state space that partitions initial conditions that lead to decay to the laminar state without exhibiting turbulence from those that grow and lead to turbulence. This chapter will address the notion of such a laminar–turbulent boundary in shear flows as a hallmark for understanding the transition

to turbulence. The nature of this boundary will be studied by observing the distributions of turbulent *lifetimes* which measure the duration of the chaotic transient associated with turbulence. The differing behavior of the lifetimes from smooth variations to rapid fluctuations corresponding to a high sensitivity of initial conditions suggests the name *edge of chaos* to describe the boundary separating the two states. The dynamics on the edge of chaos will be studied and the structures living in it will be discussed. Finally, a summary of previous studies of the edge of chaos, conducted for similar shear flows, will be presented.

2.1 The Laminar–Turbulent Boundary

For a shear flow, an arbitrary initial condition can either lead to decay to the laminar state without exhibiting turbulence or can lead to turbulence. Since the laminar and turbulent states can coexist, this suggests that there may exist a boundary which separates these two regimes, such that initial conditions on one side of this boundary will decay to the laminar state without exhibiting turbulence and initial conditions starting on the other will lead to turbulence. If such boundary exists, what would its nature and geometry be, simple or complex? Figure 2.1 illustrates this concept and shows a 2–dimensional sketch of the laminar–turbulent boundary in state space. In this visualization, the plane represents the infinite–dimensional state space. The laminar state is represented by a

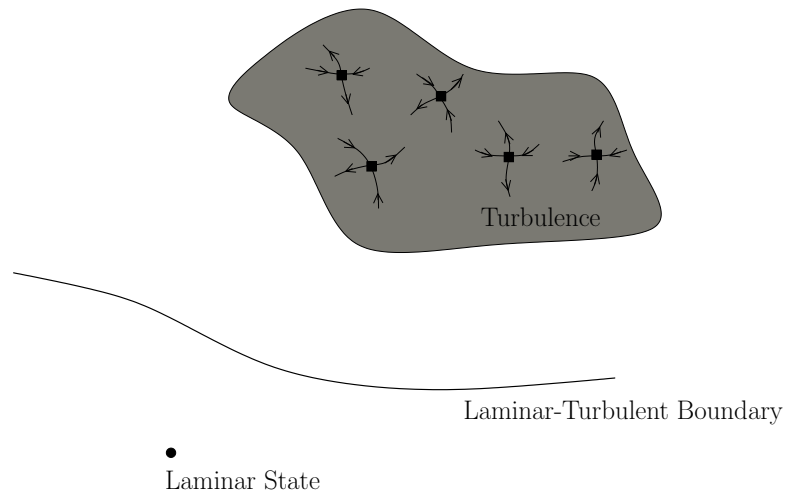


Figure 2.1: 2-dimensional sketch of the laminar-turbulent boundary in state space.

circle to which infinitesimal perturbations monotonically decay. In a completely different region of state space, there exists a turbulent state which is represented by the gray area in Figure 2.1. It has been suggested that the turbulent dynamics in linearly stable shear flows are generated by chaotic structures. Indeed, this notion of the hyperbolic structure of the turbulent state has been ratified by the discovery of unstable steady states which appear in saddle-node bifurcations in flows such as plane Couette and pipe flow [37, 7, 48, 15, 16, 67]. The hyperbolic structure, in particular, a chaotic saddle is characterized by positive Lyapunov exponents and exhibits the long chaotic transients before decaying to equilibria or periodic orbits [21], as observed in many of these shear flows.

The objective of this research is to try to identify the structures that compose

the boundary which separates these two regimes where initial conditions lying on this surface will neither decay to the laminar state nor grow and become turbulent. Understanding this boundary may help to answer the century–old question of the transition to turbulence in shear flows.

2.2 Geometry of the Boundary

In practice, the laminar–turbulent boundary can be studied by observing the time evolution of velocity fields. Every initial condition gives a unique trajectory that will either swing up to turbulence or decay to the laminar state without exhibiting turbulence, see Figure 2.2. A straightforward measure which can be used to find this boundary is to assign a *lifetime* to the perturbations, that is, the time that it takes for a trajectory with a given initial condition to decay to within some neighborhood of the laminar state [51, 49].

Generally, the lifetime of a perturbation increases as the Reynolds number and/or the perturbation amplitude increases. When the amplitude of the perturbations to the laminar state is increased, there are changes between areas of smooth variations of lifetimes, corresponding to trajectories directly decaying to the laminar state, and areas with high fluctuations in lifetimes consistent with a high sensitivity with respect to initial conditions [17]. Figure 2.3 shows a typical contrast of lifetimes for the low-dimensional model for sinusoidal shear flow

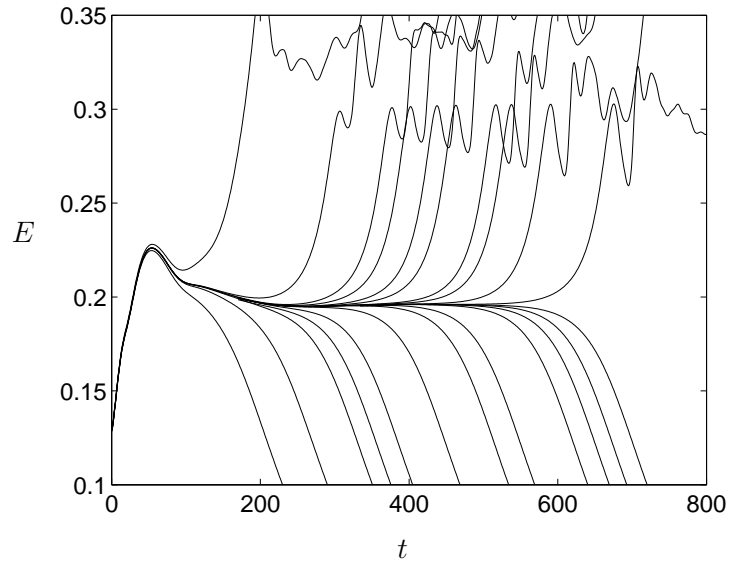


Figure 2.2: Trajectories on either side of the laminar–turbulent boundary. When E is high, the system is turbulent. $E = 0$ corresponds to the laminar state.

from [33]. The left panel shows the lifetime of perturbations as a function of the scaling amplitude $\sqrt{E_0}$, where E_0 is the initial energy of a perturbation with fixed shape with respect to the laminar state. The smooth regions, corresponding to perturbations which quickly decay to the laminar state, are undoubtedly different from regions with rapid fluctuations which are indicative of the sensitive nature of the initial conditions. Alternatively, the lifetime of perturbations with fixed shape as a function of Reynolds numbers is shown in the right panel of Figure 2.3. The clear difference between the laminar region, corresponding to short lifetimes, from the chaotic region where lifetimes reach the numerical limits is evident for the three different scaling amplitudes shown. These lifetime studies can give an

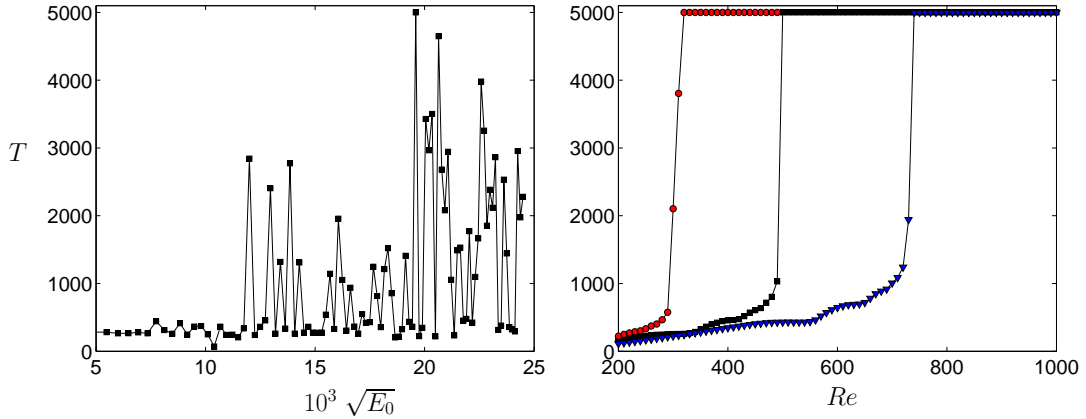


Figure 2.3: Turbulent lifetimes T for a low-dimensional model for sinusoidal shear flow. (Left) At $Re = 300$, the lifetime of perturbations is plotted as a function of the scaling amplitude $\sqrt{E_0}$, where E_0 is the initial energy of a perturbation, with fixed shaped, with respect to the laminar state. The points clearly show the difference between smooth (up to $10^3\sqrt{E_0} \approx 12$) and rapidly fluctuating (above $10^3\sqrt{E_0} \approx 12$) regions which gives an indication of when the turbulence arises in the system. Similarly, (right) the lifetime as a function or Reynolds number for three different values of scaling amplitudes (red circles) $\sqrt{E_0} = 0.022$ (black squares) $\sqrt{E_0} = 0.01$ (blue triangles) $\sqrt{E_0} = 0.0095$ determines the critical Reynolds number needed to trigger turbulence for that perturbation.

indication of the critical value of the perturbation amplitude needed to observe turbulence in the system for a particular value of the Reynolds number. The nature of the fluctuations in the lifetimes has led to the coining of the term *edge of chaos* to describe the points lying on the boundary between smooth and rapidly fluctuating regions [51].

A different lifetime study was conducted for this low-dimensional model for sinusoidal shear flow in [32]. This model, which captures the key dynamics of turbulent shear flows, demonstrates that the behavior of the perturbations is highly sensitive to initial conditions. Figure 2.4 shows the lifetimes of perturbations for

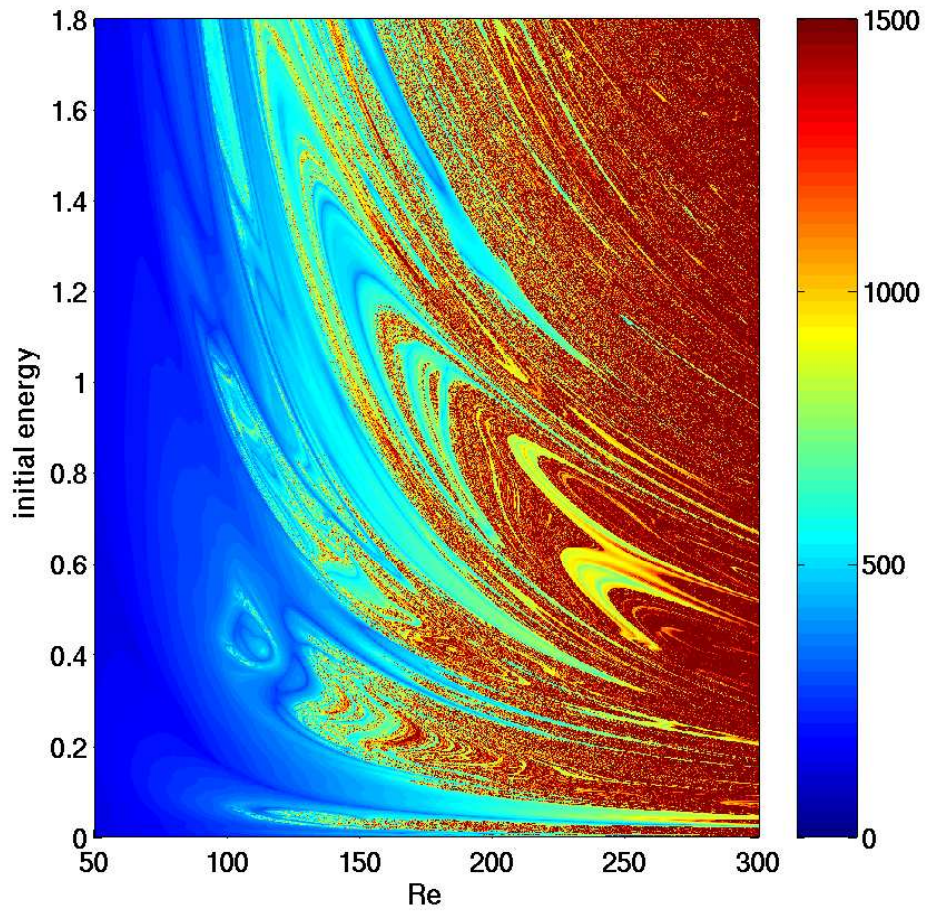


Figure 2.4: Lifetimes of perturbations for different initial energies and Reynolds numbers for a low-dimensional model for sinusoidal shear flow. (From [32]).

a range of Reynolds numbers and initial energy where the transition is believed to occur. The border between initial conditions that decay and grow is not smooth, but rather fractal in nature.

2.3 Dynamics on the Edge of Chaos

A point on the boundary of the laminar and turbulent regions is said to live on the edge of chaos. It has been shown that points lying on the edge of chaos are dynamically connected to *edge states* which are structures that are invariant under the flow and attracting for initial conditions on the edge. They are only relative attractors, since they are unstable under perturbations outside of the laminar–turbulent boundary. The edge state is energetically distinct from the laminar and turbulent states; the edge of chaos, which contains the edge state, is a subset of state space and sustains its own dynamics.

The notion of an edge of chaos is that it separates laminar dynamics from turbulent behavior in state space. In order for this to occur, the invariant state that trajectories restricted to the edge approach and which are embedded in the edge must have only one unstable direction. Figure 2.5 sketches the dynamics on and around the edge of chaos. Trajectories starting on the edge of chaos are dynamically attracted to the edge state whose stable manifold forms the edge. Trajectories in the neighborhood of (but not on) the edge will tend towards the edge state but are pulled away to the laminar or turbulent state by the one–dimensional unstable manifold of the edge state. This scenario then allows the codimension–1 stable manifold of the edge state to separate trajectories which directly decay to the laminar state from those that become transiently chaotic.

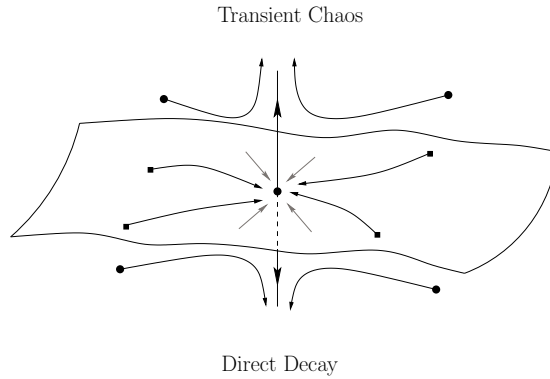


Figure 2.5: A sketch of the dynamics associated with the edge of chaos. Trajectories starting on the edge, represented by squares, are dynamically attracted to the edge state (center circle) whose codimension-1 stable manifold forms the edge of chaos. Neighboring trajectories, represented by circles, will tend towards the edge state but will be pulled away by the unstable manifold of the edge state.

2.4 Previous Studies of the Edge of Chaos

The edge of chaos has been characterized for several low-dimensional models and full direct numerical simulations of shear flows. The collective results suggest that the edge of chaos for these flows can be composed of simple structures, such as equilibria, or complex states, such as traveling waves and relative periodic orbits. Most of these boundaries have been found by means of calculating the lifetime of velocity fields or by employing a bisection method to bracket a state in between the laminar and turbulent regimes. The following presents a literature review of the results obtained for finding the edge of chaos for parallel shear, pipe, and plane Couette flows.

2.4.1 Parallel Shear Flow

In [51], the edge of chaos was studied for a low-dimensional model for parallel shear flow, where incompressible fluid is confined by no-slip parallel walls which are a distance d apart. This nine-dimensional model was derived via a Galerkin projection for parallel shear flow [48]. Trajectories in this system either decay directly to the laminar state or become transiently chaotic. The edge was numerically tracked by bisecting between points¹ on a one-dimensional curve which connects the laminar and turbulent states. The distance between these points is incrementally reduced to approximate the edge points that lie in between them. It was found that for moderately small Reynolds numbers ($Re < 402$), the edge is a smooth surface which coincides with the stable manifold of a symmetric pair of periodic orbits. As the Reynolds number is increased, within this range, the periodic orbits undergo bifurcations where old orbits gain additional unstable directions and new ones emerge from the bifurcation point with only one unstable direction.

For this system, the pair of symmetric periodic orbits associated with the edge of chaos is unique for this range of Reynolds numbers, that is, for every Reynolds number, there is at most one pair of such periodic orbits present in phase space.

¹A point near the laminar state origin and a second point near the chaotic saddle are used in the bisection algorithm and straddle the edge point. The points are chosen to be below and above the threshold value based on a maximization problem, which is a different method from what is used in Chapters 3 and 4.

The edge is then formed by the union of the stable manifolds of this symmetric pair of periodic orbits. At $Re \approx 402$, no new periodic orbits with an eight-dimensional stable manifold appear from bifurcations. Instead, for $Re > 402$, trajectories on the edge of chaos are no longer asymptotically periodic, but rather chaotic, and trajectories on the edge are dynamically attracted to a high-dimensional fractal object in the form of a relative attractor. This analysis suggests that for a given Reynolds number, all edge points are contained on the stable manifold of an invariant structure that lives in between the laminar and turbulent domains in state space.

2.4.2 Pipe Flow

Direct numerical simulation of the Navier–Stokes equations was used to identify the edge of chaos in pipe flow [49] using the techniques developed in [51]. Pipe flow is a type of shear flow in which incompressible fluid is driven by pressure in a perfectly circular and infinitely long pipe. In particular, a lifetime study was used to track the dynamics on the edge of chaos for pipe flow. To find the edge, a bisection algorithm was implemented to obtain a pair of initial conditions on either side of the edge. To ensure that the edge state was tracked, successive refinements determined new pairs of trajectories near the boundary. It was found that the edge state for this system was attracting for initial conditions restricted

in the edge, but repelling for initial conditions perpendicular to it. In addition, the edge state is chaotic and remains the edge state for a wide range of Reynolds numbers. Moreover, the dynamics of the edge state, which was dominated by streaks and streamwise vortices, remained qualitatively unchanged.

2.4.3 Plane Couette Flow

Plane Couette flow is the flow of an incompressible fluid which is confined between two infinitely parallel plates moving in opposite directions at constant and equal velocities. Recent studies of the edge of chaos in plane Couette flow for the fully-resolved Navier-Stokes equations has revealed that trajectories in the neighborhood of the laminar-turbulent boundary approach invariant states such as hyperbolic fixed points, traveling waves, or periodic orbits [50, 31]. An iterated edge tracking algorithm, based on a simple bisection algorithm, was used by [50] to track the transition boundary for a flow domain that is 4π units long, 2π units wide, and 2 units high at a Reynolds number of $Re = 400$. It was found that trajectories in the neighborhood of the edge visit near one of three states. However, upon calculating the number of unstable directions for each state, it was confirmed that only one of those states had a codimension-1 stable manifold. Since the other states have stable manifolds with codimension higher than one, they cannot by themselves divide state space into two regions. Therefore, the

state with the single unstable direction is the edge state that is associated with the edge of chaos.

This study was extended for a wide range of flow domains and it was found that edge states can be classified as fixed points or traveling waves depending on the geometry of the flow [31]. In all cases, it was found that streaks are the dominant structures in these edge states. For channel lengths greater than 8π units, the trajectories on the edge converged to invariant states which were more complex in structure. The highlight of this investigation was the discovery of spatially localized² edge states for the plane Couette system. In particular, for domains with a width of 2π units and length longer than 32π units, the edge state localizes and exponentially decays in the streamwise direction. Spanwise localization of edge states was also observed for wide channels with domains greater than 8π units. It was found that when the edge state is localized, the shape of the edge state is not dependent on the size of the flow domain, being localized both in the streamwise and spanwise directions. However, the edge tracking algorithm never converged to simple structures in this range of computational domains suggesting that trajectories near the edge visit near complex invariant states such as a chaotic saddle.

A related study considered the properties of unstable states for plane Cou-

²The localization of an edge state refers to the confinement of streaks within the flow domain such that there exists a laminar region alongside the streaks.

ette flow which undergo a saddle–node bifurcation, as mentioned in §1.1. One of these, the “upper branch”, which is subject to subsequent bifurcations as Reynolds number increases, has been associated with the turbulent state since it captures dominant statistics of turbulent shear flows [66, 55]. The “lower branch”, on the other hand, does not bifurcate and appears to only have one unstable direction. This finding suggests that these lower–branch states are associated with a boundary that separates the basins of attraction of the laminar and turbulent states, which allows for a strong correlation of this lower branch to the transition to turbulence [65, 63].

Chapter 4 will extend the studies of [31, 50] by examining the coexistence of multiple edge states in a small range of flow domains for plane Couette flow. A detailed description of the iterated edge tracking algorithm will be presented along with a discussion on methods used to classify these edge states.

Chapter 3

The Edge of Chaos for a Low-Dimensional Model

In this chapter, the laminar-turbulent boundary of a low-dimensional model for sinusoidal shear flow is characterized. This flow, in which incompressible fluid is driven by a time-independent sinusoidal body force in the streamwise direction between two free slip walls, is modeled as a nine-dimensional ordinary differential equation by projecting the full Navier-Stokes equations onto a set of physically meaningful modes. The model has a stable laminar state for all Reynolds numbers, but the decay to it can proceed in two qualitatively different ways – direct and through transient chaos. Two numerical schemes are implemented in this analysis, a systematic and probabilistic one, to detect and characterize the boundary

between initial conditions exhibiting one versus the other type of decay. Furthermore, for $330 < Re < 515$, there exists an additional stable attractor which is associated with sustained turbulent behavior. A probabilistic study is used to characterize the basin of attraction for that attractor. Finally, the way in which the basins of attraction for the laminar and turbulent states relate to each other in the phase space is discussed. The results from this chapter were published in [28].

3.1 A Low-Dimensional Model for Sinusoidal

Shear Flow

In the following, consider sinusoidal shear flow which represents a nontrivial shear flow in which incompressible fluid between two free-slip walls experiences a time-independent streamwise sinusoidal body force, see Figure 3.1. A coordinate system such that the x -axis is parallel to the walls, the y -axis is perpendicular to the wall, and the z -axis is perpendicular to both x and y is chosen for this flow. Note that x , y , and z respectively correspond to the streamwise, wall-normal, and spanwise directions. Although it is difficult to obtain experimentally, sinusoidal shear flow is amenable to analytical treatment, unlike other shear flows, and it is hoped that the knowledge gained from studying this flow can make important contributions to understanding other relevant turbulent shear flows such as plane

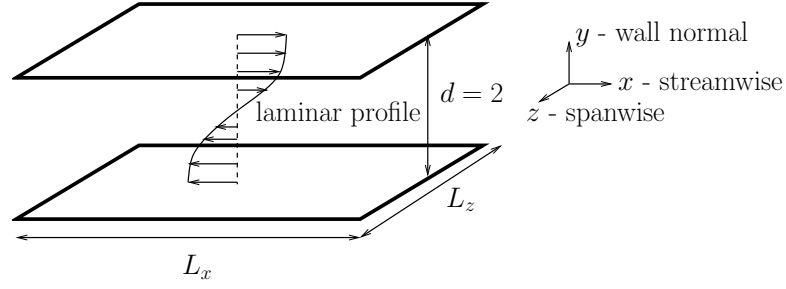


Figure 3.1: Geometry of sinusoidal shear flow where incompressible fluid between two free-slip walls is driven by a time-independent sinusoidal body force in the streamwise direction.

Couette flow, pipe flow, plane Poiseuille flow, and boundary layer flows.

Sinusoidal shear flow, whose geometry resembles that of plane Couette flow, obeys the the non-dimensional equations

$$\frac{\partial \mathbf{u}}{\partial t} = -(\mathbf{u} \cdot \nabla) \mathbf{u} - \nabla p + \frac{1}{Re} \nabla^2 \mathbf{u} + \mathbf{F}(y), \quad (3.1)$$

$$\nabla \cdot \mathbf{u} = 0, \quad (3.2)$$

where Re is the Reynolds number, defined as

$$Re = U_0 d / 2\nu, \quad (3.3)$$

where U_0 is the characteristic velocity obtained from the laminar velocity which arises from the sinusoidal body force given by

$$\mathbf{F}(y) = \frac{\sqrt{2}\pi^2}{4Re} \sin\left(\frac{\pi y}{2}\right) \hat{\mathbf{e}}_x. \quad (3.4)$$

This time independent body force results in the following laminar profile

$$\mathbf{U}(y) = (\sqrt{2} \sin(\pi y / 2), 0, 0), \quad (3.5)$$

which is linearly stable for all Re [12]. The free-slip boundary conditions are given by

$$u_y = 0, \quad \frac{\partial u_x}{\partial y} = \frac{\partial u_z}{\partial y} = 0, \quad (3.6)$$

which are imposed at $y = \pm 1$, and the flow is assumed periodic in the stream-wise (x) and spanwise (z) directions, with lengths L_x and L_z , respectively; see Figure 3.1.

3.1.1 Prominent Modes

In the following, the laminar-turbulent boundary of a nine-dimensional model for sinusoidal shear flow of [33] (see also [34]) will be studied and characterized. The low-dimensional model was derived via Galerkin projection of (3.1) onto important flow structures as follows. The velocity is expanded as

$$\mathbf{u}(\mathbf{x}, t) = \sum_{j=1}^9 a_j(t) \mathbf{u}_j(\mathbf{x}), \quad (3.7)$$

where the amplitudes a_j are real, and the modes \mathbf{u}_j are orthogonal under the standard inner product. This model generalizes the eight-mode model of [63], which includes modes describing the basic mean velocity profile, streamwise vortices, streaks, and instabilities of streaks. The main improvement for the nine-mode model is the inclusion of a mode which represents the lowest order modification of the laminar profile (3.5) and as a result of this adjustment, the other modes from the eight-mode model are modified slightly so that they can couple to this

new mode. The modes for this nine-dimensional model are the basic profile

$$\mathbf{u}_1 = \begin{pmatrix} \sqrt{2} \sin(\pi y/2) \\ 0 \\ 0 \end{pmatrix}, \quad (3.8)$$

representing a streamwise flow with the shape of the laminar profile. The streaks are given by:

$$\mathbf{u}_2 = \begin{pmatrix} \frac{4}{\sqrt{3}} \cos^2(\pi y/2) \cos(\gamma z) \\ 0 \\ 0 \end{pmatrix}, \quad (3.9)$$

that is, spanwise variations in the streamwise velocity, and

$$\mathbf{u}_3 = \frac{2}{\sqrt{4\gamma^2 + \pi^2}} \begin{pmatrix} 0 \\ 2\gamma \cos(\pi y/2) \cos(\gamma z) \\ \pi \sin(\pi y/2) \sin(\gamma z) \end{pmatrix}, \quad (3.10)$$

represents a pair of streamwise vortices. The spanwise flow is represented by the following two modes

$$\mathbf{u}_4 = \begin{pmatrix} 0 \\ 0 \\ \frac{4}{\sqrt{3}} \cos(\alpha x) \cos^2(\pi y/2) \end{pmatrix}, \quad (3.11)$$

$$\mathbf{u}_5 = \begin{pmatrix} 0 \\ 0 \\ 2 \sin(\alpha x) \sin(\pi y/2) \end{pmatrix}. \quad (3.12)$$

There are also two normal vortex modes

$$\mathbf{u}_6 = \frac{4\sqrt{2}}{\sqrt{3(\alpha^2 + \gamma^2)}} \begin{pmatrix} -\gamma \cos(\alpha x) \cos^2(\pi y/2) \sin(\gamma z) \\ 0 \\ \alpha \sin(\alpha x) \cos^2(\pi y/2) \cos(\gamma z) \end{pmatrix}, \quad (3.13)$$

$$\mathbf{u}_7 = \frac{2\sqrt{2}}{\sqrt{\alpha^2 + \gamma^2}} \begin{pmatrix} \gamma \sin(\alpha x) \sin(\pi y/2) \sin(\gamma z) \\ 0 \\ \alpha \cos(\alpha x) \sin(\pi y/2) \cos(\gamma z) \end{pmatrix}, \quad (3.14)$$

and a fully-three dimensional mode

$$\mathbf{u}_8 = \frac{2\sqrt{2}}{\sqrt{(\alpha^2 + \gamma^2)(4\alpha^2 + 4\gamma^2 + \pi^2)}} \begin{pmatrix} \pi\alpha \sin(\alpha x) \sin(\pi y/2) \sin(\gamma z) \\ 2(\alpha^2 + \gamma^2) \cos(\alpha x) \cos(\pi y/2) \sin(\gamma z) \\ -\pi\gamma \cos(\alpha x) \sin(\pi y/2) \cos(\gamma z) \end{pmatrix}. \quad (3.15)$$

The modification to the laminar mean flow profile is represented by

$$\mathbf{u}_9 = \begin{pmatrix} \sqrt{2} \sin(3\pi y/2) \\ 0 \\ 0 \end{pmatrix}. \quad (3.16)$$

3.1.2 Amplitude Equations

The interactions between these nine modes sufficiently sustain the dynamics needed to maintain the fluctuations in a non-periodic fashion as expected for a turbulent shear flow [33]. Inserting (3.7) into (3.1) and projecting, a set of nine

coupled, nonlinear ordinary differential equations is obtained given by

$$\frac{da_1}{dt} = \frac{\beta^2}{Re} - \frac{\beta^2}{Re}a_1 - \sqrt{\frac{3}{2}} \frac{\beta\gamma}{\kappa_{\alpha\beta\gamma}} a_6 a_8 + \sqrt{\frac{3}{2}} \frac{\beta\gamma}{\kappa_{\beta\gamma}} a_2 a_3, \quad (3.17)$$

$$\begin{aligned} \frac{da_2}{dt} = & - \left(\frac{4\beta^2}{3} + \gamma^2 \right) \frac{a_2}{Re} + \frac{5\sqrt{2}}{3\sqrt{3}} \frac{\gamma^2}{\kappa_{\alpha\gamma}} a_4 a_6 - \frac{\gamma^2}{\sqrt{6}\kappa_{\alpha\gamma}} a_5 a_7 \\ & - \frac{\alpha\beta\gamma}{\sqrt{6}\kappa_{\alpha\gamma}\kappa_{\alpha\beta\gamma}} a_5 a_8 - \sqrt{\frac{3}{2}} \frac{\beta\gamma}{\kappa_{\beta\gamma}} (a_1 a_3 + a_3 a_9), \end{aligned} \quad (3.18)$$

$$\begin{aligned} \frac{da_3}{dt} = & - \frac{\beta^2 + \gamma^2}{Re} a_3 + \frac{2}{\sqrt{6}} \frac{\alpha\beta\gamma}{\kappa_{\alpha\gamma}\kappa_{\beta\gamma}} (a_4 a_7 + a_5 a_6) \\ & + \frac{\beta^2(3\alpha^2 + \gamma^2) - 3\gamma^2(\alpha^2 + \gamma^2)}{\sqrt{6}\kappa_{\alpha\gamma}\kappa_{\beta\gamma}\kappa_{\alpha\beta\gamma}} a_4 a_8, \end{aligned} \quad (3.19)$$

$$\begin{aligned} \frac{da_4}{dt} = & - \frac{3\alpha^2 + 4\beta^2}{3Re} a_4 - \frac{\alpha}{\sqrt{6}} (a_1 a_5 + a_5 a_9) - \frac{10}{3\sqrt{6}} \frac{\alpha^2}{\kappa_{\alpha\gamma}} a_2 a_6 \\ & - \sqrt{\frac{3}{2}} \frac{\alpha\beta\gamma}{\kappa_{\alpha\gamma}\kappa_{\beta\gamma}} a_3 a_7 - \sqrt{\frac{3}{2}} \frac{\alpha^2\beta^2}{\kappa_{\alpha\gamma}\kappa_{\beta\gamma}\kappa_{\alpha\beta\gamma}} a_3 a_8, \end{aligned} \quad (3.20)$$

$$\begin{aligned} \frac{da_5}{dt} = & - \frac{\alpha^2 + \beta^2}{Re} a_5 + \frac{\alpha}{\sqrt{6}} (a_1 a_4 + a_4 a_9) + \frac{\alpha^2}{\sqrt{6}\kappa_{\alpha\gamma}} a_2 a_7 \\ & - \frac{\alpha\beta\gamma}{\sqrt{6}\kappa_{\alpha\gamma}\kappa_{\alpha\beta\gamma}} a_2 a_8 + \frac{2}{\sqrt{6}} \frac{\alpha\beta\gamma}{\kappa_{\alpha\gamma}\kappa_{\beta\gamma}} a_3 a_6, \end{aligned} \quad (3.21)$$

$$\begin{aligned} \frac{da_6}{dt} = & - \frac{3\alpha^2 + 4\beta^2 + 3\gamma^2}{3Re} a_6 + \frac{\alpha}{\sqrt{6}} (a_1 a_7 + a_7 a_9) + \frac{10}{3\sqrt{6}} \frac{\alpha^2 - \gamma^2}{\kappa_{\alpha\gamma}} a_2 a_4 \\ & - 2\sqrt{\frac{2}{3}} \frac{\alpha\beta\gamma}{\kappa_{\alpha\gamma}\kappa_{\beta\gamma}} a_3 a_5 + \sqrt{\frac{2}{3}} \frac{\beta\gamma}{\kappa_{\alpha\beta\gamma}} (a_1 a_8 + a_8 a_9), \end{aligned} \quad (3.22)$$

$$\begin{aligned} \frac{da_7}{dt} = & - \frac{\alpha^2 + \beta^2 + \gamma^2}{Re} a_7 - \frac{\alpha}{\sqrt{6}} (a_1 a_6 + a_6 a_9) + \frac{1}{\sqrt{6}} \frac{\gamma^2 - \alpha^2}{\kappa_{\alpha\gamma}} a_2 a_5 \\ & + \frac{1}{\sqrt{6}} \frac{\alpha\beta\gamma}{\kappa_{\alpha\gamma}\kappa_{\beta\gamma}} a_3 a_4, \end{aligned} \quad (3.23)$$

$$\begin{aligned} \frac{da_8}{dt} = & -\frac{\alpha^2 + \beta^2 + \gamma^2}{Re} a_8 + \frac{\gamma^2(3\alpha^2 - \beta^2 + 3\gamma^2)}{\sqrt{6}\kappa_{\alpha\gamma}\kappa_{\beta\gamma}\kappa_{\alpha\beta\gamma}} a_3 a_4 \\ & + \frac{2}{\sqrt{6}} \frac{\alpha\beta\gamma}{\kappa_{\alpha\gamma}\kappa_{\alpha\beta\gamma}} a_2 a_5, \end{aligned} \quad (3.24)$$

$$\frac{da_9}{dt} = -\frac{9\beta^2}{Re} a_9 - \sqrt{\frac{3}{2}} \frac{\beta\gamma}{\kappa_{\alpha\beta\gamma}} a_6 a_8 + \sqrt{\frac{3}{2}} \frac{\beta\gamma}{\kappa_{\beta\gamma}} a_2 a_3, \quad (3.25)$$

where

$$\kappa_{\alpha\gamma} = \sqrt{\alpha^2 + \gamma^2}, \quad \kappa_{\beta\gamma} = \sqrt{\beta^2 + \gamma^2}, \quad \kappa_{\alpha\beta\gamma} = \sqrt{\alpha^2 + \beta^2 + \gamma^2}. \quad (3.26)$$

In the following, we define the spatial wavenumbers as:

$$\alpha = \frac{2\pi}{L_x}, \quad \beta = \frac{\pi}{2}, \quad \gamma = \frac{2\pi}{L_z}. \quad (3.27)$$

3.1.3 Dynamics of the Model

The transition to turbulence for this nine-mode model is subcritical which means that it is possible to get turbulent-like behavior at values of Reynolds numbers for which the laminar state is stable. Furthermore, the distributions of turbulent lifetimes, which indicates the duration of turbulence before decay to the laminar state, are exponential, in agreement with observations in many shear flows [33]. For this system, the energy in the system is taken to be the fluctuation energy with respect to the laminar profile, and is defined as

$$E \equiv (1 - a_1)^2 + \sum_{i=2}^9 a_i^2. \quad (3.28)$$

The modes (3.8–3.16) have been normalized so that the energy contained in a given mode is simply the amplitude of the mode squared. As found in [34], the symmetry properties of the system are such that $\mathbf{a} = (a_1, a_2, a_3, a_4, a_5, a_6, a_7, a_8, a_9)$ is equivariant under translation symmetries which make up the group

$$\{Id, \mathcal{T}_{L_x/2}, \mathcal{T}_{L_z/2}, \mathcal{T}_{L_x/2, L_z/2}\}, \quad (3.29)$$

where

$$\mathcal{T}_{L_x/2} \cdot \mathbf{a} = (a_1, a_2, a_3, -a_4, -a_5, -a_6, -a_7, -a_8, a_9), \quad (3.30)$$

$$\mathcal{T}_{L_z/2} \cdot \mathbf{a} = (a_1, -a_2, -a_3, a_4, a_5, -a_6, -a_7, -a_8, a_9). \quad (3.31)$$

These group elements respectively correspond to the identity element, translation by $L_x/2$ in the streamwise direction, translation by $L_z/2$ in the spanwise direction, and the composition of both such translations.

As mentioned before, the geometry of sinusoidal shear flow is very similar to that of plane Couette flow, the only difference being that the fluid in sinusoidal shear flow is driven by a sinusoidal body force and has free-slip boundary conditions. This greatly simplifies the derivation of the model with respect to plane Couette flow by allowing the modes $\mathbf{u}_1, \dots, \mathbf{u}_9$ to be written in terms of trigonometric functions. Nevertheless, this nine-dimensional model exhibits turbulent-like dynamics observed in other shear flows. Therefore to validate the model, a turbulent statistics analysis of the system is performed.

Figure 3.2 compares statistics of fluctuations from the laminar state for the stable periodic orbit of the nine-dimensional model with turbulent direct numerical simulation data for plane Couette flow from [53], both at $Re = 400$ with channel lengths $L_x = 1.75\pi$ and $L_z = 1.2\pi$. Note that for the related system of plane Couette flow, these parameters correspond to the minimal flow unit, the smallest domain which is found numerically to sustain turbulence [23]. In general, the trend is the same in terms of the location of the peaks for the wall-normal root mean square fluctuations $\sqrt{\langle v'^2 \rangle}$ and the Reynolds stress $\langle u'v' \rangle$. However, for the nine-dimensional model, the stress term is smaller by an order of magnitude. On the other hand, note that the streamwise and spanwise root mean square fluctuations differ more substantially for the two flows. These results are not surprising since the two flows have distinct boundary conditions: no-slip and free-slip for plane Couette flow and sinusoidal shear flow, respectively. Nevertheless, the agreement in these quantities, and the work by [33] supports the idea that this nine-mode model is a good representation and captures essential behaviors of typical shear flows. Therefore, it is hoped that the knowledge gained from studying the edge of chaos for sinusoidal shear flow will be relevant to the laminar-turbulent boundary dynamics for other shear flows.

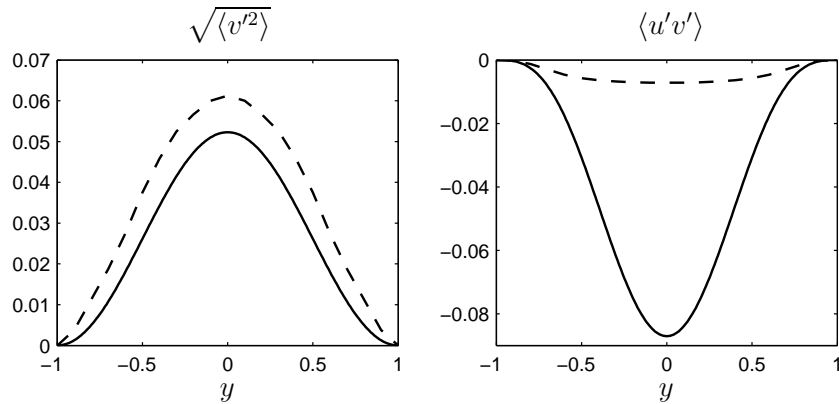


Figure 3.2: Comparisons of the turbulent statistics for the nine-dimensional model for sinusoidal shear flow (solid) and plane Couette flow taken from direct numerical simulation data from [53].

3.2 Finding the Edge of Chaos

The edge of chaos is the boundary which separates transiently chaotic from non-chaotic behavior and contains a set of solutions which neither decay nor become chaotic. For this low-dimensional model, the edge of chaos is found using a systematic bisection method which is similar to the method used for a different shear flow model in [51]; see Figure 3.3. The edge tracking algorithm starts out with a randomly chosen initial condition. The initial condition is then systematically updated along a one-dimensional curve in phase space, near the laminar state fixed point. This means that all the initial values of the amplitude are kept constant except for one, which is used as a parameter in the bisection method. The algorithm has been written so that it looks for two things: if the trajectory directly decays to the laminar state, then the algorithm takes an initial

condition on the curve further away from the laminar state, and conversely, if the trajectory shows transient chaos, it takes an initial condition on the curve closer to the laminar state. The points further/closer to the laminar state fixed point, contained to a one-dimensional curve, are typically found by varying one of the amplitudes a_j ¹. By refining the initial conditions via a bisection rule, the algorithm finds trajectories that neither decay nor show transient chaos. The goal is to find objects which lie on the boundary of these behaviors. It is important to note that one of the benefits of this algorithm is that it does not have to start with a particular type of initial condition, that is, the algorithm can find the edge of chaos when starting with an initial condition which either decays directly to the laminar state or shows chaotic behavior. Moreover, a simple bisection method for finding the laminar-turbulent boundary suffices because there is a clear distinction between chaotic and non-chaotic trajectories, therefore, it is not necessary to use a more sophisticated algorithm to find the edge in this system.

3.3 The Edge of Chaos for Sinusoidal Shear Flow

For this system, the laminar state is stable for all Reynolds numbers and corresponds to the asymptotically stable fixed point at $a_1 = 1, a_2 = \dots = a_9 = 0$.

¹The choice of amplitude is not important in this algorithm since the edge of chaos can be found by bisecting in any direction. In particular, the chaotic and non-chaotic behavior of the system is clearly distinguishable in all the modes of the model.

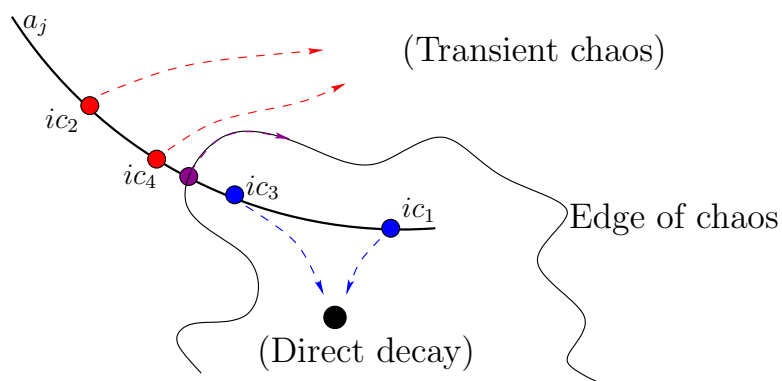


Figure 3.3: Schematic diagram of the edge tracking algorithm for sinusoidal shear flow showing a boundary in phase space separating initial conditions which exhibit direct decay and transiently chaotic behavior. Initial conditions ic_n are systematically updated along a one-dimensional curve a_j to find trajectories near the edge of chaos. Initial conditions on one side of the edge will (red) become transiently chaotic while initial conditions on the other side (blue) will decay directly to the laminar state. The edge-tracking algorithm will find trajectories (purple) which neither decay nor grow and follow the edge.

In particular, for $Re \lesssim 335$ and $515 \lesssim Re < 1000$, this fixed point is the global attractor for this model which implies that all trajectories will eventually end up at the laminar state fixed point. Initial conditions for this range of Re exhibit two distinct behaviors: (1) direct laminarization or (2) a chaotic transient before decaying to the laminar state. This behavior coincides with the situation for the low-dimensional model considered in [51]. Figure 3.4 shows the evolution of amplitude a_4 , corresponding to a spanwise flow mode, as a function of time at $Re = 300$ for two initial conditions near the laminar state, which in this figure corresponds to $a_4 = 0$. The top panel corresponds to a trajectory which visits an unstable periodic orbit before decaying to the laminar state, and the bottom panel corresponds to a trajectory which comes near the same periodic orbit and

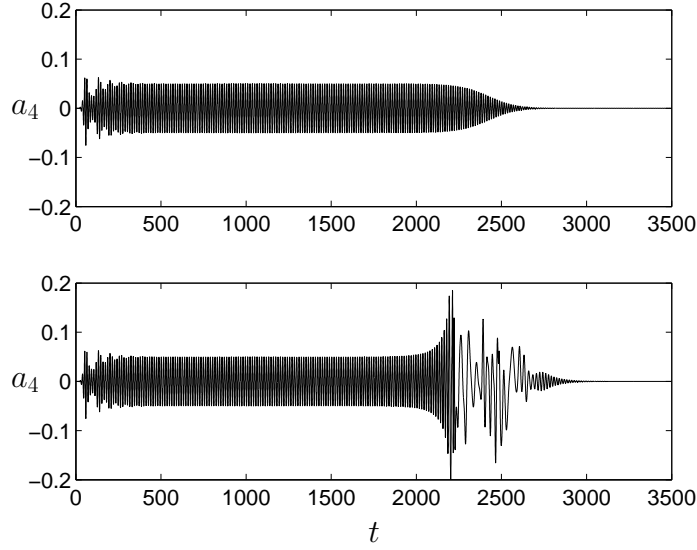


Figure 3.4: Transient and decay dynamics exhibited by the nine-dimensional model for $Re \lesssim 335$ and $515 \lesssim Re \leq 1000$. The time evolution for the amplitude of the fourth mode a_4 showing qualitatively different behaviors for two nearby initial conditions at $Re = 300$. The initial conditions for the two trajectories were kept constant with the exception of $a_4(0)$, which only differ from each other by a quantity of order 10^{-15} .

undergoes transient chaotic dynamics before laminarization. For this example, the stable manifold of the unstable periodic orbit separates initial conditions which directly laminarize from those which are transiently chaotic, therefore, this orbit determines the edge of chaos.

3.3.1 The Chaotic Transient State

The transient chaotic state in this system is associated with a chaotic saddle near which trajectories stay for a finite time before escaping. The duration of the chaotic transient is very sensitive to initial conditions and Reynolds numbers,

indeed, a one-dimensional perturbation of order 10^{-15} can give vastly different transient times. As indicated in §2.2, this behavior is indicative of the fractal nature of the lifetimes [33, 32, 51], but the overall trend is that the duration of the transient increases with Re . A schematic diagram of the dynamics around the edge of chaos for this nine-dimensional model is shown in Figure 3.5. The unstable periodic orbit associated with the edge of chaos coexists with the asymptotically stable laminar state fixed point and the chaotic saddle in phase space. This periodic orbit has a codimension-1 stable manifold and acts as the surface which separates the chaotic and directly decaying dynamics in phase space. The unstable manifold of the unstable periodic orbit either directs trajectories, like those labelled a in the figure, to the laminar state or shoots them up, like in the case of b , so that it visits near the chaotic saddle before decaying to the laminar state.

3.3.2 Characteristics of the Unstable Periodic Orbit Associated with the Edge of Chaos

The unstable periodic orbit associated with the edge of chaos, which is visited by the type of trajectories described above for this system, is shown in Figures 3.6 and 3.7. Using AUTO [11], it was numerically verified that this periodic orbit has only one unstable direction. Its eight-dimensional stable manifold separates

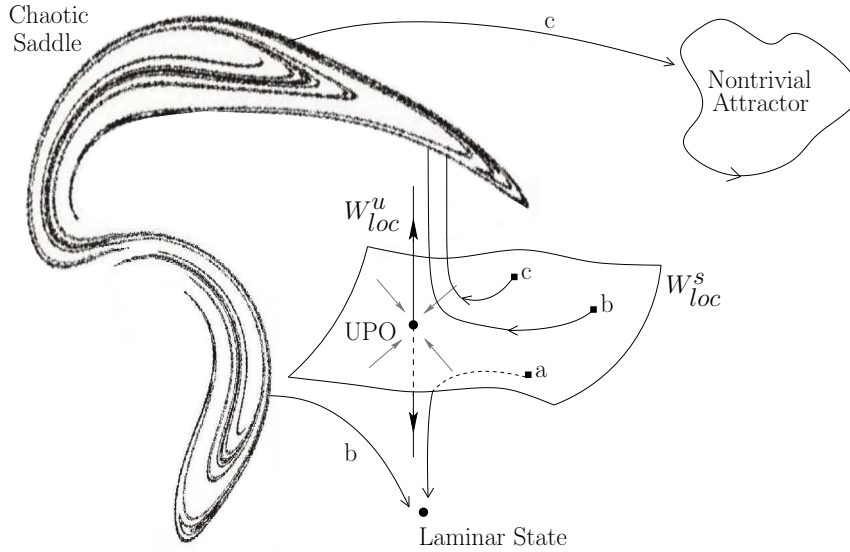


Figure 3.5: A schematic diagram of the dynamics of the nine-dimensional model in the neighborhood of the edge of chaos. The unstable periodic orbit (UPO) has an unstable manifold W_{loc}^u and an eight-dimensional stable manifold W_{loc}^s and forms the edge of chaos. For $Re \lesssim 335$ and $515 \lesssim Re < 1000$, the only attractor in the system is the laminar state fixed point and initial conditions either (a) decay directly to the laminar state (see top panel of Figure 3.4) or (b) become transiently chaotic before decaying to the laminar state (see bottom panel of Figure 3.4). For $335 \lesssim Re \lesssim 515$, initial conditions may tend towards a nontrivial attractor as in (c) and the third panel of Figure 3.10.

initial conditions that exhibit transiently chaotic behavior from those which directly decay to the laminar state, and forms the edge of chaos. This unstable orbit remains as the periodic orbit associated with the edge of chaos, as was confirmed by finding the edge for different values of the Reynolds number using the bisection method described in §3.2. Furthermore, it was verified that the edge tracking algorithm used for this model consistently converges to the same periodic orbit regardless of the initial condition used to begin the bisection algorithm and the direction that is chosen for the one-dimensional curve which intersects

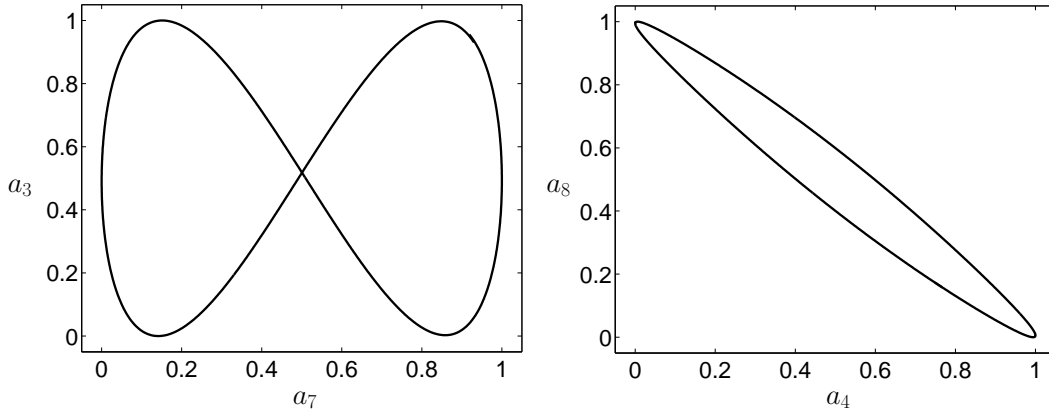


Figure 3.6: The unstable periodic orbit associated with the edge of chaos for $Re = 400$ with period $T = 13.60$ in two different projections.

its manifold. Note that for $Re \lesssim 250$, the only periodic orbits with smaller mean perturbation energy arise in a bifurcation from this periodic orbit branch. For $Re \gtrsim 250$, this periodic orbit has the smallest mean perturbation energy of all the periodic orbits found for this system [33, 34].

An important observation from Figure 3.7 is the difference between the group of modes representing the instability in the streaks and the three-dimensional flow $S_A : \{a_4, a_5, a_6, a_7, a_8\}$ from the group of modes corresponding to the basic profile, streamwise vortices and streaks $S_B : \{a_1, a_2, a_3, a_9\}$. In particular, the peak-to-peak amplitudes for the modes in group S_A are approximately 50 – 2500 times larger than the peak-to-peak amplitudes of the modes in group S_B . However, the streak mode, corresponding to a_2 , has a peak-to-peak amplitude which is comparable to those of the modes in S_A . Moreover, the period of the modes in

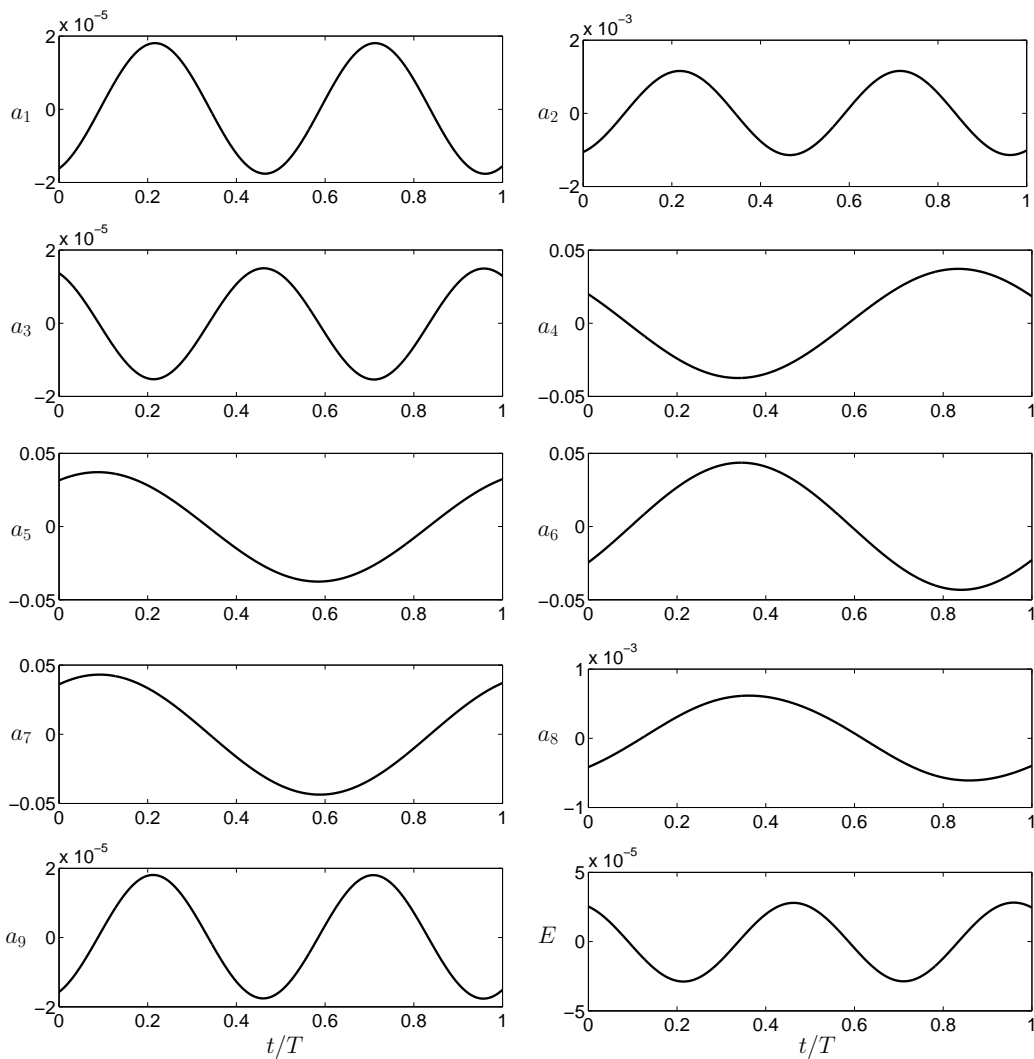


Figure 3.7: Time series for the amplitudes of the unstable periodic orbit in Figure 3.6 over one period.

group S_B are twice that of the modes in group S_A . This result implies that the dynamics of the unstable periodic orbit associated with the edge of chaos are dominated by the streak and streak instability modes.

A scaling analysis was conducted using AUTO [11] for various components of the unstable periodic orbit associated with the edge of chaos. This was achieved by calculating the average values of the energy, streak, and streamwise vortex amplitudes; see Figure 3.8. The average energy, streak and streamwise vortex modes scale as $Re^{-2}, Re^{-1}, Re^{-2}$, respectively. These scalings are different from comparable results found in [66] which finds that for the lower branch state for plane Couette flow, the amplitudes of the streaks and streamwise vortices scale as Re^0, Re^{-1} , respectively. The difference in the scaling may be due to the fact that the boundary conditions for plane Couette flow and sinusoidal shear flow are different. However, the ratio between the scalings of the vortices and streaks is the same, i.e. $\frac{\langle a_3 \rangle}{\langle a_2 \rangle} \sim Re^{-1}$ for these flows. This indicates that for both plane Couette flow and the nine-dimensional model for sinusoidal shear flow, the streamwise vortices become relatively weaker with increasing Re .

As mentioned in §3.1.3 and noted in [34], the low-dimensional model for sinusoidal shear flow is equivariant [19, 35] with respect to the group $D_2 \equiv \{Id, \mathcal{T}_{L_x/2}, \mathcal{T}_{L_z/2}, \mathcal{T}_{L_x/2, L_z/2}\}$. The action of $\mathcal{T}_{L_x/2}$ on the unstable periodic orbit associated with the edge of chaos gives a time shift of half of a period; thus, this

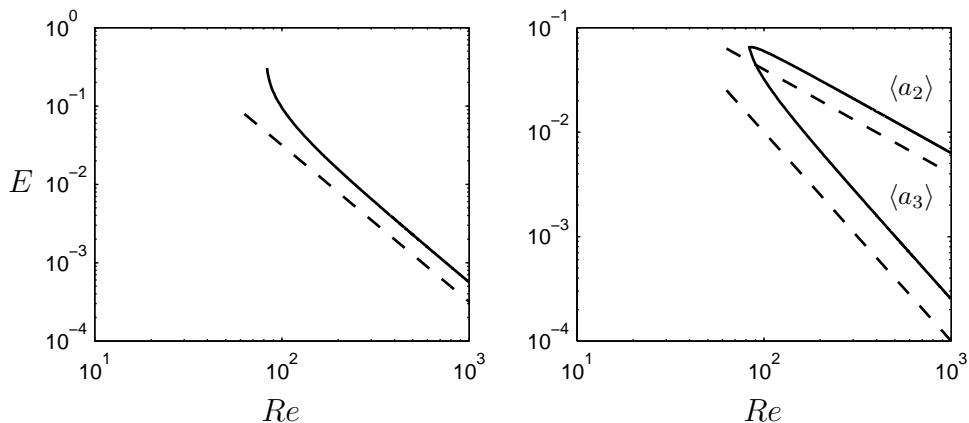


Figure 3.8: The average values of the energy, streaks a_2 , and streamwise vortices a_3 of the unstable periodic orbit associated with the edge of chaos as a function of Re . (left) The average energy of the unstable periodic orbit (solid) scales as Re^{-2} (dashed). (right) A scaling analysis shows that $\langle a_2 \rangle$ (upper solid curve) scales as Re^{-1} (upper dashed line) while $\langle a_3 \rangle$ (lower solid curve) scales as Re^{-2} (lower dashed line)

periodic orbit is (setwise) invariant under $\mathcal{T}_{L_x/2}$. The action of $\mathcal{T}_{L_z/2}$ on this periodic orbit gives a distinct, symmetry-related unstable periodic orbit, which is also (setwise) invariant under $\mathcal{T}_{L_x/2}$. The periodic orbit obtained by the action of $\mathcal{T}_{L_x/2, L_z/2}$ on the original unstable periodic orbit is related to the latter one by a time shift of half a period. Thus, there are two symmetry-related unstable periodic solutions, each with its own eight-dimensional stable manifold which forms an edge of chaos. By uniqueness of solutions backwards in time, these stable manifolds cannot intersect.

3.4 Probabilistic Analysis of the Edge of Chaos

The current study involves a nine-dimensional model with an eight-dimensional edge of chaos. Thus, a complete characterization of the laminar-turbulent boundary is not possible. A more practical way to study and describe the edge is by considering a probabilistic approach. The objective is to calculate the probability that an initial condition with a given energy will lead to chaotic behavior. In particular, sets of roughly 2000 uniformly distributed initial conditions with the same energy are drawn from the surface of a nine-dimensional hypersphere. The radius of the hypersphere corresponds to the square-root of the initial energy in the system, which ranges from $E(0) = 5 \times 10^{-5}$ to 5×10^{-3} .

To generate a set of uniformly distributed random samples on a n -dimensional sphere, let

$$\begin{aligned}x_1 &= r \cos(\phi_1), \\x_2 &= r \sin(\phi_1) \cos(\phi_2), \\&\vdots \\x_{n-1} &= r \sin(\phi_1) \cdots \sin(\phi_{n-2}) \cos(\phi_{n-1}), \\x_n &= r \sin(\phi_1) \cdots \sin(\phi_{n-2}) \sin(\phi_{n-1}),\end{aligned}\tag{3.32}$$

where $\phi_1, \dots, \phi_{n-2}$ take the values between 0 and π , ϕ_{n-1} takes values between 0

and 2π , and r is the radius of the sphere whose equation is

$$x_1^2 + \cdots + x_{n-1}^2 + x_n^2 = r^2. \quad (3.33)$$

Let $P(\phi_1, \cdots, \phi_{n-1})$ be a probability distribution function defined on the surface Ω of the sphere. For a uniform distribution, this is a constant determined by the normalization condition

$$\int_{\Omega} P(\phi_1, \cdots, \phi_{n-1}) d\Omega = 1, \quad (3.34)$$

where

$$d\Omega = \prod_{j=1}^{n-1} \sin^{n-j-1}(\phi_j) d\phi_j \quad (3.35)$$

is the element of area. Then, P is split into the product of distributions P_j so that

$$P(\phi_1, \cdots, \phi_{n-1}) d\Omega = P_1(\phi_1) d\phi_1 \cdots P_{n-1}(\phi_{n-1}) d\phi_{n-1} \quad (3.36)$$

giving

$$P_j(\phi_j) = c_j \sin^{n-j-1}(\phi_j), \quad j = 1, \cdots, n-1. \quad (3.37)$$

The constants c_j are determined from the normalization conditions

$$\int_0^{\pi} P_j(\phi_j) d\phi_j = 1 \quad j = 1, \cdots, n-2, \quad (3.38)$$

$$\int_0^{2\pi} P_{n-1}(\phi_{n-1}) d\phi_{n-1} = 1, \quad (3.39)$$

which guarantees that (3.34) will be satisfied. In order to obtain a sample of such a probability distribution function, the fundamental transformation law of

probabilities is utilized to obtain

$$P_j(\phi_j) = \left| \frac{d\omega_j}{d\phi_j} \right|. \quad (3.40)$$

For a particular sample ω_j , this can be inverted numerically to give the corresponding value of ϕ_j which may be used to construct the initial conditions x_j ; see Appendix A for more details.

Integrating these initial conditions for a sufficiently long time will determine whether or not they lead to a solution which exhibits chaotic behavior. Note that as Re increases, the time it takes for trajectories to reach the chaotic saddle (associated with transient chaos) also increases, so the integration time is increased as appropriate. For this analysis, the amplitude of the basic mode a_1 is tracked as the indicator of chaotic behavior in the system. The laminar state corresponds to $a_1 = 1$ whose value is significantly different from the value of the amplitude in the chaotic saddle, ($a_1 \lesssim 0.5$). Thus, determining whether a trajectory becomes chaotic is manageable by monitoring whether a_1 crosses the threshold $a_1 = 0.5$.

Figure 3.9 shows that the probability of transient chaos increases with Reynolds number and perturbation amplitude. These probability curves agree well with the average value of the energy of the unstable periodic orbit associated with the edge of chaos. In particular, Figure 3.9 shows the average energy drawn as a thick black curve, superimposed on the contour plot. The fact that the energy is in the 96 – 97% range demonstrates the high level of agreement between probabilistic

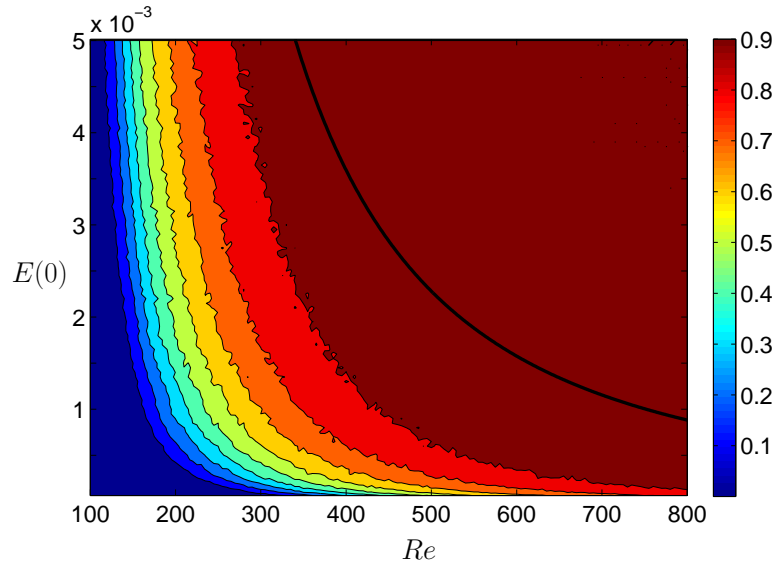


Figure 3.9: The probability of transient chaos as a function of Re and initial perturbation energy. The contour lines represent probability increments of 10% with the upper contour being the 90% curve. The thick black curve represents the average energy in the unstable periodic orbit associated with the edge of chaos.

and the Reynolds number scaling analysis performed for the unstable periodic orbit associated with the edge of chaos.

3.5 Basin Boundary of the Nontrivial Attractor

A stable nontrivial attractor coexists with the laminar state fixed point, unstable periodic orbit, and chaotic saddle in phase space for $335 \lesssim Re \lesssim 515$. The attractor captures signatures of the self-sustaining process elucidated in [61, 62, 63], as shown in [34]. For this reason, the nontrivial attractor is associated with the sustained turbulence in this study. Figure 3.10 shows the time series evolution of

the amplitude a_4 , corresponding to a spanwise flow mode, for an initial condition near the laminar state fixed point for $Re = 400$. Recall that the laminar state for this amplitude corresponds to $a_4 = 0$. In this figure, the system again visits near the same unstable periodic orbit found in Figure 3.4 but for a different value of the Reynolds number. The last panel shows the additional qualitative behavior the system undergoes, transient chaotic behavior before it enters the neighborhood of the nontrivial attractor. These dynamics correspond to the initial condition labelled c in Figure 3.5. Note that the initial conditions which give transient chaos before decaying to the laminar state are extremely close to those which tend towards the nontrivial attractor. It is necessary to emphasize that this observation is indicative of the sensitive nature of the initial conditions in the basin of attraction of the nontrivial attractor.

Table 3.1 shows that the attractor can be chaotic, periodic, or quasiperiodic, depending on the Reynolds number, and in all these cases the attractor explores similar regions of phase space as shown in Figures 3.11 and 3.12. At $Re \approx 515$, the nontrivial attractor undergoes a crisis [20], and for higher Reynolds numbers it ceases to exist. This is apparently due to the boundary of the basin of attraction of the attractor colliding with one of the many unstable periodic orbits for this model, cf. [34]. This implies that all trajectories beyond this critical Reynolds number will eventually decay to the laminar state; however, they can display

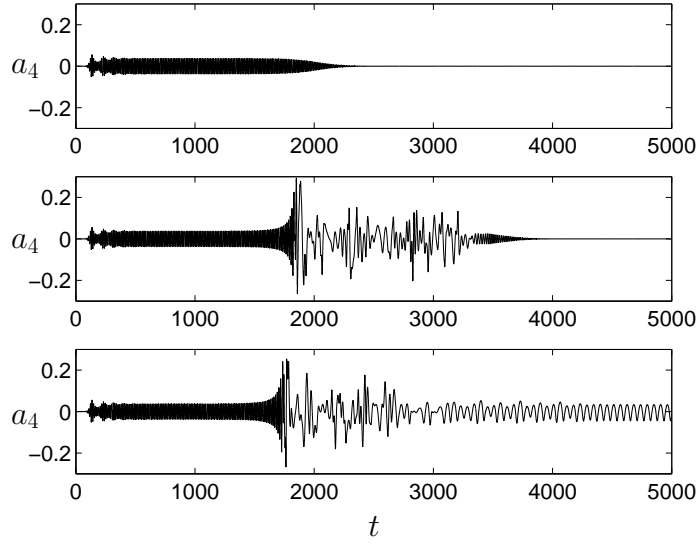


Figure 3.10: Time evolution of the amplitude a_4 for the nine-dimensional model for $335 \lesssim Re \lesssim 515$. In this range of Re , an additional qualitatively different behavior from Figure 3.4 is shown in the lower panel but for $Re = 400$. These behaviors, which are analogous to those shown in Figure 3.4, occur for initial conditions which differ in a_4 by a quantity of order 10^{-15} .

transient chaos before this decay. The situation for $515 \lesssim Re < 1000$ is thus similar that of $Re \lesssim 335$ and to the situation for a different low-dimensional model considered in [51].

Type of attractor	Reynolds number
Chaotic	$335 \lesssim Re \lesssim 355$
Periodic	$355 \lesssim Re \lesssim 508$
Quasiperiodic	$508 \lesssim Re \lesssim 515$
None	$Re < 335$ and $Re > 515$

Table 3.1: Classification of the nontrivial attractor as a function of Re .

Figure 3.13 shows the probability that perturbations of a given initial energy lead to the nontrivial attractor for $335 \leq Re \leq 515$. The first sharp contour

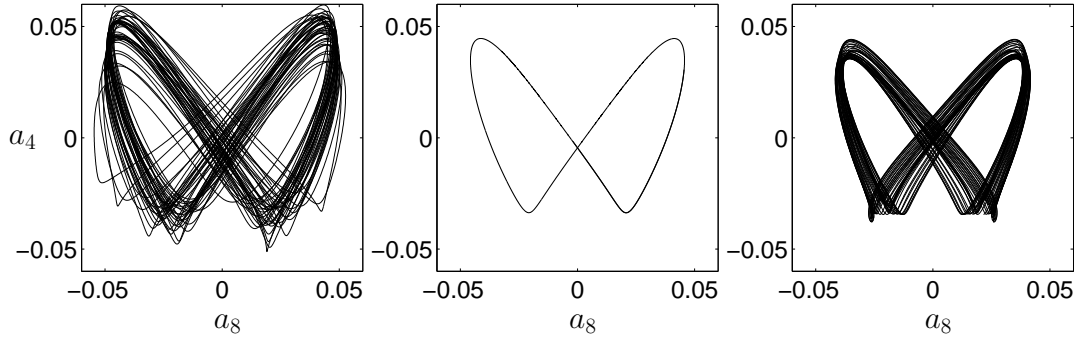


Figure 3.11: Examples of nontrivial attractors found for $335 \lesssim Re \lesssim 515$, including (left) chaotic behavior at $Re = 345$, (center) a stable periodic orbit at $Re = 400$, and (right) a quasi-periodic attractor at $Re = 510$.

line indicates a 10% probability of reaching the nontrivial attractor, and the last contour line corresponds to a 60% probability. Below $Re \approx 335$, there is no nontrivial attractor, and all trajectories approach the laminar state fixed point. A numerical scaling analysis shows that each of the contour lines in Figure 3.13 scale as

$$E(0) = c(Re - Re_c)^\sigma, \quad (3.41)$$

where c is a constant whose value for this fit is always 5×10^{-3} . This fit has two important parameters: Re_c which is the Reynolds number to which the probability contours asymptotically tend, and σ which is the scaling factor for each curve. The values of the critical Reynolds number and scaling factor for the corresponding probability curves is given in Table 3.2. The values of the scaling factor σ are comparable to the turbulent threshold exponent for other shear flows, such as plane Couette flow and plane Poiseuille flow; see e.g. [57, 6].

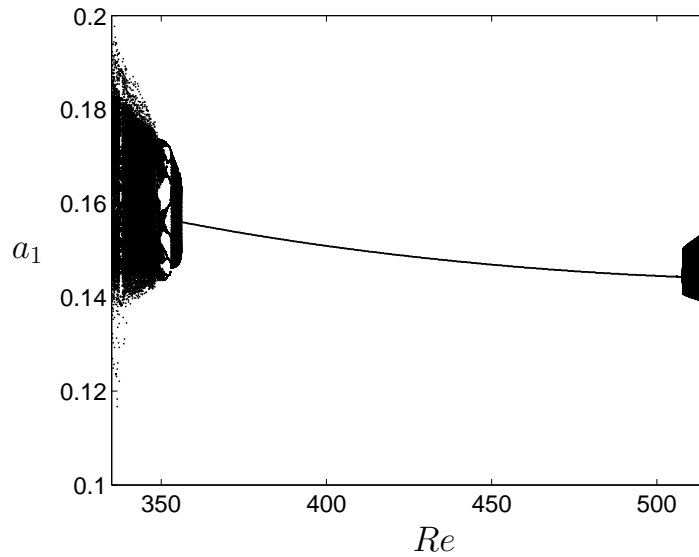


Figure 3.12: Bifurcation diagram showing the instantaneous value of a_1 whenever the trajectory pierces the Poincaré section defined by $a_2 = 0$ with $\dot{a}_2 < 0$. This plot is generated by adiabatically changing the value of Re , omitting transients. For $335 \lesssim Re \lesssim 355$, the attractor is chaotic, for $355 \lesssim Re \lesssim 508$ the attractor is a stable periodic orbit, and for $508 \lesssim Re \lesssim 515$ the attractor is quasiperiodic. For more detail for $335 \leq Re \leq 360$, see Figure 21 of [34].

The relationship between the edge of chaos and the basin boundary is shown in Figure 3.14, at $Re = 400$. This figure shows that the stable manifold of the unstable periodic orbit associated with the edge of chaos smoothly and sharply separates (gray) direct decay to the laminar state from (red and blue) transient chaotic behavior. This is in contrast to the basin structure between initial conditions which lead to the laminar state fixed point or the nontrivial attractor, as seen in the red and blue speckled region of the figure. The basin boundary between these two behaviors, as shown in Figure 3.14, is not smooth like the edge of chaos, but rather fractal in nature. The fact that trajectories can come back

Probability curve	Critical Reynolds number (Re_c)	Scaling factor (σ)
10	349	-1.6
20	357	-1.3
30	362	-0.85
40	380	-0.73
50	405	-0.65
60	450	-0.55

Table 3.2: Reynolds number scalings for probability of transient chaos curves.

to the laminar state after a chaotic transient is surprising. A possible explanation is that the stable manifold of the unstable periodic orbit could be a closed, non-orientable surface with neither an inside or an outside.

3.6 Discussion

The edge of chaos for a nine-dimensional model for sinusoidal shear flow was characterized as the eight-dimensional stable manifold of an unstable periodic orbit. Its one unstable direction is associated with the separation into regions in phase space where trajectories either decay to the laminar state or exhibit chaotic behavior. Since a complete classification of the laminar-turbulent boundary was not feasible, due to its high dimensionality, a probabilistic analysis of the edge of chaos was conducted. The analysis revealed how the probability of transient chaos increases with Reynolds number and perturbation amplitude. Furthermore, the scaling analysis for average energy content in the unstable periodic orbit showed

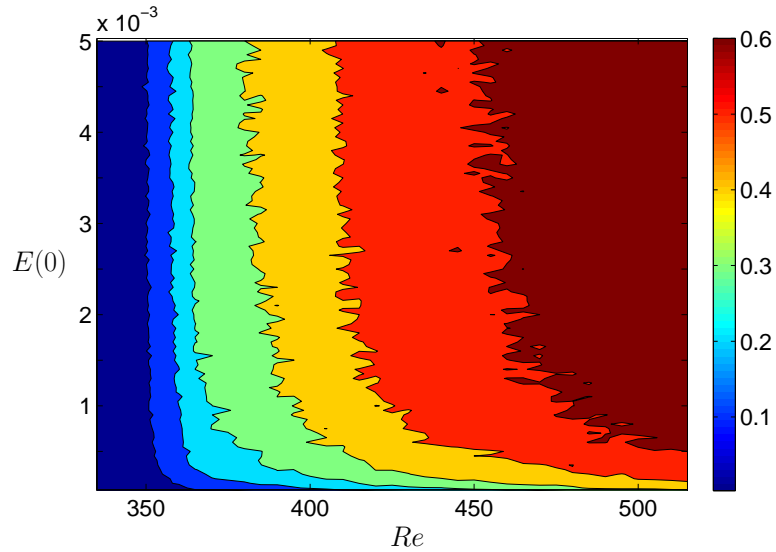


Figure 3.13: The probability of reaching the nontrivial attractor associated with sustained turbulence as a function of Re and initial perturbation energy.

good agreement with the probabilistic analysis performed for the edge of chaos.

For $335 \lesssim Re \lesssim 515$, the sustained turbulence state is associated with a non-trivial attractor, which may be a chaotic, periodic, or quasiperiodic attractor, depending on the value of the Reynolds number. It was found that the basin boundary of the nontrivial attractor is not relatively smooth like the edge of chaos, but it showed signs of a fractal nature. For $515 \lesssim Re < 1000$, the non-trivial attractor ceases to exist and the stable manifold of the unstable periodic orbit associated with the edge of chaos separates initial conditions which exhibit transiently chaotic behavior from those which directly decay to the laminar state fixed point.

In light of the interesting results obtained from this analysis, it would be

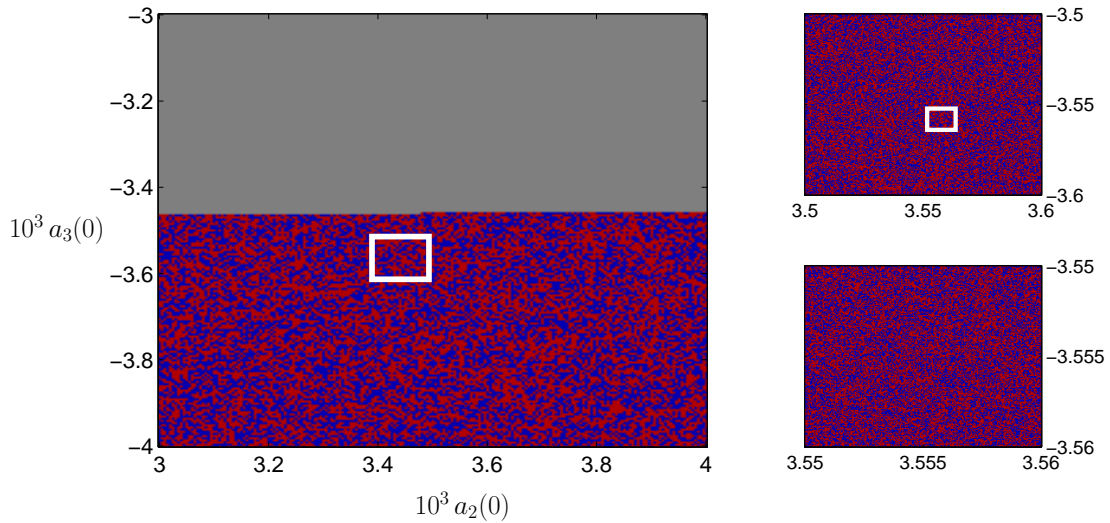


Figure 3.14: A two-dimensional visualization of the edge of chaos showing the basin boundary of the nontrivial attractor. Three different initial conditions are shown: (gray) direct decay to the laminar state, (red) transient chaos before decay, and (blue) nontrivial attractor after some transient chaos. The left panels show successive magnifications.

appealing to characterize the edge of chaos for other low-dimensional models for turbulent shear flows. In particular, for reduced-order models such as sinusoidal shear flow and parallel shear flow, the edge state is nontrivial (i.e. not a fixed point) and/or chaotic in nature. Therefore, characterizing the edge of chaos for low-dimensional models for plane Couette flow, such as those derived in [36, 53], can reveal whether or not the complexity of the invariant structures embedded in the edge of chaos is a result of the reduction in dimensionality of these systems or simply a feature of the nature of the flow, such as for pipe flow.

Chapter 4

The Laminar–Turbulent

Boundary in Plane Couette Flow

The edge of chaos for plane Couette flow will be studied and described in this chapter. This boundary contains solutions, called edge states, which are too weak to become turbulent and too strong to laminarize. To identify the edge states, an iterated edge tracking algorithm is used which is based on a simple bisection method that starts with two initial conditions chosen by scaling a turbulent field such that one becomes turbulent and the other decays to the laminar state without exhibiting turbulence. The tracking algorithm is implemented for several refinements until a trajectory which neither becomes turbulent or laminarizes is found. Edge states for various channel sizes will be characterized and their dynamics will

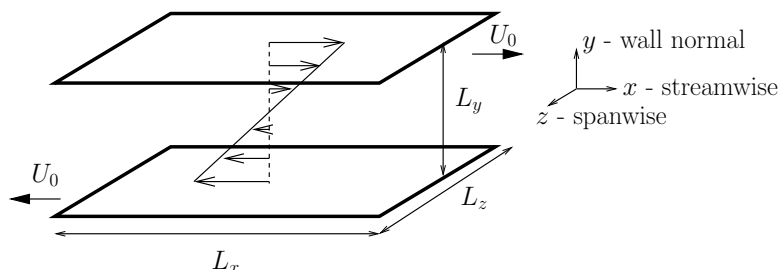


Figure 4.1: Geometry of plane Couette flow. For this flow, incompressible viscous fluid is driven by two infinitely parallel no-slip plates moving at constants speeds in opposite directions.

be compared to edge states for other shear flows. Additionally, for a small range of channel sizes, trajectories in the neighborhood of the laminar-turbulent boundary can converge to one of two edge states whose stability properties will be described in the following.

4.1 Plane Couette Flow

Plane Couette flow confines an incompressible viscous fluid between two infinitely parallel rigid walls which are moving at a constant speed but in opposite direction; see Figure 4.1. At low Reynolds numbers, the flow is laminar with a linear velocity profile between the walls. Unlike other shear flows, such as Taylor-Couette flow and plane Poiseuille flow, plane Couette flow has a laminar profile which is stable for all Reynolds numbers, as was observed in sinusoidal shear flow. Regardless of this constraint, turbulence is observed for this flow both numerically and in experiments.

In the following, the coordinate system is chosen such that the x -axis is the direction in which the walls move, the y -axis is perpendicular to the walls, and the z -axis is both orthogonal to the x -axis and parallel to the wall. Like for sinusoidal shear flow, x , y , and z correspond to the streamwise, wall-normal, and spanwise directions, respectively. The components of the velocity of the fluid are $\mathbf{u}_{tot}(\mathbf{x}) = [u, v, w](x, y, z)$. Plane Couette flow is governed by the Navier–Stokes equations, given in §1.3. This system of differential equations can be nondimensionalized using a velocity scale U_0 and a length scale d which are defined as the velocity of the plates and half the distance between the two plates, respectively. The present length and velocity scales induce the time scale $t = d/U_0$ and results in the following definition of the Reynolds number:

$$Re = \frac{U_0 d}{\nu}. \quad (4.1)$$

After nondimensionalization, the plates are located at $y = \pm 1$ and move with velocity $U_0 = \pm \hat{\mathbf{e}}_x$.

In the following, the dynamics of the deviation \mathbf{u} from the laminar profile will be considered. Therefore, the total velocity of the fluid is replaced by

$$\mathbf{u}_{tot} = \mathbf{u} + y \hat{\mathbf{e}}_x, \quad (4.2)$$

and the Navier–Stokes equations take the form

$$\frac{\partial \mathbf{u}}{\partial t} + y \frac{\partial \mathbf{u}}{\partial t} + v \hat{\mathbf{e}}_x + (\mathbf{u} \cdot \nabla) \mathbf{u} = -\nabla p + \frac{1}{Re} \nabla^2 \mathbf{u}, \quad (4.3)$$

$$\nabla \cdot \mathbf{u} = 0. \quad (4.4)$$

For the laminar state, the pressure is constant, so here p represents the pressure field of the perturbation. The boundary conditions for this flow are the no-slip conditions applied to each wall, thus, giving:

$$\mathbf{u}(x, \pm 1, z) = 0, \quad (4.5)$$

and periodic boundary conditions in the streamwise and spanwise directions,

$$\mathbf{u}(x, y, z) = \mathbf{u}(x + L_x, y, z), \quad \mathbf{u}(x, y, z) = \mathbf{u}(x, y, z + L_z), \quad (4.6)$$

where L_x and L_z are the nondimensionalized lengths in their respective directions and have associated wavenumbers α and γ such that

$$L_x = \frac{2\pi}{\alpha}, \quad L_z = \frac{2\pi}{\gamma}. \quad (4.7)$$

4.1.1 Symmetries of Plane Couette Flow

In practice, understanding the symmetries of a dynamical system can be very beneficial since it can substantially simplify the problem. Moreover, the consideration of the symmetries of differential equations can lead to a greater understanding

of the system. The governing equations for plane Couette flow (4.3) are invariant under the following symmetries:

$$\sigma_x[u, v, w](x, y, z) = [-u, -v, w](-x, -y, z), \quad (4.8)$$

$$\sigma_z[u, v, w](x, y, z) = [u, v, -w](x, y, -z), \quad (4.9)$$

$$\sigma_{x,z}[u, v, w](x, y, z) = [-u, -v, -w](-x, -y, -z), \quad (4.10)$$

corresponding to a rotation by π about the z -axis, a reflection of \mathbf{u} about z , and a point reflection of the flow about the origin, respectively. The flow is also invariant under continuous translations in x and z

$$\tau_{x,l_x}[u, v, w](x, y, z) = [u, v, w](x + l_x, y, z), \quad (4.11)$$

$$\tau_{z,l_z}[u, v, w](x, y, z) = [u, v, w](x, y, z + l_z). \quad (4.12)$$

Most equilibria and periodic solutions of plane Couette flow are invariant under shift-rotate and shift-reflect symmetries which generate the dihedral (D_2) symmetric group

$$S = \{e, \tau_x \sigma_z, \tau_{xz} \sigma_x, \tau_z \sigma_{x,z}\},$$

$$\tau_x = (L_x/2, 0), \quad \tau_z = (0, L_z/2), \quad \tau_{xz} = (L_x/2, L_z/2),$$

which was first introduced by [37, 8].

4.2 Numerical Analysis

The solutions of plane Couette flow will be computed by direct numerical simulations of the Navier–Stokes equations. Direct numerical simulation is an ideal choice since it allows for the ability to solve the full system and it does not require one to provide additional assumptions about the flow. The numerical analysis in this chapter has been completed using *channeflow* [18]. Written by John F. Gibson, the *channeflow* library conveniently provides a method of performing direct spectral simulations of the incompressible Navier–Stokes equations for various types of turbulent shear flows. The simulations for this research have been carried out in the QSR Linux Cluster of the California NanoSystems Institute high computing facility with Hewlett–Packard at UC Santa Barbara and the MARC Linux Cluster of the Hochschulrechenzentrum in Marburg, Germany.

4.2.1 Numerical Discretization and Resolution

In *channeflow*, the solutions are represented by a spectral discretization in the spatial directions [5]. For the system of equations and boundary conditions (4.3–4.5), a Fourier representation in a rectangular grid for the streamwise and spanwise directions is used due to the periodic boundary conditions imposed in

these directions. The velocity field is then expanded as

$$\mathbf{u}(\mathbf{x}, t) = \sum_{l,n} \hat{\mathbf{u}}_{l,n}(y, t) e^{2\pi i(lx/L_x + nz/L_z)}. \quad (4.13)$$

The representation in the wall-normal direction is slightly more complicated due to the non-periodicity of the boundary condition. To account for the no-slip boundary condition, a staggered grid is used in the wall-normal direction. This allows for the velocity to be represented by discrete Chebyshev polynomials in the y -direction

$$\hat{\mathbf{u}}(y, t) = \sum_m^{N_y} \tilde{\mathbf{u}}_{l,n}(t) T_m(y). \quad (4.14)$$

In this scheme, the pressure field is evaluated in between every velocity point and can be represented as

$$\hat{P}(y, t) = \sum_m^{N_y-1} \tilde{P}_{l,n}(t) T_m(y). \quad (4.15)$$

For (4.13–4.15), the symbols ($\hat{\cdot}, \tilde{\cdot}$) respectively represent quantities rescaled in Fourier space and the wall-normal direction.

Channelflow offers two time-integration schemes that treat the linear terms implicitly and the nonlinear term explicitly. The first combines the Crank–Nicolson scheme (for the viscous and pressure terms) with a second-order Adams–Bashworth scheme (for the nonlinear term); see [5] for details. The second scheme, set as default, is a 3rd-order Runge Kutta semi-implicit scheme which employs a corrector step, called *tau correction*, to the solution in the discretized form; see [54] for details.

Choosing the correct numerical resolution is critical for turbulent shear flows because it is important to capture the dynamics of the edge and turbulent states as accurately as computationally possible. For this analysis, streamwise and spanwise resolutions of $N_x = 16L_x/\pi$, $N_z = 16L_z/\pi$ were chosen. The wall-normal resolution was fixed at $N_y = 16.5L_y = 33$. For a channel domain of 4π units long, 2π units wide, and 2 units high, this corresponds to a $64 \times 33 \times 32$ computational grid. These resolutions are similar to those used to calculate edge states in [31, 50]. The resolution was refined for the Newton search and Arnoldi iteration algorithms to $32 \times 49 \times 64$, which was verified both numerically and visually for accuracy with a slightly coarser grid.

4.2.2 The Edge Tracking Algorithm

An iterated edge tracking algorithm was implemented to find the edge of chaos for plane Couette flow. Typical trajectories observed in this flow exhibit either direct decay or transiently chaotic behaviors. The stable laminar state fixed point coexists in state space with the turbulent state and a third object which corresponds to an invariant structure that maintains its own dynamics. Trajectories starting in the stable manifold of this invariant structure will neither decay to the laminar state or grow and become turbulent.

This edge tracking algorithm, which is similar in structure to those used in

Chapter 3 and in [51, 49, 31], traces out the dynamics on the laminar–turbulent boundary. Every point lying on the edge of chaos in principle can be identified with this iterated method. The algorithm was written such that it does not require an *a priori* knowledge of what the invariant structure embedded in the edge has to be. In essence, the purpose of the edge tracking algorithm is to approximate a trajectory that neither decays to the laminar state or grows to become turbulent. This is achieved by adjusting the velocity fields by a scaling parameter.

Figure 4.2 shows a schematic of the iterated edge tracking algorithm. The algorithm starts with a turbulent initial condition \mathbf{u}_t which is obtained from an arbitrary turbulent simulation. The initial condition is connected to the laminar state \mathbf{u}_l with a scaling parameter λ such that

$$\mathbf{u}_\lambda = \mathbf{u}_l + \lambda(\mathbf{u}_t - \mathbf{u}_l). \quad (4.16)$$

When $\lambda = 0$, $\mathbf{u}_\lambda = \mathbf{u}_l$ and as λ is gradually increased to 1, the distance from the laminar state is also increased. Initial conditions will subsequently come closer to the turbulent domain and when $\lambda = 1$ they will meet up with the initial turbulent trajectory $\mathbf{u}_\lambda = \mathbf{u}_t$. The perturbation velocity field $\mathbf{u} = \mathbf{u}_t - \mathbf{u}_l$ is the difference between the laminar and turbulent velocity fields. It is important to point out that only the perturbed velocity field is scaled. This is done to ensure that only trajectories living in between the laminar and turbulent domains are monitored and to avoid numerical instabilities. Bisection in λ between a

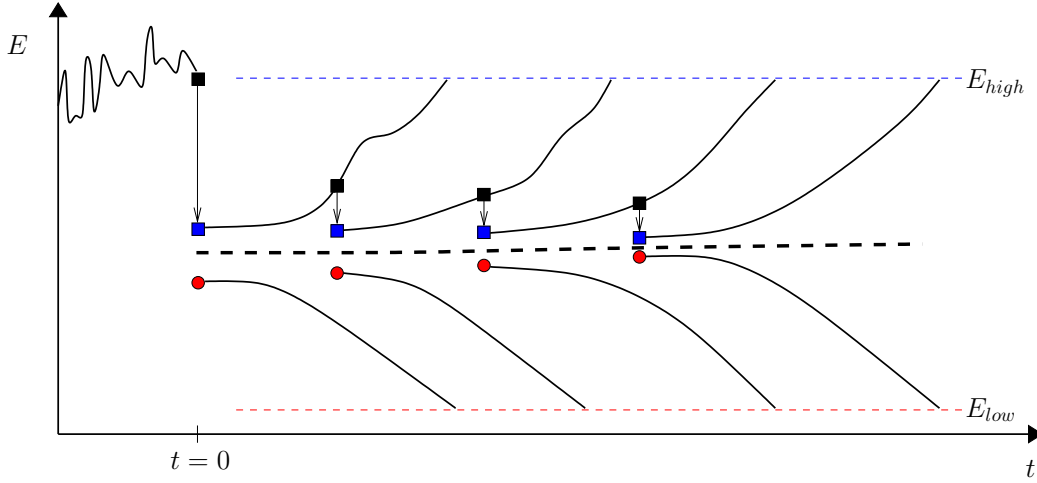


Figure 4.2: A schematic representation of the edge tracking algorithm. A turbulent initial condition is rescaled and a bisection method calculates a pair of trajectories where one grows and becomes turbulent and the other decays and laminarizes. In between the two trajectories is one that neither decays or becomes turbulent corresponding to the edge trajectory (dashed line). Successive iterations minimize the distance between the pair of trajectories.

growing and decaying trajectory makes it possible to focus on the one that lives in between for a substantial amount of time. The edge-tracking algorithm monitors the energy, which is the L_2 -norm of the velocity field, defined as

$$E \equiv \|\mathbf{u}\|_2 = \left[\frac{1}{L_x L_y L_z} \int_0^{L_x} \int_{-1}^1 \int_0^{L_z} \mathbf{u} \cdot \mathbf{u} \, dx \, dy \, dz \right]^{1/2}. \quad (4.17)$$

The L_2 -norm corresponds to the amplitude fluctuation of the velocity field. As shown in Figure 4.3, the energy of decaying and growing trajectories are measurably distinguishable from one another, thus, tracking the energy of the velocity field is convenient.

To minimize extraneous computational time, energy bounds and temporal bounds are imposed. The lower energy bound E_{low} has a value that is very close

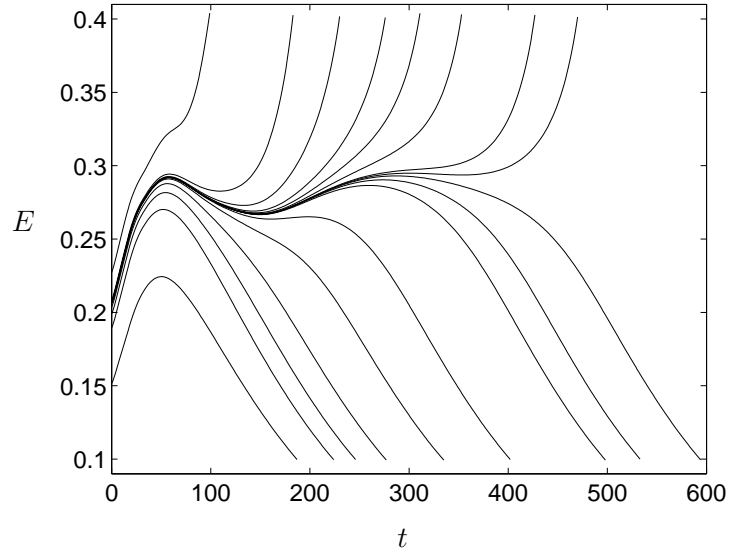


Figure 4.3: One iteration of the edge tracking tracking algorithm showing the energy of trajectories as a function of time. Decaying and growing trajectories are explicitly distinguishable by the evolution of the energy E .

to the energy of the laminar state $E_l = 0$. For this analysis, lower bounds of $E_{low} \in [0.1, 0.15]$ are chosen¹. The upper energy bound E_{high} requires added consideration since for different flow domains and Reynolds numbers, the turbulent state may have different energy values. For this reason, a sample turbulent simulation for different parameter values is performed to determine an adequate value of the upper energy bound. Occasionally, a trajectory might have a long excursion where it neither decays, grows, nor converges to the boundary, therefore a temporal bound of $T = 3000$ units is implemented to terminate the current simulation

¹Generally, the value of E_{low} depends on the flow domain and Reynolds numbers. The energy of the edge trajectory can be close or far away from the laminar state, therefore an appropriate value of the lower energy bound must be chosen to keep performance of the algorithm at an optimum and conserve computational time.

and start a new one with a rescaled initial condition.

Each iteration of the algorithm finds a pair of trajectories on either side of the edge via a bisection method. The first iteration always begins with a scaling factor value of $\lambda = 0.5$, corresponding to $(\lambda_l, \lambda_h) = (0, 1)$, where λ_l, λ_h are the low and high scaling factors respectively corresponding to decaying and growing trajectories. After each trajectory is calculated, based on the current λ , (λ_l, λ_h) are updated accordingly. If the trajectory becomes turbulent, then the algorithm bisects down with the laminar state and if the trajectory decays, the algorithm bisects up with the turbulent state; see Table 4.1 for example scaling factor calculations. The iteration is stopped when the initial separation of the two approximating trajectories δ_λ is sufficiently small. The smaller the value of δ_λ is, the closer the trajectories will be able to approximate an intermediate trajectory and consequently spend more time near the edge state. However, the separation between the approximate trajectories increases over time, therefore, the bisection is repeated when δ_λ is of the order 10^{-8} for several iterations, or refinements, until a solution that neither decays or becomes turbulent is found. For an alternate and detailed description of the edge tracking algorithm, see Appendix B.

On a technical level, the way the new pair of trajectories is found involves starting a new iteration with an initial condition corresponding to the velocity field one-third of the way up the previous turbulent trajectory. The one-third

Scaling factors	Trajectory	New scaling factors
$\left. \begin{array}{l} \lambda_h = 1 \\ \lambda_l = 0 \end{array} \right\} \Rightarrow \lambda = 0.5$	decaying	$\rightarrow \begin{cases} \lambda_h = 1 \\ \lambda_l = \lambda = 0.5 \end{cases}$
	growing	$\rightarrow \begin{cases} \lambda_h = \lambda = 0.5 \\ \lambda_l = 0 \end{cases}$
$\left. \begin{array}{l} \lambda_h = 0.5 \\ \lambda_l = 0.3 \end{array} \right\} \Rightarrow \lambda = 0.4$	decaying	$\rightarrow \begin{cases} \lambda_h = 0.5 \\ \lambda_l = \lambda = 0.4 \end{cases}$
	growing	$\rightarrow \begin{cases} \lambda_h = \lambda = 0.4 \\ \lambda_l = 0.3 \end{cases}$

Table 4.1: Examples of scaling factor calculations.

principle approximately corresponds to 180 time units and it is comparable to temporal refinement bounds of other edge-tracking algorithms. For successive iterations, the initial turbulent and laminar scaling factors are reset to $\lambda_h = 1$ and $\lambda_l = 0.95$. The choice of $\lambda_h = 1$ is obvious since the initial condition that is chosen for the new iteration comes from a turbulent trajectory. The choice for λ_l however is less clear. It is critical to choose appropriate scaling bounds, otherwise, the loss of critical computation time is likely to occur since the algorithm would be calculating trajectories which are too far apart from one another and more importantly, too far from the edge trajectory. Note that the separation amplitude to the initial conditions of the previous iteration are very small, this means that the algorithm has been able to focus on a very specific region of the space. Moreover, after the first iteration, most of the approximate trajectory is smooth, corresponding to the damping of fluctuations of the velocity field. With this in

mind, a lower scaling bound of $\lambda_l = 0.95$ is chosen.² Figure 4.4 shows five refinements of the edge tracking algorithm. The solid lines correspond to trajectories that grow and become turbulent while the dashed lines show trajectories which decay to the laminar state. Every refinement gets initial conditions which have trajectories which come closer to the edge state, thus, approximate edge trajectories maintain approximately constant energy longer with every refinement. The segments of these approximate trajectories can then be concatenated to construct the edge trajectory.

4.2.3 Finding Eigenvalues

Calculating the eigenvalue spectra will be an important step in identifying edge states. Computing the stability of solutions will require the linearization of (4.3), but the size of the state space makes any direct analysis of such magnitude unfeasible.³ One method of alleviating this issue is by projecting the high-dimensional problem into a lower-dimensional *Krylov subspace* [56]. A power iteration calculates the Krylov sequence given by the set of vectors b, Ab, A^2b, \dots , for a given a matrix $A \in \mathbb{R}^{m \times m}$ and an arbitrary initial vector $b \in \mathbb{R}^m$. The n^{th} Krylov subspace $\mathcal{K}_n(A; b) \subset \mathbb{R}^m$ is the linear subspace spanned by large groups of these

²Other edge tracking algorithms, such as the one in [31], use tighter scaling bounds. For this investigation, a slightly larger initial separation amplitude is used to ensure that the correct trajectory is being calculated. Note that this conservative bound does not substantially increase computation times.

³The mathematics and notations of the following iterative methods will be based on [56].

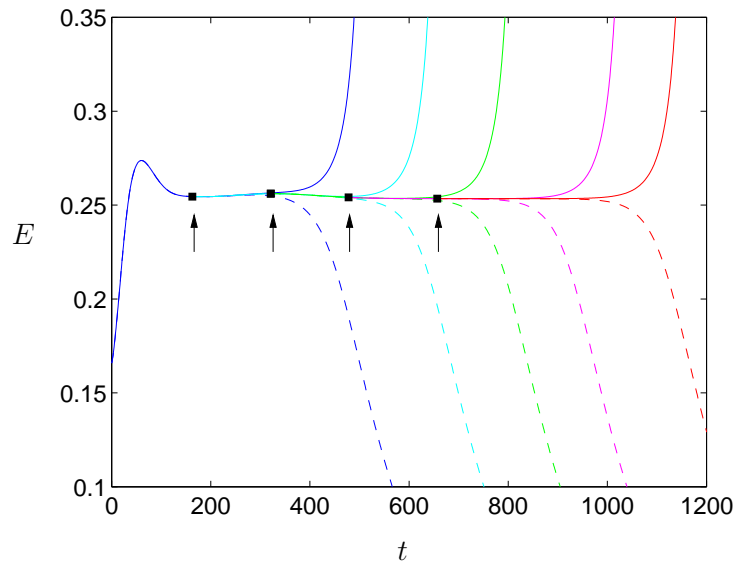


Figure 4.4: Trajectories near the edge of chaos approximated by the edge tracking algorithm after 5 refinements. The solid lines correspond to trajectories which grow and become turbulent and the dashed lines correspond to decaying trajectories. The arrows indicate new iterations of the algorithm. As expected, edge trajectories are longer as the number of iterations increase since the approximate trajectories undergo increasingly sharper refinements.

vector and is defined as

$$\mathcal{K}_n(A; b) = \{b, Ab, A^2b, \dots, A^{n-1}b\}. \quad (4.18)$$

Working in the projected subspace, it is now possible to compute the eigenvalues and eigenvectors of matrix A by means of an Arnoldi iteration. The algorithm utilizes a Gram–Schmidt iteration to approximate eigenvalues of A by computing the eigenvalues of Hessenberg matrices. In detail, by projecting A onto an orthonormal basis for the Krylov subspace, the eigenvalues of A can be estimated

by reducing the matrix into Hessenberg form

$$H = Q^\dagger A Q, \tag{4.19}$$

where Q is a sequence of orthonormal vectors which span the Krylov subspace. The eigenvectors of H (analogous to A) can be efficiently calculated using QR iteration. The Arnoldi algorithm is thus useful for high dimensional systems since it converges to eigenvalues with large real parts first. This means that the total number of Arnoldi iterations is always significantly smaller than the dimension of the full system. Arnoldi iteration is ideal for the purposes of this investigation since the objective is to find states which have only one large real eigenvalue, corresponding to an edge state. The code for the Arnoldi algorithm for finding eigenvalues is included in the *channelflow* library.

4.2.4 Searching for Invariant Structures

The invariant solutions of the governing equations for plane Couette flow (4.3) will be solved using a Newton–hookstep GMRES algorithm. The algorithm, available in the *channelflow* library, can find invariant solutions such as fixed points, traveling waves, periodic orbit, and relative periodic orbits. The following discussion will provide a brief overview of this iteration method. Consider the system $F(u) = 0$ with exact solution u^* . An initial guess u which is near the exact solution u^* can be obtain from the edge tracking algorithm. Letting $u = u^* + du$ and

linearizing the system to first order about this solution gives

$$DF(u)du = -F(u), \tag{4.20}$$

and yields a better approximation of the zeros of the linear system. New guesses can be iterated using the following expression $DF(u_n)(u - u_n) = -F(u_n)$, where u_n is the calculated solution corresponding to the n^{th} iteration. The number of iterations depends on the *goodness* of an initial guess and are typically terminated when the value $F(u)$ is small.

The accuracy of the Newton algorithm is conditional on the near proximity of the initial guesses to the solution. To remedy this problem, an upper limit to the step size du is imposed. This idea is based on [10, 58] where a trust region on the search is implemented

$$\|u - u_n\|_2 \leq \delta. \tag{4.21}$$

So, the trust region δ determines the validity of the linearization about u_n . Therefore, the Newton-hookstep algorithm finds solutions to the minimization of (4.20) subject to the constraint (4.21).

The high dimensionality of the system (and solutions) make finding invariant structures in the full state space impractical. Therefore, a generalized minimal residuals (GMRES) iterative method is used to solve the Newton equations. In essence, the GMRES algorithm solves the system of equations $Ax = b$ in the Krylov subspace. The idea is to approximate the exact solution $x_* = A^{-1}b$ by the

vector $x_n \in \mathcal{K}_n$ that minimizes the residual

$$\|r_n\| = \|b - Ax_n\|. \quad (4.22)$$

A QR decomposition of the matrix A , projected onto \mathcal{K}_n , requires that the least squares problem be solve for the vector y

$$\|AQ_n y - b\| = \textit{minimum}. \quad (4.23)$$

This Newton–hookstep algorithm can also find traveling waves, periodic orbits, and relative periodic orbits. For this study, the Newton search algorithm will be limited to finding equilibria. For further information on how the Newton–hookstep finds other types of solutions, see [18].

4.3 The $L_x = 4\pi$ and $L_z = 2\pi$ Domain

The edge of chaos for the flow domain $[L_x, L_y, L_z] = [4\pi, 2, 2\pi]$ will be characterized in this section. This domain, which has been considered in many previous studies of plane Couette flow [37, 8, 48, 36, 65], corresponds to a domain size where steady state solutions appear at the lowest Reynolds number. It is also the domain for which the edge of chaos has been studied [50, 31], thus, this study will function as a validation of the algorithms and techniques described in the previous section. The laminar–turbulent study for this domain size will be carried out at $Re = 400$ with a computational grid of $64 \times 33 \times 32$. Figure 4.5 shows typical

results from the edge tracking algorithm for different initial conditions. Generally, the edge tracking algorithm does a very good job with approximating trajectories. Though it will not converge all initial conditions, it has a high rate of convergence which can be reached at approximately 600 time units on a fast run.

Starting with different \mathbf{u}_t 's, for this flow domain, the edge tracking algorithm converged to trajectories which visited close to one of the two distinct equilibria. Despite the fact that the \mathbf{u}_t 's are topologically distinct, that is, the initial conditions will converge to different states, the algorithm was successful in calculating trajectories with constant energies; see the top panels of Figures 4.6 and 4.7. The final state, which is extracted after five refinements, is significantly smoother than the initial state but looks different for each trajectory; see the second panels of Figures 4.6 and 4.7. Mainly, the state with a higher energy has a single pair of rolls, and the other has two pairs of rolls confined in the domain. The difference in the energies is expected, since physically, it takes more energy to sustain a single pair of rolls in such a large domain.

The Newton–hookstep algorithm of §4.2.4 is implemented to calculate invariant solutions of the Navier–Stokes equations for this domain, where the final states (shown as red dots in the bottom left panels of Figures 4.6 and 4.7) are used as initial guesses for the algorithm. As expected, for both these states, the Newton algorithm converged to fixed points. The eigenvalue spectra for each of these fixed

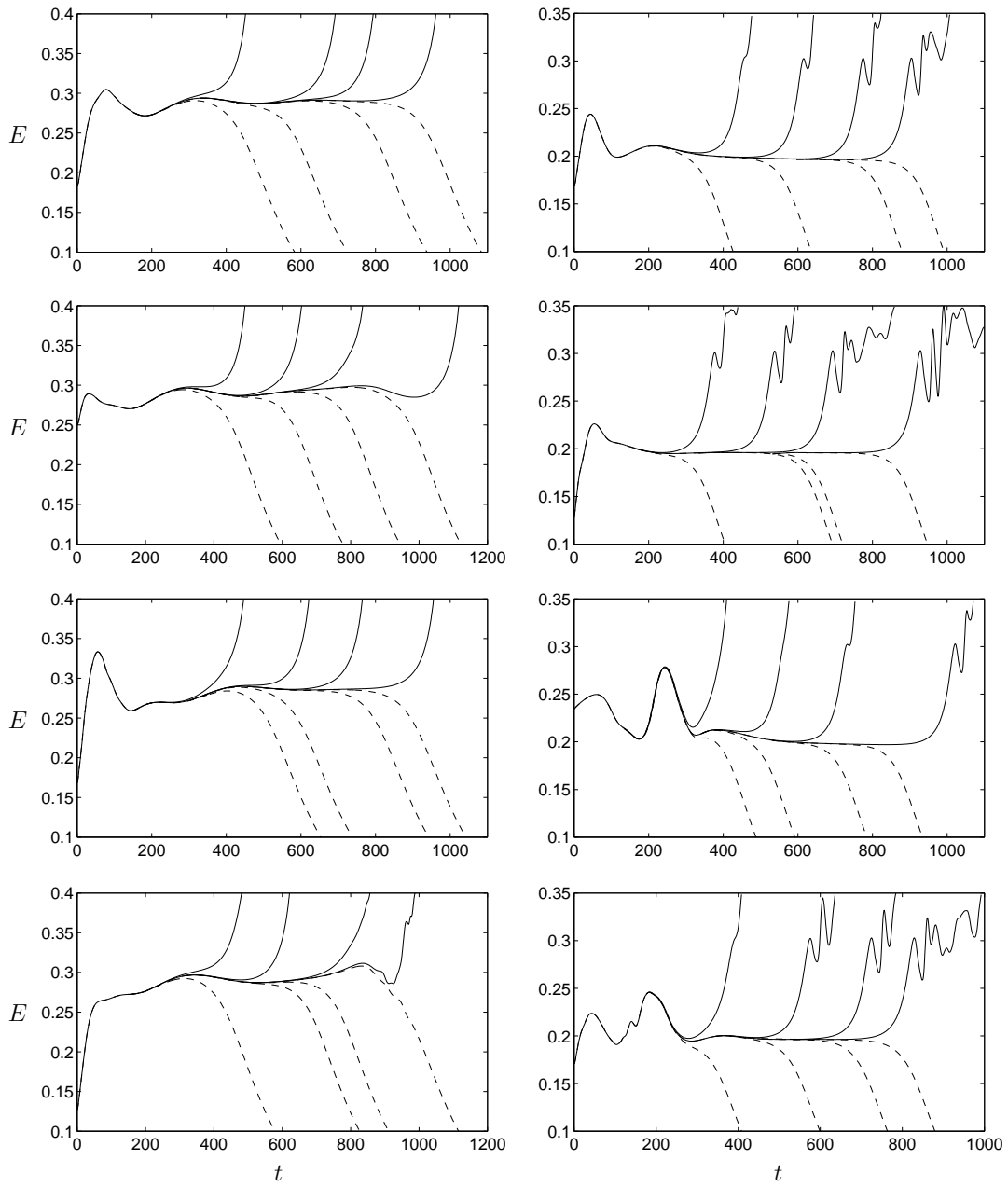


Figure 4.5: Typical edge trajectories for the $L_x = 4\pi$ and $L_z = 2\pi$ plane Couette flow domain calculated with the edge-tracking algorithm.

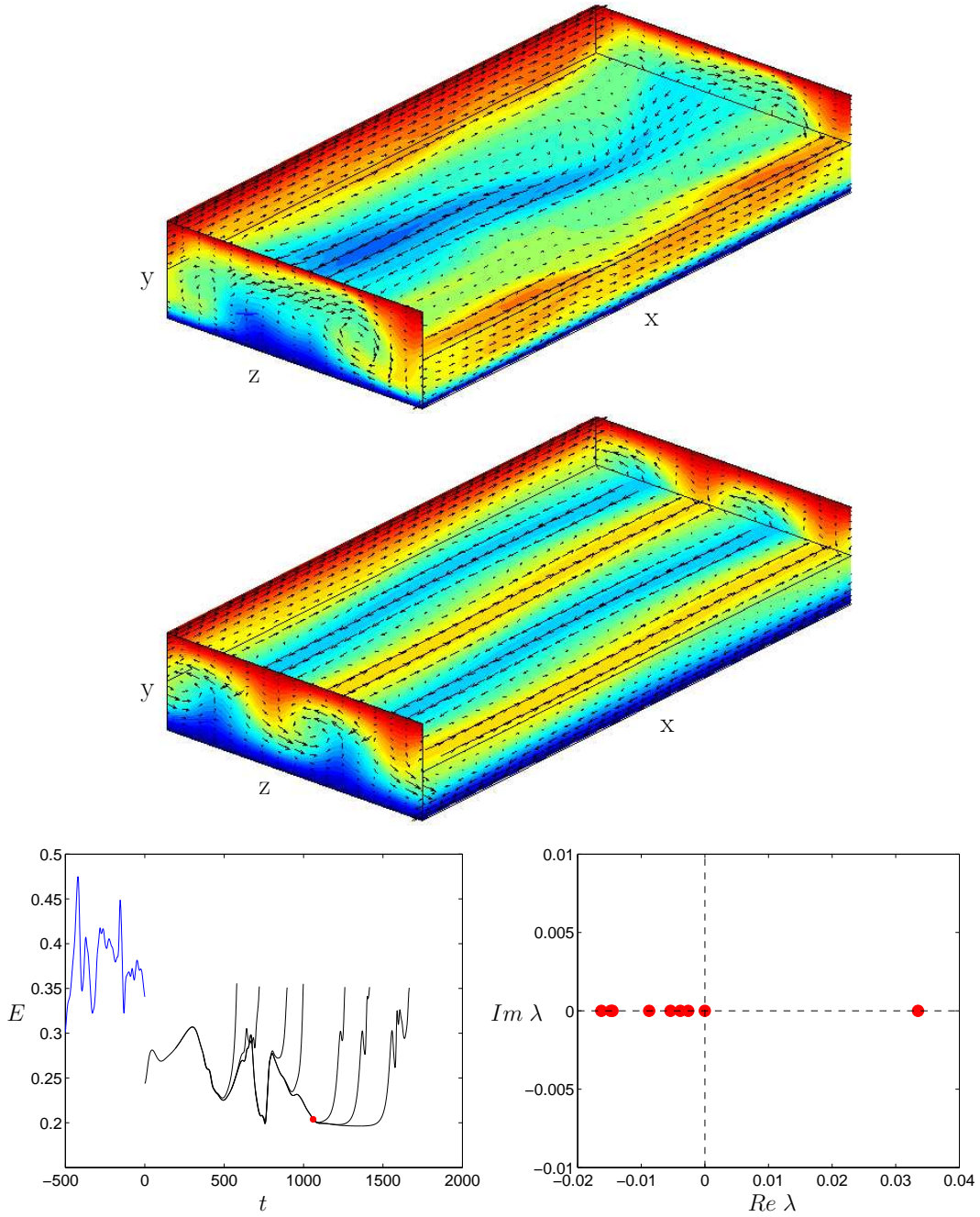


Figure 4.6: The edge state in the $L_x = 4\pi$ and $L_z = 2\pi$ domain. (Top) the initial condition used in the edge tracking algorithm is qualitatively distinct from the converged state (middle) from the Newton algorithm. (Bottom left) the energy traces extracted from the edge tracking algorithm where the red dot corresponds to the final state used as an initial guess in the Newton algorithm. (Bottom right) the single positive real eigenvalue in the eigenvalue spectra confirms that this state is indeed the edge state for this flow domain.

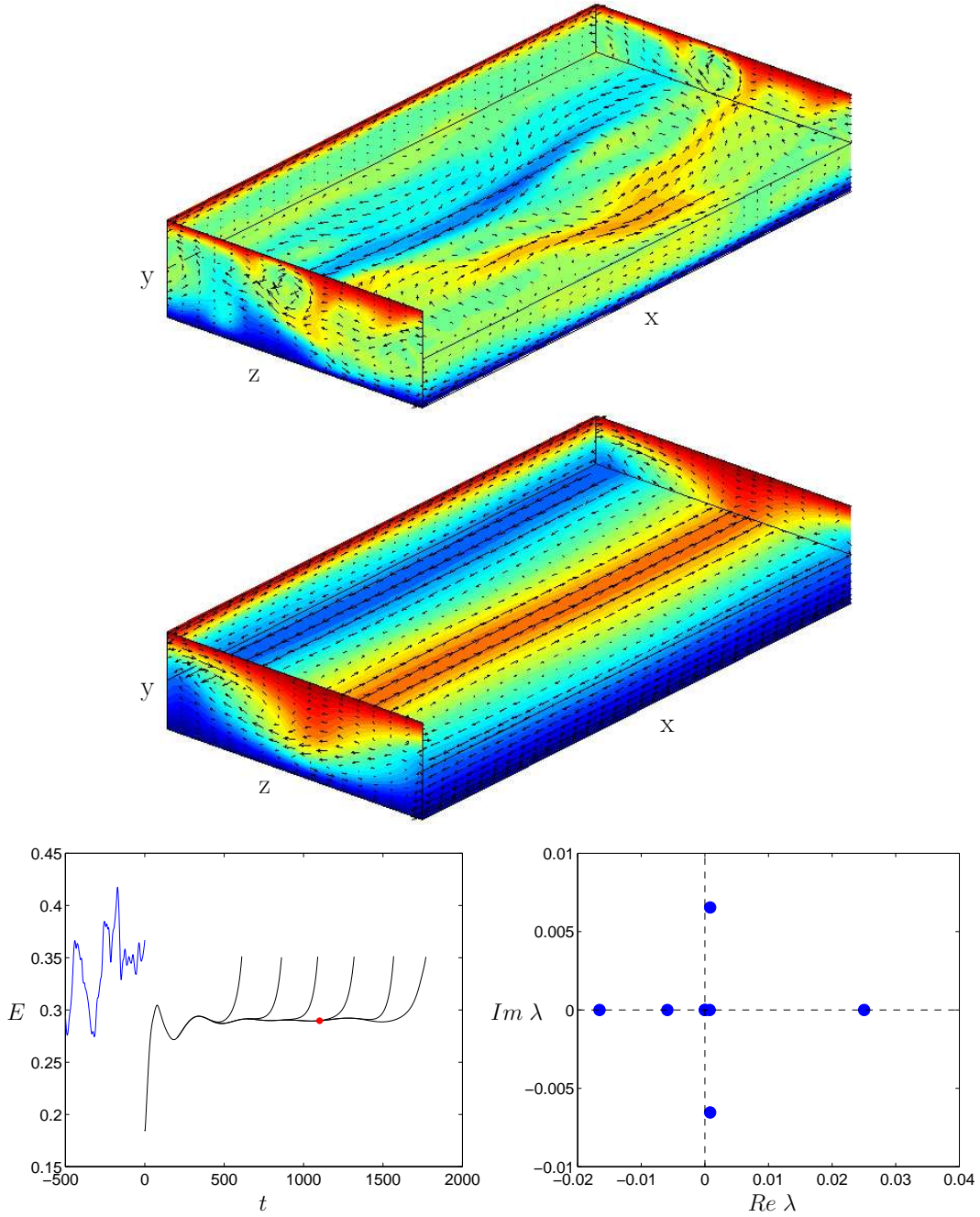


Figure 4.7: An invariant state in the $L_x = 4\pi$ and $L_z = 2\pi$ domain. (Top) the initial condition used in this analysis is topologically different from the initial condition in Figure 4.6. (Middle) a Newton search converged to a state with a single pair of rolls. (Bottom right) The edge tracking algorithm shows a smooth approximate trajectory, nevertheless, the eigenvalue spectra (bottom left) confirms that this state cannot be the edge state since it has 4 positive eigenvalues.

points is calculated to determine their stability. Figures 4.6 and 4.7) show that the 4-roll solution only has one positive real eigenvalue while the 2-roll solution has a total of 4 unstable directions. Each solution also has a pair of neutral eigenvalues which arise from the symmetry with respect to periodic shifts in the streamwise and spanwise directions [50]. The results from this stability analysis determined that the 2-roll solution cannot be an edge state since its stable manifold cannot divide state space. The 4-roll solution, on the other hand, has only one unstable direction and its stable manifold is codimension-1. Thus, the 4-roll solution is the edge state for this flow domain, and its stable manifold forms the edge of chaos.

On the numerical side, the energy of the 4-roll edge state is $E_{edge} = 0.1956$. The edge state is invariant under a $\tau_{z,1/2}$ translation symmetry. The 4-roll edge state and 2-roll solution found in this analysis are the equivalent to the (0.5, 2) and (0.5, 1) states found by [50]. The third state (1, 2) calculated by [50] was not found in this analysis which is likely due to the properties of this state. This state has 5 unstable directions, only one more than the 2-roll state. However, the magnitude of the positive eigenvalues of the (1, 2) state are considerably larger than that of the 2-roll state. The instability of the state makes it hard for trajectories to come near it and its strong unstable manifolds quickly drive them away from the state. Nonetheless, the fact that two of the same states were found validates

the edge tracking algorithm for this investigation.

The fact that the edge tracking algorithm approximates and converges to other invariant states raises the question of how these structures coexist with the edge state. It has been hypothesized that the invariant states may be embedded in the edge of chaos where trajectories near this state tend towards it before they are pulled away to a different direction by one of its unstable manifolds. Figure 4.8 illustrates this scenario, where the invariant state, such as the one found for this domain, lies in the manifold spanned by the stable manifold of the edge state. These states themselves govern their own dynamics, which are similar to those of the edge state, but cannot by themselves separate initial conditions which grow and become turbulent from those which decay to the laminar state without exhibiting turbulent behavior.

4.4 The $L_x = 4\pi$ and $L_z = 4\pi$ Domain

Ultimately, it is of interest to study the dynamics of the edge state as the size of the flow domain and Reynolds number is varied. The motivation for this analysis is to determine if the size and shape of the edge state is dependent on the geometry of the flow domain. For example, if the width or the domain is doubled, does the edge state gain a respective number of rolls or does it simply contain a set of larger modes? This also raises the question of the energetic properties of

Transient Chaos

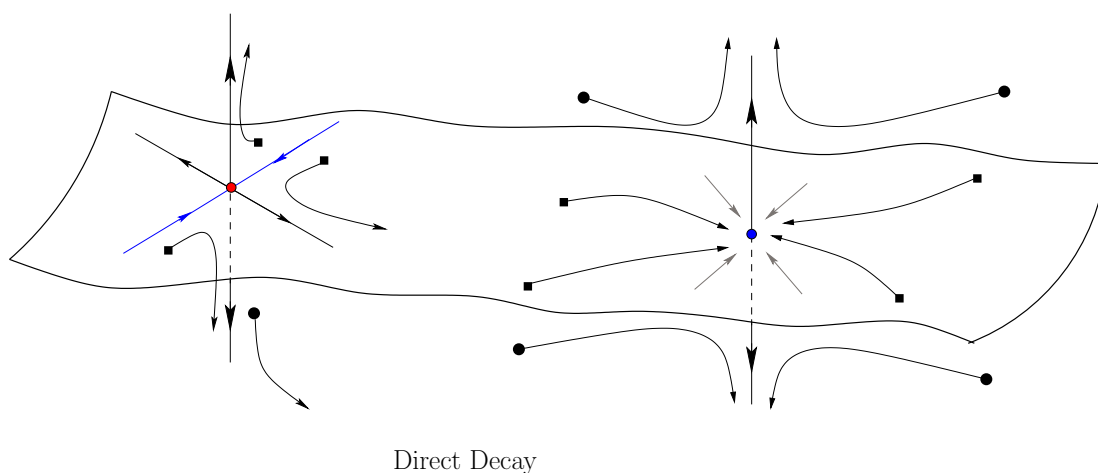


Figure 4.8: Invariant states (red circle) embedded in the edge of chaos may have more than one unstable direction.

the edge states, that is, at what domain size do edge states with uniform energy cease to exist?

In this section, the width of the channel in §4.3 is doubled to identify the edge states in a square domain. The edge of chaos analysis is performed for $[L_x, L_y, L_z] = [4\pi, 2, 4\pi]$ on a $64 \times 33 \times 64$ computational grid.⁴ For this flow domain, the edge tracking algorithm converges to a state with 6 streaks, which is an additional pair of rolls than what is observed in a channel half the width. Indeed, Newton algorithm converged to the state shown in Figure 4.9 which is invariant under a $\tau_{z,1/3}$ translation symmetry. The Arnoldi algorithm confirmed that this state has only one unstable direction, therefore, it is the edge state for

⁴This domain size was also studied in [31]

this flow domain. The energy of this 6-roll edge state is $E_{edge} = 0.2134$.

4.5 Multiple Edge States

Previous studies of the laminar-turbulent boundary in turbulent shear flows have shown that the dynamics on the edge of chaos are dominated by a single invariant structure which is embedded in the edge. It was shown in §4.3 that the edge-tracking algorithm converges to two equilibria. However, upon closer examination, only one of the two equilibrium points corresponds to the edge state. The fact that the algorithm is capable to converge to more than one state raises the question of whether or not the dynamics of the state space can support a scenario where multiple edge states coexist. If so, do they connect and together create a global boundary? Enclose the laminar or turbulent states? Or live in completely different regions of state space and maintain their own dynamics?

Along these lines, an interesting observation from the results in §4.3-4.4 is that the structure of the edge state goes from a 4-roll to a 6-roll solution as $L_z : 2\pi \rightarrow 4\pi$. Here, the goal is to determine when the 4-roll edge state ceases to exist and the 6-roll edge state emerges. To determine how the edge states change in topology, the edge states and their corresponding stability properties for this range of domain sizes is calculated. A Newton algorithm will be used to follow the edge state from §4.3 by systematically increasing the width of the domain.

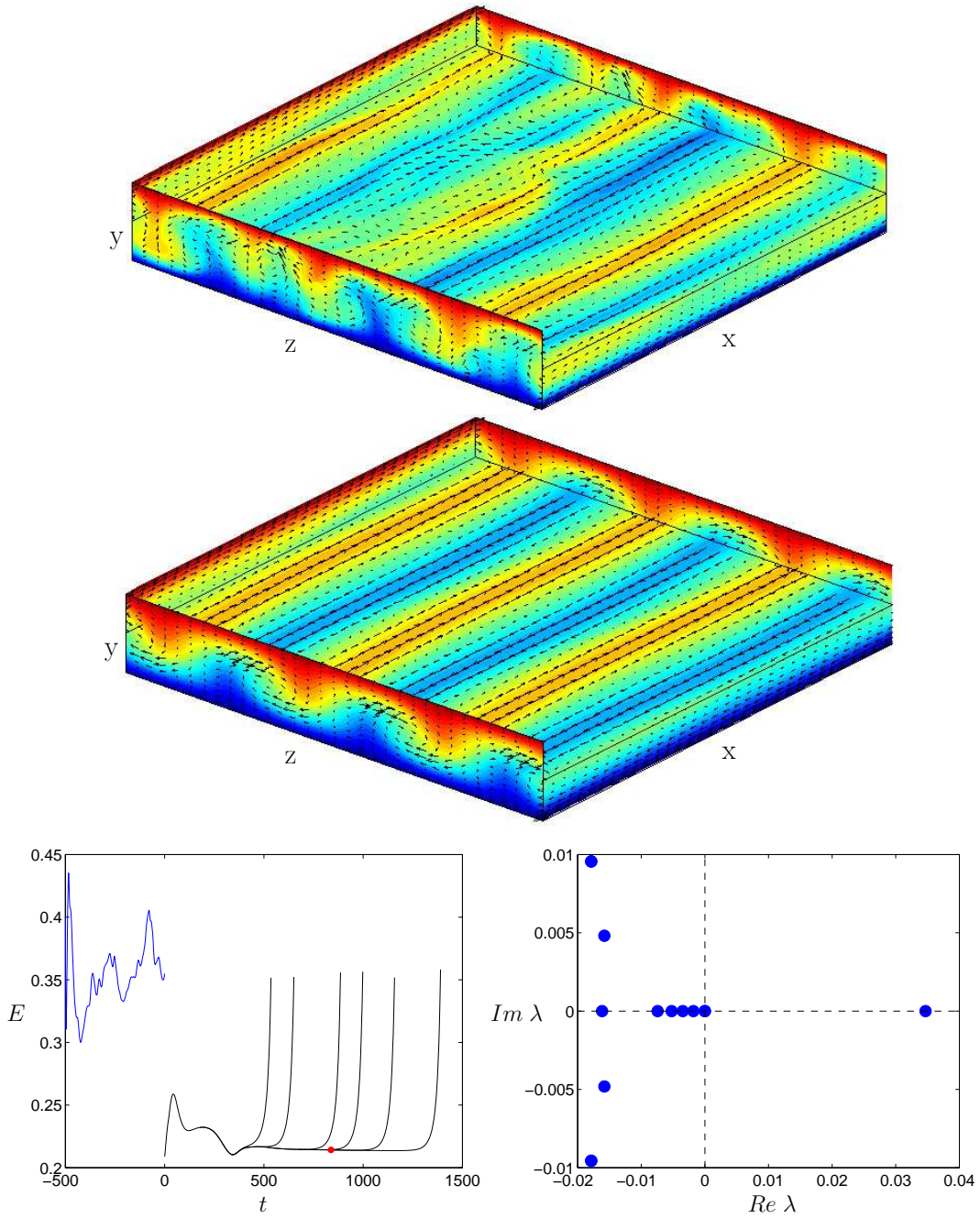


Figure 4.9: (Top) An arbitrary turbulent initial condition used to initiate the edge tracking algorithm for the $L_x = 4\pi$ and $L_z = 4\pi$ flow domain. (Middle) The edge state obtained from the Newton algorithm. (Bottom left) the approximate edge trajectory obtained from the edge tracking algorithm after 5 refinements. (Right) the eigenvalue spectra for the converged state shows that it is indeed the edge state.

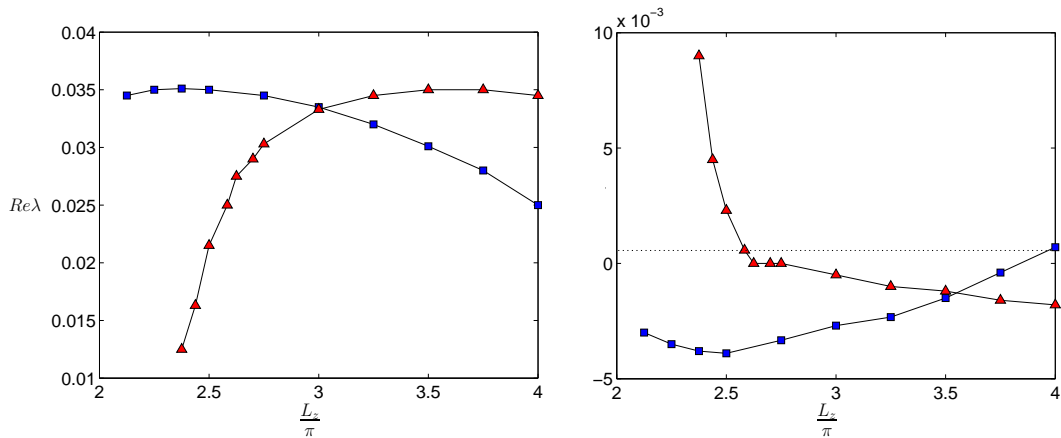


Figure 4.10: Eigenvalue analysis for $Re = 400$, $L_x = 4\pi$, and variable channel width L_z . (left) The real part of the largest eigenvalues for the 4-roll (red squares) and the 6-roll (blue triangles) edge states obtained from following the states using the Newton algorithm. (right) The real part of the second largest eigenvalues determines when the state is no longer an edge state.

Similarly, the edge state from §4.4 will be followed down to a domain width of $L_z = 2\pi$. An Arnoldi algorithm will track the number of unstable directions for these states.⁵

Figure 4.10 shows the two largest eigenvalues of the edge states calculated for different channel sizes. The real part of largest eigenvalues for the 4- and 6-roll edge states are positive for this range of channel widths. On the other hand, the real part of the second largest non-trivial eigenvalue changes in sign at different values of the channel width. In particular, between the values $L_z \in [2.625\pi, 3.75\pi]$ the second largest eigenvalues of the two states is negative, which implies that the 4- and 6-roll solutions are edge states are the same time. To examine how the two

⁵Note that some edge states in this range of L_z and their respective stability properties were calculated using the edge tracking algorithm as a validation of the results.

edge states coexist in state space, the edge tracking algorithm will be implemented for $Re = 400$ and a flow domain of $[L_x, L_y, L_z] = [4\pi, 2, 3.5\pi]$, which corresponds to a $64 \times 33 \times 56$ computational grid.

At $L_z = 3.5\pi$, the edge tracking algorithm converges to one of two states. The first is physically similar in structure to the invariant state for the $L_x = 4\pi$ and $L_z = 2\pi$ domain; see Figure 4.11. The edge state is invariant under a $\tau_{z,1/2}$ translation symmetry, which generates a Z_2 symmetry, and the energy is $E_{edge} = 0.2534$. The eigenvalue spectra for this edge state contains more complex eigenvalues than the edge state in the $L_x = 4\pi$ and $L_z = 2\pi$.

The second converged state from the edge tracking algorithm is one that resembles that of §4.4. Figure 4.12 shows the initial and final states from the edge tracking algorithm. Note that the initial conditions used to extract the 4– and 6–roll solutions from the edge tracking algorithm are different. A stability analysis of this state confirms that this 6–roll solution is indeed an edge state. The energy of the state is $E_{edge} = 0.2028$ and it is invariant under a $\tau_{z,1/3}$ translation symmetry, which generates a Z_3 symmetry.

The edge states for different values of the Reynolds number were calculated for this flow domain using the Newton algorithm using the edge states in Figures 4.11 and 4.12 as initial guesses. For both edge states, the energy increases as the Reynolds number decreases; see Figure 4.13. At approximately $Re = 235$, the

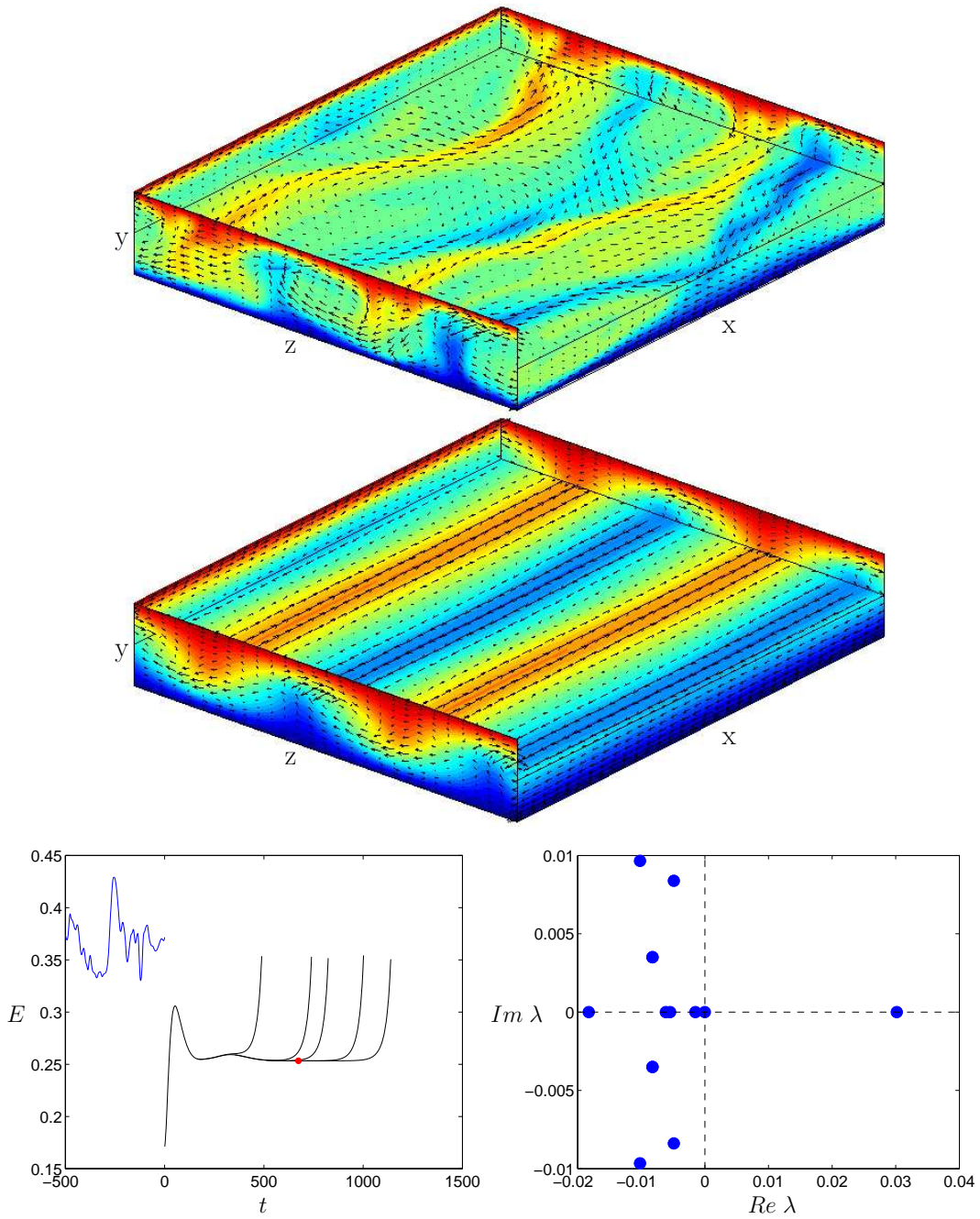


Figure 4.11: The 4-roll edge state in the $L_x = 4\pi$ and $L_z = 3.5\pi$ domain. The converged edge state is very similar in structure to the invariant state in the $L_x = 4\pi$ and $L_z = 2\pi$ domain, but the energy traces and eigenvalue spectra differ considerably.

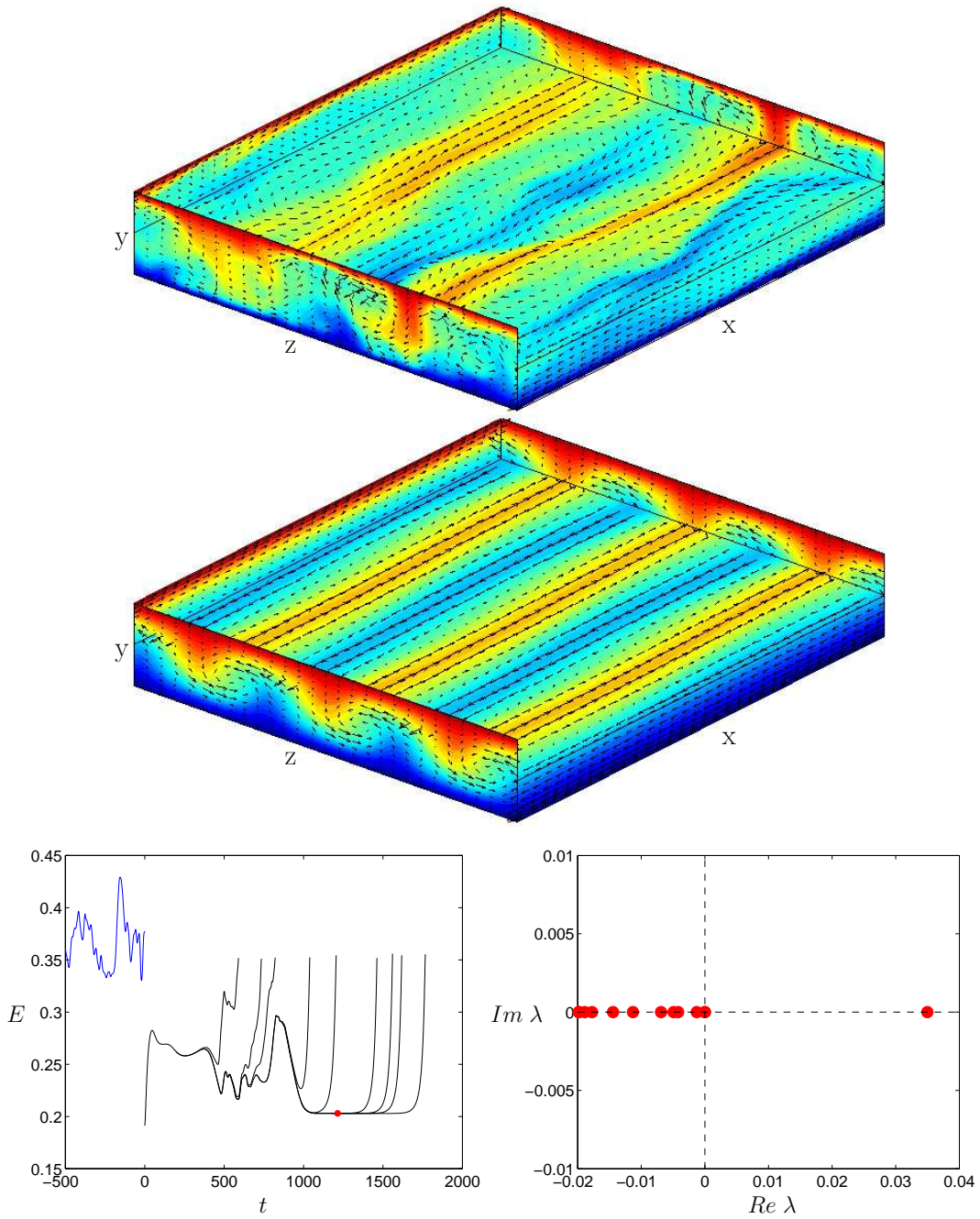


Figure 4.12: The 6-roll edge state in the $L_x = 4\pi$ and $L_z = 3.5\pi$ domain. The converged edge state is very similar in structure to the edge state in the $L_x = 4\pi$ and $L_z = 4\pi$ domain, but the energy traces and eigenvalue spectra show different behaviors.

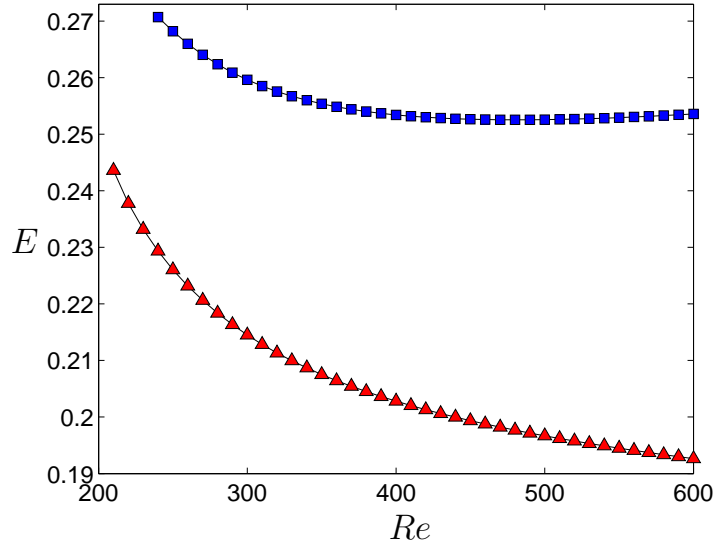


Figure 4.13: Edge states for variable Reynolds number in the $L_x = 4\pi$ and $L_z = 3.5\pi$ domain. The blue and red curves correspond to the edge state with 4-rolls and 6-rolls, respectively.

4-roll edge state undergoes a bifurcation and gains additional unstable directions.

A similar behavior is observed for the 6-roll edge state but for a lower Reynolds number. The upper branches of these curves can be calculated in a similar manner.

4.5.1 Approximate Connections Between Edge States

The edge of chaos analysis was restricted to the invariant symmetry subspaces where each edge state lives. As expected, the results showed that trajectories in the invariant subspaces either decay to the laminar state or grow and tend towards turbulence with the corresponding symmetry. Indeed, the symmetry subspaces only contained one single edge state whose codimension-1 stable manifold forms

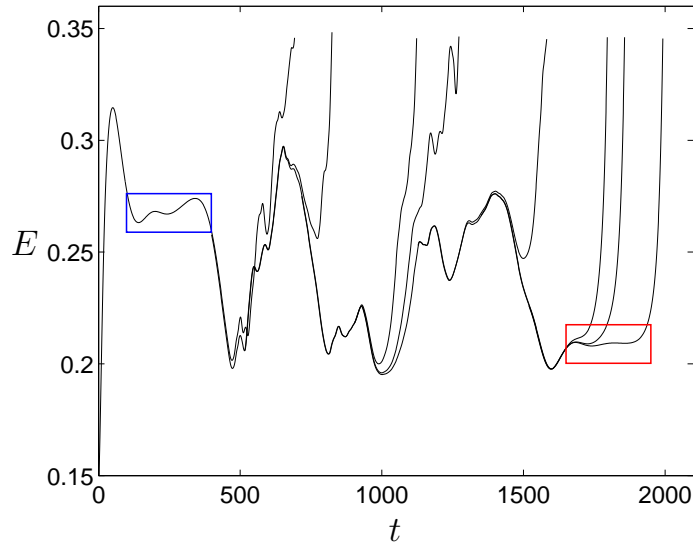


Figure 4.14: An approximate edge trajectory which comes near the 4-roll edge state (blue box) and converges to the 6-roll edge state (red box) after some time.

the edge of chaos.

However, the edge tracking algorithm analysis in the full space revealed something unexpected. The algorithm approximated trajectories that came near one edge state and later converge to another. Figure 4.14 shows such a trajectory which visits near the 4-roll edge state, then leaves and goes through a long excursion before converging to the 6-roll state. This behavior was not unique, and in fact, was observed for multiple initializations of the edge tracking algorithm. This suggests that there might be a single trajectory which connects the two edge states.

To verify that the trajectory in Figure 4.14 does indeed visit near the neigh-

borhood of the two edge states, a Newton search was performed for a sample of velocity fields in the boxes shown in the figure. The results revealed that the trajectories corresponding to the initial states do in fact converge to different fixed points. Furthermore, the Arnoldi algorithm confirmed that these solutions are indeed edge states.

Figure 4.15 shows another edge trajectory which was approximated by the edge tracking algorithm. The behavior of the trajectory is different from that of Figure 4.14, and in fact the time that it takes for this trajectory to go between the two states is very short. The edge tracking algorithm is initialized with a turbulent initial condition which is scaled down via a bisection method at $t = 0$. Between $t = 25$ and $t = 100$ time units, the trajectory is in the neighborhood of the 4-roll solution. The trajectory then makes its way down and comes near the 6-roll solution and remains there during between the interval $t = 170$ and $t = 270$. Recall that the energy of the 4- and 6-roll solutions for this flow domain are $E_{edge,4} = 0.2534$ and $E_{edge,6} = 0.2028$. A Newton algorithm was used to determine whether any of the initial states in the time frame do indeed converge to invariant solutions. At $t = 51$, the Newton algorithm converged to a 4-roll state and the eigenvalue spectrum confirmed that this is the edge state from Figure 4.11. Similarly, at $t = 226$, the edge tracking algorithm converged to the 6-roll edge state from Figure 4.12. This implies that the time that it takes

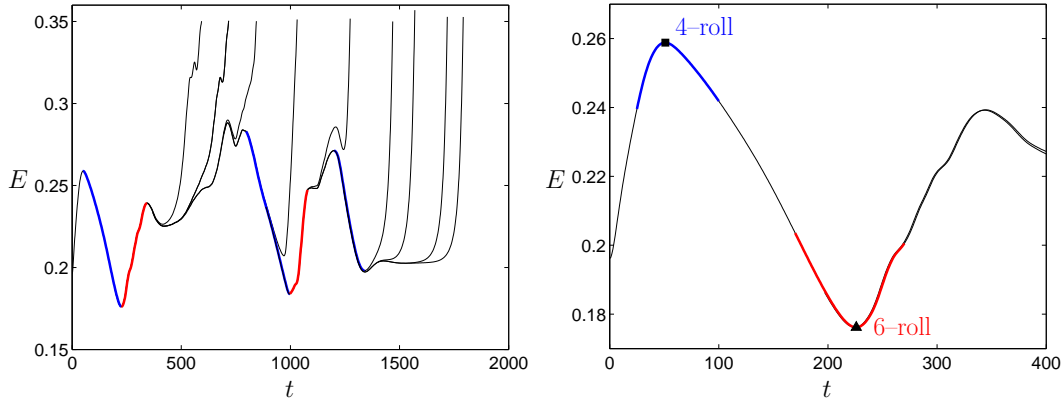


Figure 4.15: (Left) An approximate edge trajectory which comes near both edge trajectories before converging to the 6-roll edge state. (Right) The bold blue and red lines indicates the path the approximated trajectory takes to enter and exit edge trajectories. (Left) Initial guesses used in the Newton algorithm which resulted in convergence to edge states.

for this trajectory to travel from neighborhood of one state to a neighborhood of the other is approximately $T = 175$ time units. Thus, since evidence shows that approximate trajectories come near one state and end up converging to another after some time, the dynamics of the state space can be sketched using Figure 4.16. In this scenario, initial conditions in red and blue squares are in the full space. As time evolves, they come near one of the edge states but get pulled away by the unstable manifolds before converging to one of two edge states.

An alternative interpretation of these observations would involve a non-trivial solution that would be in both of the symmetry invariant subspaces. For example, trajectories can enter and exit the Z_2 and Z_3 symmetry subspaces via a saddle which is invariant under a $\tau_{z,1/6}$ translation symmetry, corresponding to a

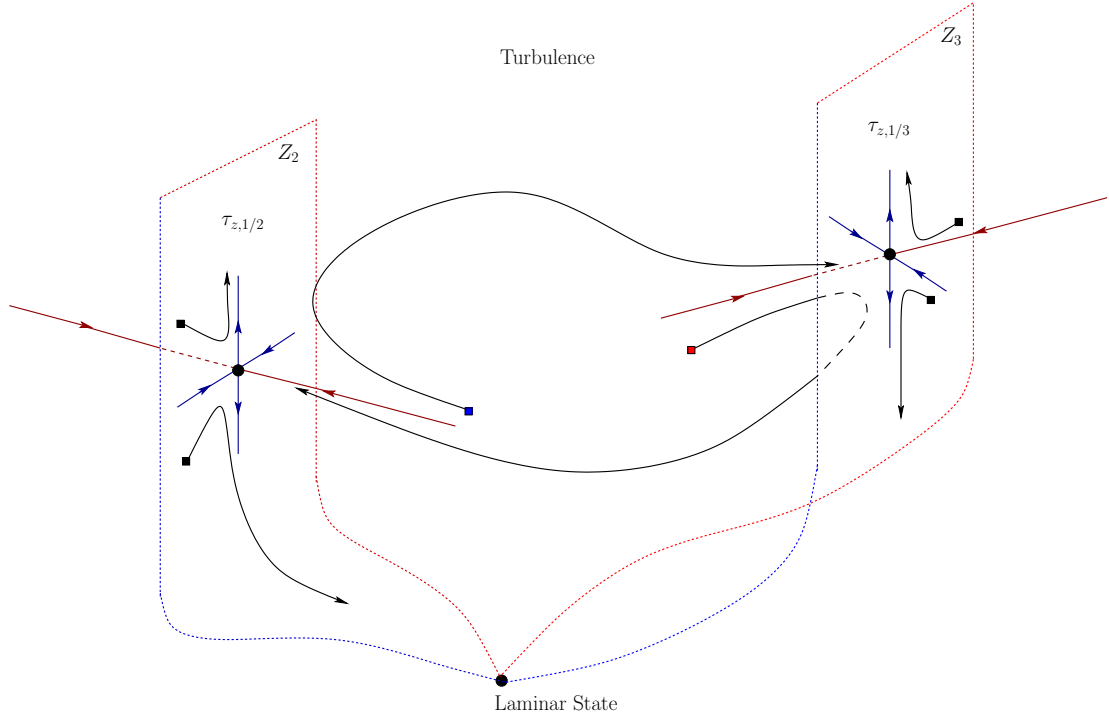


Figure 4.16: A sketch of the dynamics in state space where multiple edge states coexist. For $Re = 400$, $L_x = 4\pi$ and $L_z \in [2.625\pi, 3.75\pi]$, the 4-roll and 6-roll edge states exist in their respective symmetry invariant subspaces. Trajectories starting in the Z_2 (respectively Z_3) subspace will either decay to the laminar state or become turbulent. Initial conditions in the full space (red and blue squares) may result in trajectories which come close to one edge state before converging to the other.

Z_6 symmetry subspace. This scenario was tested in two distinct ways: by perturbation analysis and by spectral analysis. To determine whether the edge states are connected in this way, perturbations of the form

$$\mathbf{u}_p = \mathbf{u}_e + \epsilon \mathbf{u}_u \quad (4.24)$$

were studied, where \mathbf{u}_e corresponds to the velocity field of the edge state, ϵ is the strength of the perturbation, and \mathbf{u}_u is the velocity field corresponding to the unstable eigenfunction. Figure 4.17 shows typical trajectories calculated for

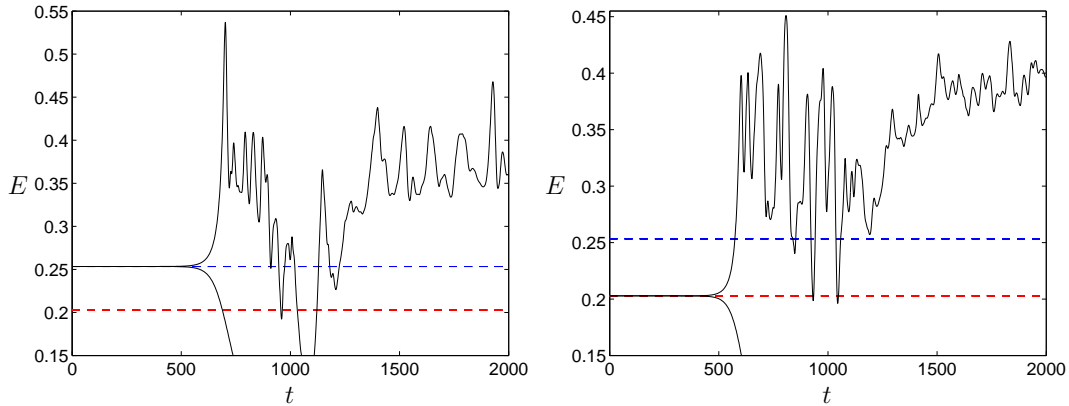


Figure 4.17: Energy traces of perturbations about the unstable manifolds of the edge states for $Re = 400$, $L_x = 4\pi$, and $Lz = 3.5\pi$. For perturbation strengths of order 10^{-10} result in trajectories which spend a long time near the edge before decaying to the laminar state or becoming turbulent.

perturbations strengths of the order 10^{-10} where the blue and red dashed lines respectively correspond to constant energy lines of the 4– and 6–roll edge states. The trajectories initially follow the edge states and after some time, the separation between the perturbations and edge state increases. The results show that trajectories starting on one edge state do not simply connect to the second one, instead, trajectories directly decay to the laminar state or become turbulent. This confirms that the unstable manifold cannot take trajectories outside of the symmetry invariant subspace.

This can also be checked in a different way. The direct numerical simulation generates a finite number of velocity fields between 4– and 6–roll edge states found in Figure 4.15. Although, no *a priori* assumption is made about the symmetries

in these velocity fields, there may be one which exists near the Z_6 symmetry invariant subspace. A spectral analysis was conducted for this set of velocity fields by calculating their Fourier coefficients. If a velocity field is in the Z_6 symmetry invariant subspace, then the total energy of the modes obeying that symmetry should equal to the total energy of all Fourier modes. The analysis found that there are no velocity fields between the visits near the the two edge states which are in the neighborhood of the Z_6 symmetry invariant subspace.

Therefore, the perturbation and spectral analyses suggest that indeed, the first interpretation of the behavior of the trajectory is valid. This implies that trajectories which come near one edge state, then get pulled away and tend towards the second edge state need initial conditions which are not in the invariant symmetry subspaces of the edge states but rather start in the full space. Moreover, since the 4- and 6-roll states are symmetric in that a translation by 2 rolls maps the state into itself, then the unstable manifolds of each edge state will remain in their respective symmetry subspaces. This scenario will absolutely extinguish any possible direct connections between the edge states. However, approximate connection between these states are certainly plausible as was presented in this section.

4.6 Long Flow Domains

The edge states and coherent structures found in pipe flow are dynamically non-trivial. The domain sizes considered thus far for plane Couette flow contain edge states that are much simpler. However, the nature of the edge state may be dependent on the size of the domain. In this analysis the edge of chaos will be characterized for long channels at $Re = 400$ to determine if edge states can be found in geometries which resemble long pipes and to find a correlation between the physical characteristics of the edge state with the size of the domain.

The edge tracking algorithm was implemented for the $L_x = 8\pi$ and $L_z = 2\pi$ flow domain which corresponds to a $128 \times 33 \times 32$ computational grid. The algorithm converged to a state with a single pair of rolls, which was confirmed with a Newton algorithm; see Figure 4.18. The energy in the state is $E_{edge} = 0.2431$.

The length of the previous domain was doubled such that the edge of chaos can be studied for a channel size of $L_x = 16\pi$ and $L_z = 2\pi$. Unlike the small domains, the edge tracking algorithm approximated trajectories with periodic behaviors; see Figure 4.19. The algorithm tracked a trajectory which is not dynamically simple. Nevertheless, the Newton method was able to converge to an equilibrium point which was determined to only have one unstable direction. A symmetry analysis showed that the edge state is invariant under a $\tau_{x,1/2}$ operation. The edge state itself looks a lot like the one found in the previous geometry, and in

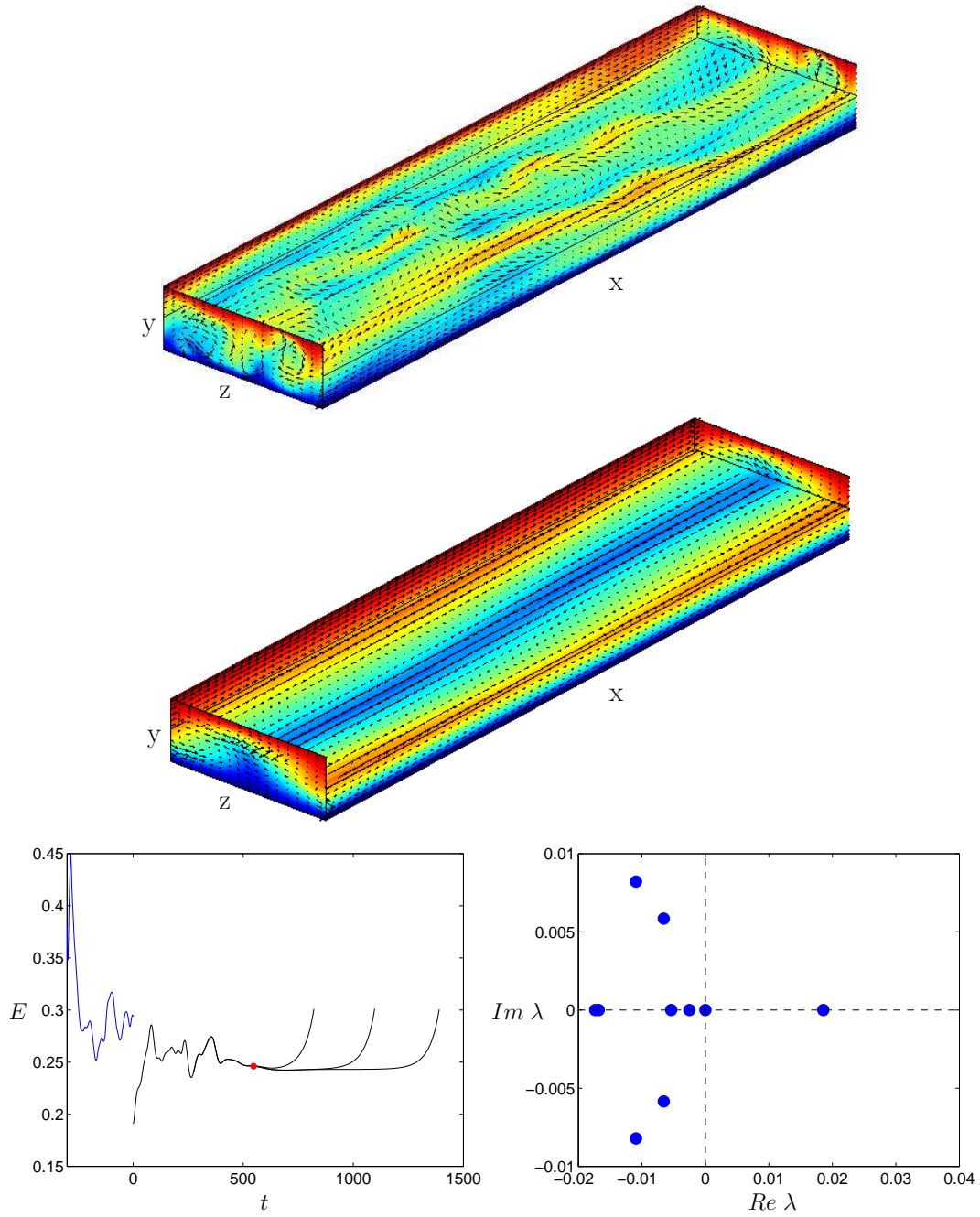


Figure 4.18: The 2-roll edge state in the $L_x = 8\pi$ and $L_z = 2\pi$ domain.

fact, the energy of the state is $E_{edge} = 0.2431$ which is the same value found in a channel half its length. The symmetry properties of this state could suggest that if the edge state in the $L_x = 8\pi$ were to be concatenated to itself to create a longer channel, it may be same state that has been found for this geometry. If it is so, then this would generate some exciting ideas about the existence of edge states for long domains. In particular, it would be interesting to determine if the geometry of the flow domain has any influence on the type of edge states that can be found.

4.7 Discussion

The edge of chaos was characterized for various flow domains of plane Couette flow. The results from the analysis of the $L_x = 4\pi, L_z = 2\pi$ domain confirmed that the edge tracking algorithm is indeed valid in finding approximate edge trajectories. An iterated Newton–hookstep method was implemented to find invariant solutions near the edge and an Arnoldi iteration was used to calculate the stability properties of those states. The edge states for this flow have a single unstable direction, thus, their codimension–1 stable manifolds form the boundary that separate initial conditions which decay to the laminar state without exhibiting turbulence from those which become turbulent in their flow domain. It was found that the shape of the edge state is not linearly related to the size of the

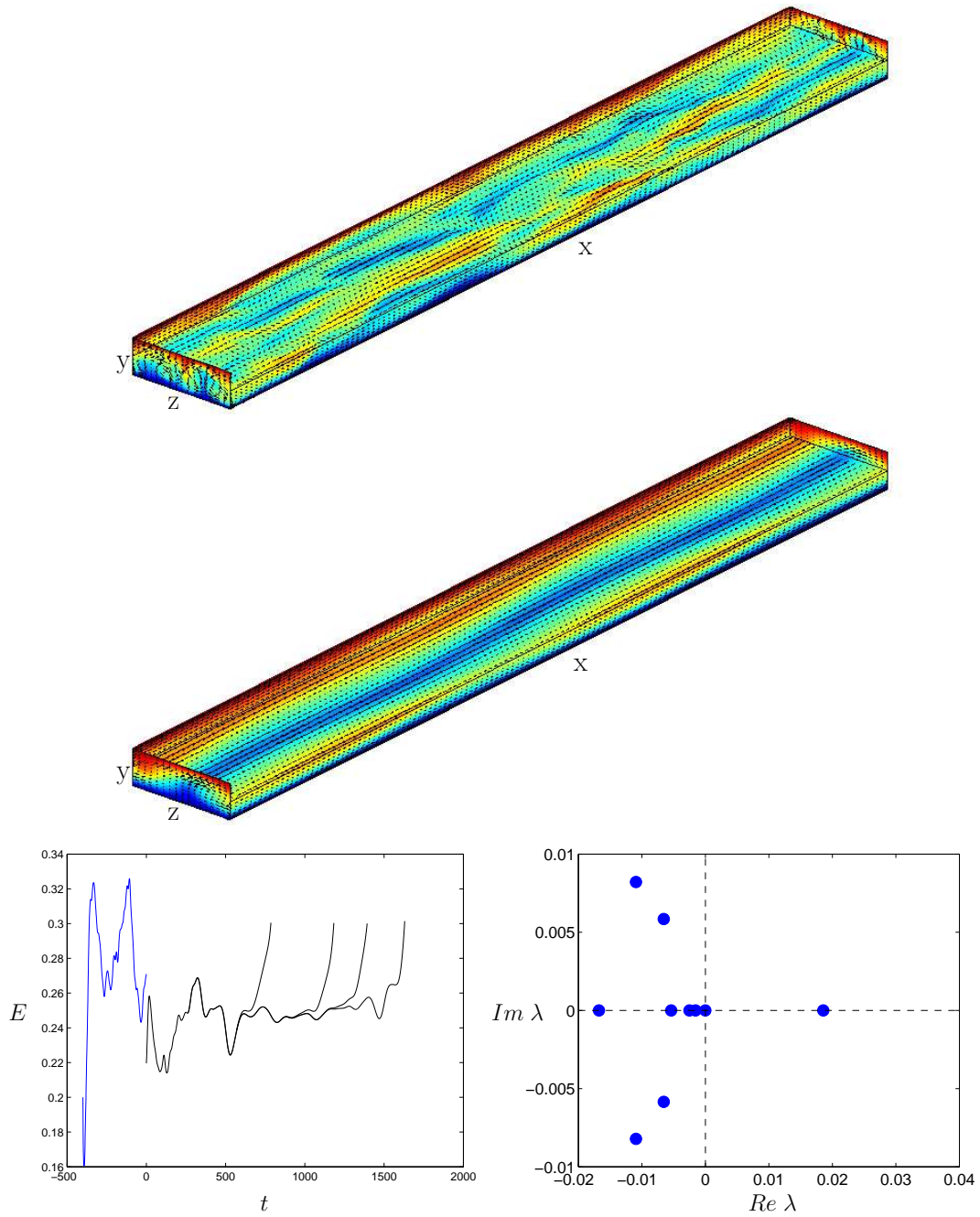


Figure 4.19: The edge state in the $L_x = 16\pi$ and $L_z = 2\pi$ flow domain. Note that the eigenvalue spectrum for this edge state is very similar to that found for the $L_x = 8\pi$ and $L_z = 2\pi$ flow domain.

channel. The edge state in the $L_x = 4\pi, L_z = 2\pi$ flow domain had 4 streaks while the edge state in a domain double this width had 6 streaks. This behavior was also observed for variable channel lengths, the edge state in a $L_x = 8\pi, L_z = 2\pi$ had only 2 streaks. A catalogue of the edge states found for this study can be found in Appendix C.

For a specific range of channel widths, multiple edge states were observed. In particular, for $Re = 400, L_x = 4\pi$, and $L_z \in [2.625\pi, 3.75\pi]$, trajectories calculated by the edge tracking algorithm converged to either a 4-roll or 6-roll edge state which are invariant under different translation symmetries. Approximate edge trajectories which came near both edge states were also found. To explore possible connections between the edge states, a perturbation analysis and spectral analysis was performed. The results from this study revealed that there is no direct connection between the edge states, and moreover, they exist in their own symmetry invariant subspaces. Therefore, initial conditions which start in the full space can have trajectories which visit near both states multiple times before finally converging to one.

Chapter 5

Conclusions

The transition to turbulence in shear flows is still not well understood. Although great advances have been made in this area of research, a quantitatively rigorous description of the transition from laminar to turbulent flow has not been developed. Stability analysis reveals that for flows such as sinusoidal shear flow and plane Couette flow, the laminar state is stable for all values of the Reynolds number, yet turbulence is observed in these flows. Thus, transition to turbulence in these flows is not triggered by linear instabilities of the laminar profile but rather by a different mechanism. Triggering turbulence in these flows requires that initial perturbations and Reynolds numbers be higher than some critical value. It has been suggested that an indication of these critical values can be obtained by monitoring the emergence of exact coherent structures which can sustain the

turbulent dynamics observed in these flows.

In an effort to further understand the transition to turbulence in shear flows, the edge of chaos was characterized for a low-dimensional model for sinusoidal shear flow and the direct numerical simulation of the Navier–Stokes equations for plane Couette flow. The edge of chaos, is the boundary that separates state space into two distinct regions such that trajectories on one side decay to the laminar state without exhibiting turbulence and trajectories on the other grow and become turbulent. Trajectories which neither decay or grow will move around an intermediate region between laminar and turbulent behaviors. Furthermore, trajectories near the edge of chaos will tend towards the edge state. Understanding the dynamics on the edge of chaos may give key insight on the transition process.

The edge of chaos for a low-dimensional model for sinusoidal shear flow was identified as the 8-dimensional stable manifold of an unstable periodic orbit. Initial conditions starting on one side of this boundary decayed directly to the stable laminar state while initial conditions on the other side exhibited transiently chaotic behavior. For a special range of Reynolds numbers, the dynamics of the system included a nontrivial attractor which was associated as sustained turbulence and captures the self-sustaining process identified by Waleffe.

For the related system of plane Couette flow, the edge of chaos for the full Navier–Stokes equations was characterized for various flow domains. An iterated

edge tracking algorithm based on a bisection method was implemented to find invariant solutions in a region where perturbations are too strong to decay or too weak to become turbulent. It was found that for most channel sizes, the edge state is a dynamically trivial object. For a small range of channel widths, coexisting edge states were found. Although the edge states exist in separate symmetry invariant subspaces, trajectories which visited the neighborhood of each edge state were found. A perturbative and spectral analysis determined that there are no direct connections between these edge states.

5.1 Outlook

The edge of chaos has been characterized for several shear flows, and the results obtained from these studies have shed light on a possible mechanism for the transition from laminar to turbulent flow. The analysis of low-dimensional models have greatly helped in understanding the dynamics in the neighborhood of the edge. Recently, the edge of chaos was characterized for a two-dimensional map whose dynamics resemble those found for other shear flows such as pipe flow and plane Couette flow [60]. The advantage of working in smaller dimensions is that it allows for a geometric description of the structure of the edge of chaos, which is unfeasible for higher dimensional systems. Along these lines, it would be of interest to study the edge of chaos for other turbulent shear flows. In particular,

preliminary analysis of the 9–uncoupled–mode model of [53] shows that the edge state in the minimal flow unit domain is dynamically non–trivial. The goal would be to characterize the edge of chaos for various channel sizes and compare the edge states obtained from this study to those found for the full system.

Ultimately, the goal is to extend this study to other flows such as boundary layer flows and plane Poiseuille flow. In particular, the geometry of plane Poiseuille flow resembles that of flows such as plane Couette and sinusoidal shear but the laminar profile is parabolic, which is characteristic of pipe flow. Since so much research has already been invested in pipe and plane Couette flow, it would be nice to see how the edge states from plane Poiseuille flow measure up to the edge states found in those flows. For this flow, turbulent dynamics have been observed at low Reynolds numbers, where the laminar state is stable [27]. Starting out with the minimal flow unit for this flow, the edge of chaos can be characterized for various channel sizes and Reynolds numbers. Moreover, a study of the existence of the edge state in relation to the stability of the laminar profile would be very interesting since it would help enhance the current understanding of the transition to turbulence for flows with primary instabilities in the flow.

The edge of chaos analysis can be extended to areas of research beyond the transition problem. For example, edge states may be important components for controlling turbulence. In particular, designing controllers to alter the behavior

of trajectories near the edge state might be more efficient than trying to change the behavior around other solutions such as the laminar state. Also, these techniques can be applied to other systems besides fluid flows which have more than one qualitatively distinct behaviors, such as large-scale interconnected systems, biological systems, and other chaotic systems.

Bibliography

- [1] N. Aubry, P. Holmes, J. L. Lumley, and E. Stone. The dynamics of coherent structures in the wall region of the turbulent boundary layer. *J. Fluid Mech.*, 192:115–73, 1988.
- [2] J. S. Baggett, T. A. Driscoll, and L. N. Trefethen. A mostly linear model of transition to turbulence. *Phys. Fluids*, 7:833–8, 1995.
- [3] J. S. Baggett and L. N. Trefethen. Low-dimensional models of subcritical transition to turbulence. *Phys. Fluids*, 9:1043–53, 1997.
- [4] G. K. Batchelor. *An Introduction to Fluid Dynamics*. Cambridge University Press, New York, NY, 1967.
- [5] C. Canuto, M. Y. Hussaini, A. Quateroni, and T. A. Zhang. *Spectral Methods in Fluid Dynamics*. Springer-Verlag, New York, NY, 1988.
- [6] S. J. Chapman. Subcritical transition in channel flows. *J. Fluid. Mech.*, 451:35–97, 2002.

- [7] R. M. Clever and F. H. Busse. Three-dimensional convection in a horizontal fluid layer subjected to a constant shear. *J. Fluid Mech*, 234:511–27, 1992.
- [8] R. M. Clever and F. H. Busse. Tertiary and quaternary solutions for plane Couette flow. *J. Fluid Mech*, 344:137–53, 1997.
- [9] P. A. Davidson. *Turbulence: An Introduction for Scientists and Engineers*. Oxford University Press, New York, NY, 2004.
- [10] J. E. Dennis and R. B. Schnabel. *Numerical Methods for Unconstrained Optimization and Nonlinear Equations*. SIAM, Philadelphia, PA, 1996.
- [11] E. Doedel, A. Champneys, T. Fairgrieve, Y. Kuznetsov, B. Sandstede, and X. Wang. *AUTO 97: Continuation and bifurcation software for ordinary differential equations*. 1997. Available from <http://indy.cs.concordia.ca/auto/>.
- [12] P. G. Drazin and W. H. Reid. *Hydrodynamic Stability*. Cambridge University Press, Cambridge, UK, 1981.
- [13] B. Eckhardt and A. Mersmann. Transition to turbulence in a shear flow. *Phys. Rev. E*, 60:509–17, 1999.
- [14] B. Eckhardt, T. M. Schneider, B. Hof, and J. Westerweel. Turbulence transition in pipe flow. *Annu. Rev. Fluid Mech.*, 39:447–468, 2007.

- [15] H. Faisst. *Turbulence transition in pipe flow*. PhD thesis, Universität Marburg, 2003.
- [16] H. Faisst and B. Eckhardt. Traveling waves in pipe flow. *Phys. Rev. Lett.*, 91:224502, 2003.
- [17] H. Faisst and B. Eckhardt. Sensitive dependence on initial conditions in transition to turbulence in pipe flow. *J. Fluid Mech.*, 504:343–52, 2004.
- [18] J. F. Gibson. *Channelflow, A spectral Navier-Stokes simulator in C++*. Available from <http://www.channelflow.org/dokuwiki/doku.php>.
- [19] M. Golubitsky, I. Stewart, and D. G. Schaeffer. *Singularities and Groups in Bifurcation Theory*, volume II. Springer-Verlag, New York, NY, 1988.
- [20] C. Grebogi, E. Ott, and J.A. Yorke. Crises: sudden changes in chaotic attractors and chaotic transients. *Physica D*, 7:181–200, 1983.
- [21] J. Guckenheimer and P. Holmes. *Nonlinear Oscillations, Dynamical Systems, and Bifurcations of Vector Fields*. Springer-Verlag, New York, NY, 1983.
- [22] J. Halcrow, J. F. Gibson, P. Cvitanović, and D. Viswanath. Heteroclinic connections in plane Couette flow. *J. Fluid Mech.*, 621:365–76, 2009.
- [23] J. Hamilton, J. Kim, and F. Waleffe. Regeneration mechanisms of near-wall turbulence structures. *J. Fluid Mech.*, 287:317–48, 1995.

- [24] M. Ilak and C. W. Rowley. Modeling of transitional channel flow using balanced proper orthogonal decomposition. *Phys. Fluids.*, 20:034103–1–17, 2008.
- [25] J. Jiménez and A. Pinelli. The autonomous cycle of near-wall turbulence. *J. Fluid Mech.*, 389:335–359, 1999.
- [26] G. Kawahara and S. Kida. Periodic motion embedded in plane Couette turbulence: regeneration cycle and burst. *J. Fluid Mech.*, 449:291–300, 2001.
- [27] J. Kim, P. Moin, and R. Moser. Turbulent statistics in fully developed channel flow at low Reynolds number. *J. Fluid Mech.*, 177:133–66, 1987.
- [28] L. Kim and J. Moehlis. Characterizing the edge of chaos for a shear flow model. *Phys. Rev. E*, 78:036315, 2008.
- [29] P. Manneville. Spots and turbulent domains in a model of transitional plane Couette flow. *Theor. Comp. Fluid Dyn.*, 18:169–181, 2004.
- [30] P. Manneville and F. Locher. A model for transitional plane Couette flow. *C. R. Acad. Sci. II B*, 328:159–164, 2000.
- [31] D. Marinc. *Localised edge-states in plane Couette flow*. PhD thesis, Universität Marburg, 2008.
- [32] J. Moehlis, B. Eckardt, and H. Faisst. Fractal lifetimes in the transition to turbulence. *Chaos*, 14:S11, 2004.

- [33] J. Moehlis, H. Faisst, and B. Eckhardt. A low-dimensional model for turbulent shear flows. *New J. Phys.*, 6, 2004. Article 56.
- [34] J. Moehlis, H. Faisst, and B. Eckhardt. Periodic orbits and chaotic sets in a low-dimensional model for shear flows. *SIAM J. Appl. Dyn. Syst.*, 4:352–376, 2005.
- [35] J. Moehlis and E. Knobloch. Equivariant dynamical systems. 2007. Scholarpedia. <http://www.scholarpedia.org>.
- [36] J. Moehlis, T. R. Smith, P. Holmes, and H. Faisst. Models for turbulent plane Couette flow using the proper orthogonal decomposition. *Phys. Fluids*, 14(7):2493–507, 2002.
- [37] M. Nagata. Three-dimensional finite-amplitude solutions in plane Couette flow: bifurcation from infinity. *J. Fluid Mech.*, 217:519–27, 1990.
- [38] M. Nagata. Nonlinear solutions of modified plane Couette flow in the presence of a transverse magnetic field. *J. Fluid Mech.*, 307:231–43, 1996.
- [39] M. Nagata. Three-dimensional traveling-wave solutions in plane Couette flow. *Phys. Rev. E*, 55:2023–5, 1997.
- [40] M. Nagata. Tertiary solutions and their stability in rotating plane Couette flow. *J. Fluid Mech.*, 358:357–78, 1998.

- [41] B. R. Noack, P. Papas, and P. A. Monkewitz. The need for a pressure-term representation in empirical Galerkin models of incompressible shear-flows. *J. Fluid Mech.*, 523:339–365, 2005.
- [42] R. L. Panton. *Incompressible Flow*. Wiley-Interscience, New York, NY, second edition, 1996.
- [43] B. Podvin and J. Lumley. A low-dimensional approach for the minimal flow unit. *J. Fluid Mech.*, 362:121–55, 1998.
- [44] S. C. Reddy, P. J. Schmid, J. S. Baggett, and D. S. Henningson. On stability of streamwise streaks and transition thresholds in plane channel flows. *J. Fluid Mech.*, 365:269–303, 1998.
- [45] D. Rempfer. Low-dimensional modeling and numerical simulation of transition in simple shear flows. *Annu. Rev. Fluid. Mech.*, 35:229–265, 2003.
- [46] O. Reynolds. An experimental investigation of the circumstances which determine whether the motion of water shall be direct or sinuous, and of the law of resistance in parallel channels. *The Royal Society*, 174:935–82, 1883.
- [47] P. J. Schmid and D. S. Henningson. *Stability and Transition in Shear Flows*. Springer-Verlag, New York, NY, 2000.

- [48] A. Schmiegel. *Transition to turbulence in linearly stable shear flows*. PhD thesis, Universität Marburg, 1999.
- [49] T. M. Schneider, B. Eckhardt, and J. A. Yorke. Turbulence transition and the edge of chaos in pipe flow. *Phys. Rev. Lett.*, 99:034502, 2007.
- [50] T. M. Schneider, J. F. Gibson, M. Lagha, F. De Lillo, and B. Eckhardt. Laminar-turbulent boundary in plane Couette flow. *Phys. Rev. E*, page 037301, 2008.
- [51] J. D. Skufca, J. A. Yorke, and B. Eckhardt. Edge of chaos in a parallel shear flow. *Phys. Rev. Lett.*, 96:174101 – 4, 2006.
- [52] T. R. Smith, J. Moehlis, and P. Holmes. Low-dimensional modelling of turbulence using the proper orthogonal decomposition: a tutorial. *Nonlinear Dynamics*, 41:275–307, 2004.
- [53] T. R. Smith, J. Moehlis, and P. Holmes. Low-dimensional models for turbulent plane Couette flow in a minimal flow unit. *J. Fluid Mech.*, 538:71–110, 2005.
- [54] P. R. Spalart, R. D. Moser, and M. M. Rogers. Spectral methods for the Navier-Stokes equations with one infinite and two periodic directions. *J. Comp. Physics*, 96:297–324, 1990.

- [55] S. Toh and T. Itano. Low-dimensional dynamics embedded in a plane Poiseuille flow turbulence : Traveling-wave solution is a saddle point? *arXiv:physics/9905012*, pages 1–5, 1999.
- [56] L. N. Trefethen and D. Bau III. *Numerical Linear Algebra*. SIAM, Philadelphia, PA, 1997.
- [57] L. N. Trefethen, A. E. Trefethen, S.C. Reddy, and T.A. Driscoll. Hydrodynamic stability without eigenvalues. *Science*, 261:578–84, 1993.
- [58] D. Viswanath. Recurrent motions within plane Couette turbulence. *J. Fluid Mech.*, 580:339–58, 2007.
- [59] D. Viswanath and P. Cvitanović. Stable manifolds and the transition to turbulence in pipe flow. *J. Fluid Mech.*, 627:215–33, 2009.
- [60] J. Vollmer, T. M. Schneider, and B. Eckhardt. Basin boundary, edge of chaos and edge state in a two-dimensional model. *New J. Phys.*, 11:013040, 2009.
- [61] F. Waleffe. Hydrodynamic stability and turbulence: beyond transients to a self-sustaining process. *Stud. Appl. Math.*, 95:319–43, 1995.
- [62] F. Waleffe. Transition in shear flows. Nonlinear normality versus non-normal linearity. *Phys. Fluids*, 7(12):3060–6, 1995.

- [63] F. Waleffe. On a self-sustaining process in shear flows. *Phys. Fluids*, 9:883–900, 1997.
- [64] F. Waleffe. Three-dimensional coherent states in plane shear flows. *Phys. Rev. Lett.*, 81:4140–3, 1998.
- [65] F. Waleffe. Homotopy of exact coherent structures in plane shear flows. *Phys. Fluids*, 15:1517–34, 2003.
- [66] J. Wang, J. Gibson, and F. Waleffe. Lower branch coherent states in shear flows: transition and control. *Phys. Rev. Lett.*, 98:204501, 2007.
- [67] H. Wedin and R. R. Kerswell. Exact coherent structures in pipe flow: travelling wave solutions. *J. Fluid Mech.*, 508:333–71, 2004.
- [68] S. Wiggins. *Introduction to Applied Nonlinear Dynamical Systems and Chaos*. Springer-Verlag, New York, NY, second edition, 2003.

Appendix A

Uniform Distribution of Initial Conditions for an n -Dimensional Sphere

The following procedure generates a set of uniformly distributed random samples on an n -dimensional sphere based on the method described in §3.4. As an example, consider a nine-dimensional system where a set of uniformly distributed

initial conditions is given by:

$$\begin{aligned}
x_1 &= r \cos(\phi_1), \\
x_2 &= r \sin(\phi_1) \cos(\phi_2), \\
&\vdots \\
x_8 &= r \sin(\phi_1) \sin(\phi_2) \cdots \sin(\phi_7) \cos(\phi_8), \\
x_9 &= r \sin(\phi_1) \sin(\phi_2) \cdots \sin(\phi_8) \sin(\phi_9).
\end{aligned} \tag{A.1}$$

$P(\phi_1, \phi_2, \dots, \phi_9)$ is the probability distribution function defined on the surface of the nine-dimensional sphere which is constant with respect to a uniform distribution. The function can be represented as a product of distributions such that individual functions $P(\phi_j)$ can be readily calculated. For example, for $n = 9$

$$\begin{aligned}
P(\phi_1) &= c_1 \sin^7(\phi_1) \\
\Rightarrow \int_0^\pi P(\phi_1) d\phi_1 &= c_1 \int_0^\pi \sin^7(\phi_1) = 1 \\
c_1 &= \frac{35}{32} \\
\Rightarrow P(\phi_1) &= \frac{35}{32} \sin^7(\phi_1).
\end{aligned} \tag{A.2}$$

Taking advantage of the transformation law of probabilities

$$|P_j(\phi_j) d\phi_j| = |P_u(\omega_j) d\omega_j| \tag{A.3}$$

where $P_u(\omega_j) = 1$ is the uniform distribution on $[0, 1]$, a sample of these probability distribution functions is given by

$$P_j(\phi_j) = \left| \frac{d\omega_j}{d\phi_j} \right|. \quad (\text{A.4})$$

For example, for $n = 5$,

$$\begin{aligned} \frac{d\omega_1}{d\phi_1} &= \frac{3}{4} \sin^3(\phi_1) \\ \omega_1(\phi_1) &= \int d\omega_1 = \int \frac{3}{4} \sin^3(\phi_1) d\phi_1 \\ &= \frac{3}{4} \left[-\frac{3}{4} \cos(\phi_1) + \frac{1}{12} \cos(3\phi_1) \right] + \text{const.} \end{aligned} \quad (\text{A.5})$$

Since $\omega_1(0) = 0$ and $\omega_1(\pi) = 1$, $\text{const.} = \frac{1}{2}$. Therefore

$$\omega_1(\phi_1) = \frac{3}{4} \left[-\frac{3}{4} \cos(\phi_1) + \frac{1}{12} \cos(3\phi_1) \right] + \frac{1}{2}. \quad (\text{A.6})$$

Inverting these samples numerically will give a corresponding value of ϕ_1 . A similar procedure is performed to calculate the remaining ϕ 's, which may be used to construct the set of initial conditions x_j .

Appendix B

Approximating Edge Trajectories

Using an Edge Tracking

Algorithm

The edge tracking algorithm for plane Couette flow finds approximate trajectories that neither decay to the laminar state nor grow to become turbulent. Figure B.1 shows a detailed flow chart of the edge tracking algorithm. Starting with an arbitrary turbulent initial condition, the algorithm employs a bisection method to find two trajectories on either side of the edge. By monitoring the energy of the perturbations, the algorithm automatically rescales initial conditions in the laminar and turbulent regions such that their corresponding trajectories

remain very close to one another and bracket the edge state. When the difference between the trajectories reaches some threshold, the edge tracking algorithm chooses a new pair of initial conditions between the turbulent trajectory and the laminar state. Successive iterations of the edge tracking algorithm can piece together an approximate trajectory near the edge of chaos.

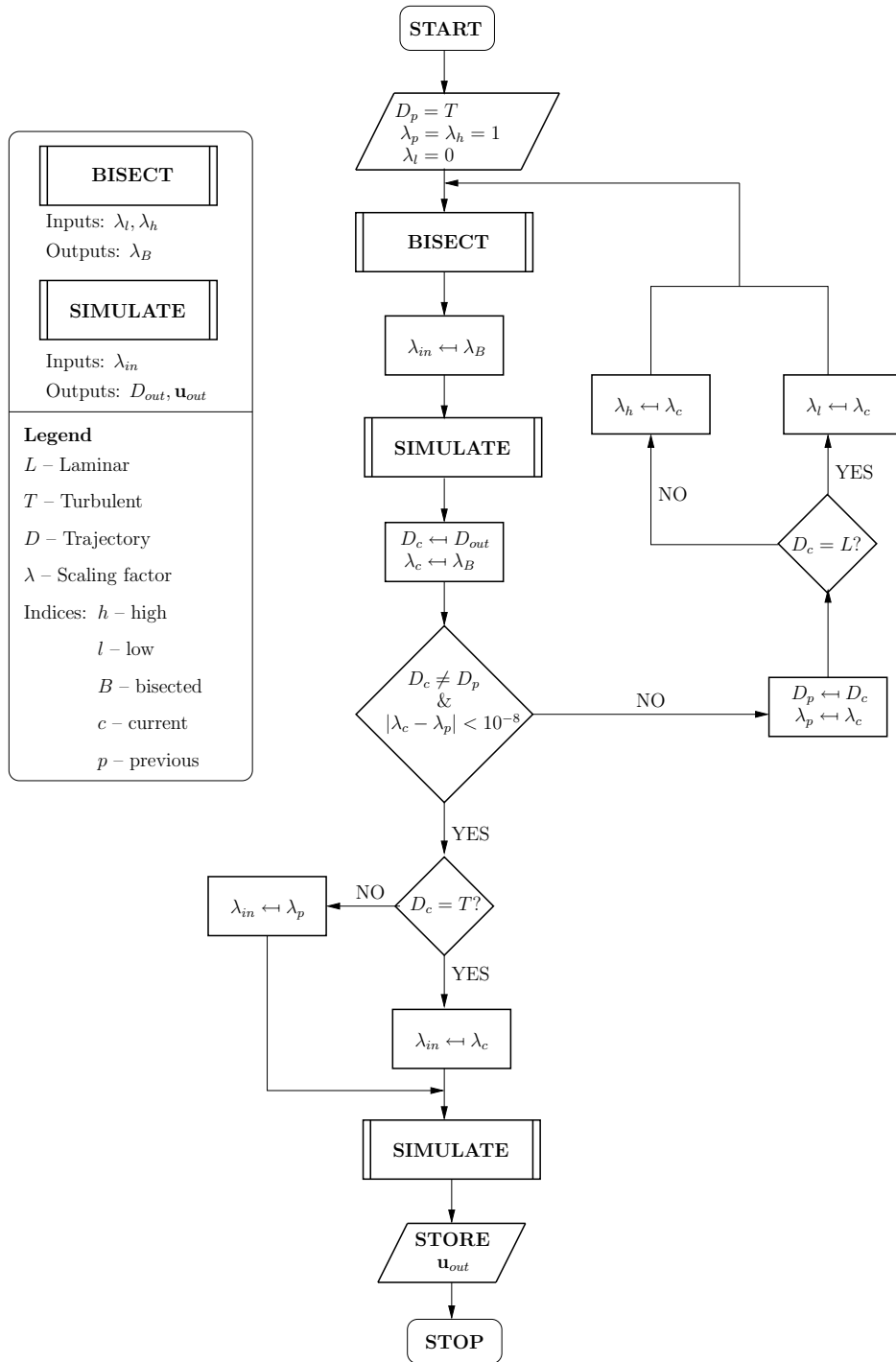


Figure B.1: Edge tracking algorithm flowchart.

Appendix C

A Summary of States found in Plane Couette Flow

The following table shows a summary of the edge states found in plane Couette flow for $Re = 400$. All of the edge states in the given domain have been classified as equilibria. All solutions have a shift-rotate symmetry $\sigma_{x,z}$ along with the symmetry indicated in the table. The first panel corresponds to the midplane velocity field of the edge states where the vectors and colors respectively represent the velocities in and perpendicular to the plane.

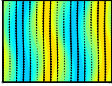
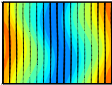
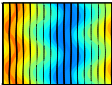
	Flow Domain (L_x, L_y, L_z)	Comp. Grid ($N_x \times N_y \times N_z$)	Energy (L_2 -norm)	Symmetry
	($4\pi, 2, 2\pi$)	$64 \times 33 \times 32$	0.1956	$\tau_{z,1/2}$
	($4\pi, 2, 3.5\pi$)	$64 \times 33 \times 56$	0.2534	$\tau_{z,1/2}$
	($4\pi, 2, 3.5\pi$)	$64 \times 33 \times 56$	0.2028	$\tau_{z,1/3}$
	($4\pi, 2, 4\pi$)	$64 \times 33 \times 64$	0.2134	$\tau_{z,1/3}$
	($8\pi, 2, 2\pi$)	$128 \times 33 \times 32$	0.2431	–
	($16\pi, 2, 2\pi$)	$256 \times 33 \times 32$	0.2431	$\tau_{x,1/2}$

Table C.1: Classification of edge states in plane Couette flow